Title
Dynamics of Glaciers and Ice Sheets at the Ocean Margin from Airborne and Satellite Data

Author
Millan, Romain

Publication Date
2018

Peer reviewed|Thesis/dissertation

UNIVERSITY OF CALIFORNIA,
IRVINE

Dynamics of Glaciers and Ice Sheets at the Ocean Margin from Airborne and Satellite Data

DISSERTATION

submitted in partial satisfaction of the requirements
for the degree of

DOCTOR OF PHILOSOPHY

in Earth System Science

by

Romain Millan

Dissertation Committee:
Donald Bren Professor Eric Rignot, Chair
Professor Isabella Velicogna
Assistant Professor Mathieu Morlighem

2018

DEDICATION

To my family, my wife and friends

TABLE OF CONTENTS

LIST OF FIGURES

LIST OF TABLES

ACKNOWLEDGMENTS

First, I would like to thank my PhD advisor, Prof. Eric Rignot who gave me the opportunity to work on these exciting projects, do fieldwork in Greenland, helping me through the course of my PhD and making all of this possible. I am very grateful for his support, enthusiasm, positivity and the fact that he has trust in my work since I arrived in 2014. When I began to study Earth Sciences in Strasbourg, my goal has always been to study glaciers and ice sheets, and I can't thank him enough for gaving me the best possible opportunity to realize this dream.

Thank you to my dissertation committee members Mathieu Morlighem and Isabella Velicogna for providing me good comments, insights on my work and important collaborations through my PhD.

I sincerely thank Jérémie Mouginot for his unbreakable motivation, curiosity, patience and all he taught me on Remote Sensing and programming. Many thanks to Bernd Scheuchl for his indispensable help on Remote Sensing and writing. Everything would have been different without their help, I don't know how they have remained so calm and patient with me after all the questions I have asked them.

I would like to thank Anders Anker Bjørk, Abbas Shfaqat Khan, Kristian Kielsen and Kurt Kjær at DTU/SPACE and the University of Copenhagen, for being great fieldwork partners, integrating me in exciting projects and welcoming me at the University of Copenhagen.

I want to thank my office mate Emily Kane for her everyday positivity, being such a great fieldwork partner and being so patient for enduring my presence everyday in the lab! I really want to thank the past and present members of the Cryosphere research groups: Michael Wood, Lu An, Youngmin Choi, Tara Harder, Xin Li, Hongju Yu, Cilan Cai, Yara Mohajerani, Enrico Ciraci and Tyler Sutterley for their support through my PhD.

I would also like to thank my classmate friends: Daniel Ruiz, Shih-Wei Fang, Christian Lewis, Johan Lopez, Blanca Rodriguez, Megan Fowler and Zach Labe. Thank you to Qian Huang for being such an amazing TA partner. It was great to spend these years of Graduate School in such a friendly and supportive atmosphere!

I would like to thank my wife Judith, who has supported and pushed me through my whole PhD, without her, this work would not have been possible. Thank you to my entire family for passing on their love for nature, their all-time support and enduring my bad temper. Thanks to my friends in France, that always pushed me to do what I love, even if it meant to leave the country. Finally, thank you to Alice, Yannick, Jéremie, Céline, Camille and Mike for their friendship and who welcomed me in the US and made my life so pleasant and exciting, I owe you a lot.

We thank the NASA-funded OIB instrument team for their achievements in collecting OIB data pole-to-pole since 2009 and making this thesis possible.

We also thank A. Muto and K. Tinto for useful discussions at the project inception, P. Dutrieux, L. Peters, A. Muto and S. Anandakrishnan for sharing the AUV and seismic data.

The work presented in this thesis was performed at the University of California, Irvine and funded by grants from the National Aeronautics and Space Administration's Cryosphere Science Program (contracts NNX13AI84A, NNX14AN03G, NNX14AB93G and NNX17AI02G), Operation IceBridge Mission (OIB) and Interdisciplinary Science program at the University of California Irvine and at Caltech's Jet Propulsion Laboratory.

Parts of Chapter 2, 3 and 4 are reprinted with permission from the American Geophysical Union and IOPscience. The original texts appear in *Geophysical Research Letters* and *Environmental Research Letters*. I would like to thank all the co-authors for their contributions and invaluable insights on these articles.

CURRICULUM VITAE

Romain Millan

Research Interests

Glaciology	Mass balance	Ice dynamics
Ice velocity	Bedrock topography	DEM differencing
Radar interferometry	Optical Imagery	Airborne gravity inversion

Education

- **University of California Irvine** Irvine, USA
  PhD Candidate in Earth System Sciences (Supervisor: E. Rignot) *2015 – 2018*
  - PhD title: Remote sensing of glaciers and ice sheets from satellite and airborne observations.
- **University of California Irvine** Irvine, USA
  Master degree in Earth System Sciences *2015 – 2016*
  - Main courses: Global Physical Climatology, Geoscience Modeling and Data Analysis, Ocean processes, Atmospheric chemistry and physics, Geophysical Fluid Dynamics, Land processes.
- **University of Strasbourg** Strasbourg, France
  Master degree in Solid Earth and Planetary Sciences *2013 – 2014*
  - Main courses: Remote sensing, earth deformation, paleoseismology, seismology
- **Ecole et Observatoire des Sciences de la Terre** Strasbourg, France
  Engineering diploma in geophysics *2011 – 2014*
  - Main courses: geodesy,potential methods, seismic, rock's physics, stratigraphy, acquisition and processing of geophysical data, field and laboratory work
- **Universite d'Avignon et des Pays du Vaucluse** Avignon, France
  2 year of Bachelor degree in mathematics and physic (DEUG diploma) *2009 – 2011*

Research Experience

- **University of Copenhagen** Copenhagen, Denmark
  Advisors: A. A. Bjørk (Copenhagen University) *March-May 2017*
  – Digitization, orthorectifaction and georeferencing of aerial images in Greenland spanning the period 1940-1970 for the calculation of ice velocity.
- **University of California, Irvine** Irvine, USA
  Advisors: E. Rignot (UCI, JPL-Pasadena), J.Mouginot (UCI) *Sep-March 2015*
  – Ice dynamics of the Canadian Arctic Archipelago from remote sensing observation (processing of ALOS-PALSAR, RADARSAT, ERS and LANDSAT data, speckle-tracking, InSAR, grounding line mapping, IDL programming)
- **LISTIC - LEGOS** Annecy, France
  Advisors: E. Trouvé (LISTIC), E. Berthier (LEGOS) *Feb-June 2014*
  – Processing of TanDEM-X SAR images for the observation of glaciers thickness changes in the Chamonix-Mont-Blanc area (DInSAR processing with Gamma-rs software, DEM differencing, python programming)
- **Earthquake Engeneering Research Center (EERC)** Selfoss, Iceland
  Advisor: B. Halldorsson *July and Aug 2013*
  – Parameterization of ICEARRAY Recordings of the Aftershock Sequence following the 29 May 2008 M6.3 Olfus Earthquake in South Iceland
- **Institut de Physique du Globe (IPGS)** Strasbourg, France
  Advisor: N.Gourmelen, A.Dehecq *Jan to June 2013*
  – Study of the dynamic of Himalayan glaciers (cross-correlation of Landsat images, automatic computing of center-flow-line, Bibliography, matlab)

Field Experience

- **Northeast Greenland: Monitoring of Zachariae Isstrom glacier** Aug 2017
  GPS and automatic Weather station on ice, tide gauge and AXCTD in the fjord.
- **Northeast Greenland: Monitoring of Zachariae Isstrom glacier** Aug 2016
  GPS and automatic Weather station on ice, tide gauge and AXCTD in the fjord.
- **West Greenland, Monitoring of Kangilerngata sermiaa glacier** Jul 2016
  Ground radar interferometry, CTD and tide gauge measurements.
- **Moscow Russia, Monitoring of an aquifer in Alexandrovka** Jun 2013
  Deep electrical and seismic methods.
- **Understanding the geology from the Jura to the French Alps** May 2012/13
  Cartography, structural geology, sedimentology, tectonic interpretation.

Teaching Experience

- **Earth System Sciences 19, Oceanography** Irvine, USA
  Faculty advisor: J. Ferguson *Winter 2018*
  – Organize discussions and activities in the field of oceanography at a bachelor level.

- **Earth System Sciences 19, Modeling the Earth** Irvine, USA
  Faculty advisor: M. Prather *Fall 2017*
  – Design laboratory activities in Earth System Sciences field such as sea ice modelling, population growth, greenhouse gases...

- **Earth System Sciences 19, Modeling the Earth** Irvine, USA
  Faculty advisor: M. Morlighem *Winter 2016*
  – Design laboratory activities in Earth System Sciences field such as sea ice modelling, population growth, greenhouse gases... Teaching of an ice core class.

Supervision Experience

- **Supervision of a 6 months internship (Tara Harder)** Irvine, USA
  School: UC, Irvine *Oct–March 2017/18*
  – Design a processing chain to calculate ice velocity fields from historical aerial images (1930-1970).

- **Supervision of a 6 months internship(Valentin Martineau)** Irvine, USA
  School: Ecole Centrale, Paris *Jan–June 2017*
  – Design of processing chain to invert gravity data in the Patagonian ice field.

- **Supervision of a 6 months internship (Vincent Bernier)** Irvine, USA
  School: Ecole Centrale, Paris *Jan–June 2016*
  – Design of processing chain to invert gravity data in Antarctica.

Skills

- **Computing**
  – Programming language: IDL (expert), Python (expert), Matlab (expert), Bash (intermediate), C (basic).
  – Operating System: Linux (expert), MacOS (expert), Windows (expert)

  - Other: $\LaTeX$(expert), Microsoft Office (expert)

- **Geophysical Devices**
  - Ground Penetrating Radar, Magnetometer, Gravimeter, Electric, Seismic.
  - Installation of Automatic Weather Stations on ice in a polar environment
  - Installation of permanent Global Positionning System stations on ice in a polar environment

- **Language**
  - French: native language
  - English: fluent
  - Spanish: proficient (8 years)

Awards and Fellowships

- Best Research Master Thesis of the Région Alsace, France (700 Reward)
- Jenkins Family Graduate Fellowship
- University of California, Irvine Student Spotlight

Others

- Reviewer for *IEEE-Journal of Selected Topics in Applied Earth Observations and Remote Sensing*
- Reviewer for *International Journal of Remote Sensing - Remote Sensing letters*
- Co-organizer of *NASA's Operation Icebridge Meeting* (June 20, Irvine, CA, 2017)
- Co-organizer of *NASA's Ocean Melting Greenland Meeting* (June 21, Irvine, CA, 2017)

Public Outreach

- **CBCnews (interview and online article)** Canada
  As Arctic warms, Canada's glaciers playing major role in sea level rise *Sep-Mar 2015*
- **Globalnews (interview, video documentary and online article)** Canada
  Canada's Arctic glaciers now a major contributor to sea-level rise *Sep-Mar 2015*
- **Vice - Motherboard (interview and online article)** International
  Canada's Melting Glaciers are Causing Sea Level Rise Around the World *Feb 14 2017*
- **ScienceDaily (online article)** International
  Seafloor valleys discovered below West Antarctic glaciers *Jan 18 2017*
- **International Business Times (online article)** USA
  Gigantic valleys [...] revealed beneath West Antarctic Ice Sheet *Jan 2017*

References

- **Eric Rignot** - University of California, Irvine and NASA's Jet Propulsion Laboratory, USA
- **Jeremie Mouginot** - Institut des Géociences de l'Environnement, Grenoble, France
- **Abbas Shfaqat Khan** - DTU/SPACE, Copenhagen, Denmark
- **Noel Gourmelen** - University of Edinburgh, United Kingdom

Activities

- **Sports**
  - Mountain sports : climbing, hiking, mountain biking, slacklining
  - Swimming
- **Music**
  - Trumpet player (17 years) in jazz band and classical orchestra

List of Publications and Communications

M. Wood, E. Rignot, I. Fenty, D. Menemenlis, **R. Millan**, M. Morlighem, J. Mouginot, H. Seroussi (2018), Ocean-induced melt triggers glacier retreat in Northwest Greenland, *Geoph. Res. Lett.* [under review]

R. Millan, E. Rignot, J. Mouginot, M. Wood, A. A Bjørk (2018), Vulnerability of Southeast Greenland glaciers to warm Atlantic water from Operation Icebridge and Ocean Melting Greenland data, *Geoph. Res. Lett.*, 45, doi:10.1002/2017GL076561.

L. An, E. Rignot, J. Mouginot, **R. Millan** (2017), A century of stability of Avannarleq and Kujalleq glaciers, West Greenland, explained using high-resolution airborne gravity and other data, *Geoph. Res. Lett.*, 45, doi:10.1002/2018GL077204.

J. Mouginot, E. Rignot, B. Scheuchl, **R. Millan**, (2017), Comprehensive Annual Ice Sheet Velocity Mapping Using Landsat-8, Sentinel-1, and RADARSAT-2 Data, *Remote Sensing*, *9*(4), 364, doi:10.3390/rs9040364.

M. Morlighem,..., **R. Millan**,..., (2017), BedMachine v3: Complete bed topography and ocean bathymetry mapping of Greenland from multi-beam echo sounding combined with mass conservation, *Geoph. Res. Lett.*, *9*(4), 364, doi: 10.1002/2017GL074954.

L. An, E. Rignot, S. Elieff, M. Morlighem, **R. Millan**, J. Mouginot, D. M. Holland, D. Holland, J. Paden, (2017), Bed elevation of Jakobshavn Isbræ, West Greenland, from high-resolution airborne gravity and other data, *Geoph. Res. Lett.*, doi:10.1002/2017GL073245.

R. Millan, J. Mouginot, E. Rignot (2017), Mass budget of the glaciers and ice caps of the Queen Elizabeth Islands, Canada, from 1991 to 2015, *Environmental Research Letters*, *12*(2), doi:10.1088/1748-9326/aa5b04.

R. Millan, E. Rignot, V. Bernier, M. Morlighem, P. Dutrieux (2017),Bathymetry of the Amundsen Sea Embayment sector of West Antarctica from Operation IceBridge gravity and other data, *Geoph. Res. Lett.*, doi: 10.1002/2016GL072071.

A. Dehecq, **R. Millan**, E. Berthier, N. Gourmelen, E. Trouvé and V. Vionnet (2016),Elevation Changes Inferred From TanDEM-X Data Over the Mont-Blanc Area: Impact of the X-Band Interferometric Bias, *IEEE Journal of Selected Topics in Applied Earth Observa-*

tions and Remote Sensing, *9*(8), 3870–3882, doi: 10.1109/JSTARS.2016.2581482.

R. Millan, A. Dehecq, E. Trouvé, N. Gourmelen and E. Berthier (2015), Elevation changes and X-band ice and snow penetration inferred from TanDEM-X data of the Mont-Blanc area, *Analysis of Multitemporal Remote Sensing Images, 8th International Workshop in Annecy, 2015*, 1–4. doi: 10.1109/Multi-Temp.2015.7245753, (*Conference paper*)

Oral Presentations

R. Millan, E. Rignot, M. H. Wood, J. Mouginot, A. A. Bjørk, M. Morlighem , Vulnerability of SouthEast Greenland glaciers to Atlantic warm water using Operation Icebridge and Ocean Melting Greenland data, *American Geophysical Union, Fall Meeting 2017, New Orleans, USA*.

R. Millan, E. Rignot, J. Mouginot, M. Morlighem, B. Scheuchl, Observation des glaciers et calottes polaires á partir de données satellitaires et aéroportées, *Invited Seminar at University of Grenoble, March 2017, Grenoble, France*.

R. Millan, E. Rignot, J. Mouginot, Remote Sensing of glaciers and ice caps in the Canadian Arctic (March 2017), *Invited Seminar at University of Copenhagen, March 2017, Copenhagen, Denmark*.

R. Millan, E. Rignot, J. Mouginot, D. Menemenlis, M. Morlighem and M. Wood, Retreat of Southeast Greenland glaciers from Operation Icebridge and Ocean Melting Greenland Data, *NASA's Ocean Melting Greenland 2017 Meeting, Irvine, USA*.

R. Millan, E. Rignot, J. Mouginot, D. Menemenlis, M. Morlighem and M. Wood, Bathymetry of Southeast Greenland glaciers from Operation Icebridge and Ocean Melting Greenland Data, *NASA's Operation Icebridge 2017 Meeting, Irvine, USA*.

R. Millan, J. Mouginot, E. Rignot, Mass budget of the glaciers and ice caps of the Queen Elizabeth Islands, Canada, from 1991 to 2015, *American Geophysical Union, Fall Meeting 2015, San Francisco, USA*.

Posters

R. Millan, E. Rignot, J. Mouginot, D. Menemenlis, M. Morlighem and M. Wood, Bathymetry of Southeast Greenland glaciers from Operation Icebridge and Ocean Melting Greenland Data, *NASA's PARCA meeting, Washington DC, USA*.

R. Millan, E. Rignot, J. Mouginot, D. Menemenlis, M. Morlighem and M. Wood, Understanding changes in ice dynamics of southeast Greenland glaciers from high resolution gravimetry data and satellite remote sensing observations,*American Geophysical Union, Fall Meeting 2016, San Francisco, USA*.

ABSTRACT OF THE DISSERTATION

Dynamics of Glaciers and Ice Sheets at the Ocean Margin from Airborne and Satellite Data

By

Romain Millan

Doctor of Philosophy in Earth System Science

University of California, Irvine, 2018

Donald Bren Professor Eric Rignot, Chair

The modern contribution of glaciers and ice sheets to sea level rise increases with time and has largely been attributed to anthropogenic sources. The mass losses through the dynamic discharge of ice into the ocean has played a major role in the last two decades with a widespread acceleration of marine terminating glaciers. Recent studies have shown that these changes are closely linked to the ocean conditions, the bedrock and fjord topography. It is therefore crucial to document in details the evolution of glaciers and ice sheets, the bedrock topography and ocean properties to understand how and why the glaciers have been changing recently. Therefore, the aim of this thesis is to improve our understanding of ice dynamics and ice-ocean interaction by using a set of satellite and airborne remote sensing data over key regions. We describe the evolution of glacier dynamics and the detailed partitioning of the mass losses of the Queen Elizabeth Islands, Canada since the 1990s, which are major contributors to recent sea level rise. In Antarctica, we provide the first map of the sub-ice shelf bathymetry of the largest glaciers in the Amundsen Sea Embayment that reveals deep pathways for circumpolar warm water up to the grounding line of the glaciers. Finally, we assembled a comprehensive map of the bedrock and fjord topography of the Southeastern coast of Greenland, and interpret the pattern of glacier retreat during the last 80 years, which was not possible before. The work proposed help to understand the recent deglaciation history of key regions in the Arctic, Greenland and Antarctica. The new

mapping of sub-ice shelf, bedrock and fjord topography provides invaluable insights for mass balance calculation, ocean and ice-sheet modeling.

Chapter 1

Introduction

The decrease of glaciers and ice sheets observed over the last few decades is the result of current climate change [*Church et al.*, 2011], which is extremely likely caused by anthropogenic sources. As reported by the International Panel for Climate Change (IPCC), it has become a major challenge facing society for the 21st century, with important impacts in terms of sea level rise (SLR), natural hazards, and socio-economic issues related to water resources [*Church et al.*, 2011]. The primary contributions to sea level rise are thermal expansion and the mass loss from the world's glaciers (estimated ice volume: 180 10^3km^3), Antarctica (26.92 10^6km^3) and Greenland (2.99 10^6km^3) [*Morlighem et al.*, 2017; *Fretwell et al.*, 2013]. The two ice sheets holds more than 50% of land-ice[1] and have a potential sea-level equivalent of 7.42 m for Greenland and 58.3 m for Antarctica [*Morlighem et al.*, 2017]. The contribution of great ice sheets to global sea level rise has increased during the last two decades and was 0.43 mm/yr in Greenland and 0.27 mm/yr in Antarctica for the period 1993-2010 [IPCC, AR5]. Accurate observation of the evolution of these ice masses is therefore crucial to draw accurate projections on their contributions to sea level rise. Mountain glaciers and ice caps hold 2.6% of the land ice, with a potential sea level rise equivalent of 0.41 m [IPCC AR5,

[1] outside seasonally frozen ground, seasonal snow cover, ice lakes and rivers

[*Vaughan et al.*, 2013]]. While their share of the total volume of ice on earth is smaller than the two great ice sheets, they have contributed to 0.76 mm/yr (30%) sea level rise for the period 1993-2010, which is larger than both Greenland and Antarctica [IPCC AR5]. Furthermore, the disintegration of mountain glaciers in remote areas threaten local populations by a rarefaction of drinkable water in addition to an increase in devastating glacial lake outburst floods (GLOFs) events [*Riaz et al.*, 2014].

The *mass balance* of glaciers and ice sheets is controlled by the amount of accumulation (through snowfall, refreezing, etc.) and ablation, which mainly occurs through surface melt and dynamic discharge of ice in the ocean for marine terminating glaciers (calving). Thinning of ice is an essential parameter for the initiation of fractures. Calving is therefore closely linked to the flow rate of glaciers that can increase longitudinal stretching with high velocities [*Cuffey*, 2010]. The dynamic ice discharge of glaciers controls $\sim$ 40-50% of the mass losses of the GrIS [*Andersen et al.*, 2015] and is largely dominant in Antarctica, where surface melt only plays a minor role. Hence, with increasing mass losses from glaciers and ice sheets, the acceleration of glaciers is a significant response to climate change. For glaciers and ice caps, this component has so far been under-documented. Also, the partitioning of mass losses between SMB and ice discharge is less clear. In this thesis, we will discuss both the dynamic component of mass loss as well as their contribution to the total mass budget.

The *bedrock topography* is defined as the shape and elevation of the bed under the grounded portion of a glacier. *Sub-ice shelf bedrock topography* will be referred in this thesis as the elevation of the seafloor under ice shelves[2] or floating ice tongues. Finally, *seafloor bathymetry* is the depth and shape of the seafloor. The work proposed by Schoof in 2007 focused on the

[2] *Ice shelves* are glacier termini portions that are floating. In Antarctica, ice shelves represent an area of 1.6 million square kilometers ($\sim$ size of the Greenland Ice Sheet) and surround 75% of the coastline [*Rignot et al.*, 2013]. These floating extensions play a crucial control on glacier stability and ice-sheet mass balance as they act as a buttress from the flow of upstream glaciers, hence slowing them down [*Cuffey*, 2010; *Jacobs et al.*, 2011]. The shape of the seafloor under ice shelves and in front of glacier termini have the potential to bring warm ocean water that has the potential to melt the glaciers and ice shelves from below

so-called **Marine Ice Sheet Instability** (MISI), that suggests that reverse bed slopes have the potential to unground and destabilize glaciers. Initially, the ungrounding of glaciers is caused by melting and thinning, which is likely coming from surface melt [*Box et al.*, 2006] but also from warmer ocean temperatures that undercuts the ice faces and can trigger significant glacier retreat [*Rignot et al.*, 2016]. This was later observed in the Amundsen Sea sector, Antarctica, where large glaciers that accelerated during the last ten years were retreating at an alarming rate on retrograde slopes [*Rignot et al.*, 2014]. The cause of the ungrounding of these glaciers has later been attributed to warmer Circumpolar Deep Water (CDW) [*Jacobs et al.*, 2011], that has enhanced sub-ice shelve melting and reduced buttressing, which has led to an increase in ice velocity and widespread retreat of the glaciers since the early 1990s [*Rignot et al.*, 2014]. In Greenland, similar observations have shown that the response of marine terminating glaciers to climate warming was likely due to a complex relationship between bed topography, ocean-induce melt, increasing runoff and the supply of ice from upstream [*Straneo et al.*, 2010] [*Rignot and Mouginot*, 2012]; *Holland et al.*, 2008]. These observations have highlighted the strong link between the ice dynamics and the bedrock topography that has the potential to (1) channel warm ocean water to the ice-ocean boundary (grounding line, ice front termini) and (2) stabilize (in case the glacier is standing on a sill) or enhance (in case the glacier is standing on a retrograde slope) glacier retreat and reduce buttressing, leading to an acceleration in glacier flow and increase mass losses. Hence, a precise knowledge of the ice flow, bedrock topography, and ocean properties is essential to document and understand precisely the evolution of the ice masses.

In the following sections, we will describe the regions of interest (Figure 1.1), the techniques that will be used in this study to document changes in ice dynamics and map the bedrock and fjord topography and finally, we will present the outlines of this project.

1.1 Regions of Interest

The **Queen Elizabeth Islands** are located in the Northern part of the Canadian Arctic Archipelago. They are divided into eight major ice caps and ice fields with more than 4500 land-terminating and marine terminating glaciers flowing at their periphery. Satellite gravimetry and surface mass balance models from re-analysis data have shown that this area was losing mass at increasing rates between 2004 and 2011, with the largest rate of mass losses after Greenland and Antarctica [*Gardner et al.*, 2011; *Lenaerts et al.*, 2013]. While half of the total ice area is drained by marine terminating glaciers, the contribution of ice dynamics to the total mass losses has however been largely under-documented and limited in time [*Gardner et al.*, 2011; *Van Wychen et al.*, 2014, 2016]. It is therefore crucial to document in details the changes in ice dynamics and the partitioning of the mass losses to understand how the region has been evolving through time and to identify the physical processes behind those changes.

The **Amundsen Sea Embayment** in the West Antarctic Ice Sheet (WAIS) is a major contributor to sea level rise. This area is drained by the fastest marine-terminating glaciers on Earth: Pine Island, Thwaites, Smith, Pope and Kohler glaciers, that are the largest contributor to sea level rise in Antarctica. The ice dynamics from these glaciers have been well documented in recent years: the total ice discharge has increased by 77% since 1973 and glaciers were ungrounded from their stabilizing positions and started retreating tenth of kilometers inland on reverse bed slopes [*Mouginot et al.*, 2014; [*Rignot et al.*, 2014], *Scheuchl et al.*, 2016; [*Favier et al.*, 2014]. While consequent amount of bathymetric data has been produced, and assembled on land and offshore, the sub-ice shelf bathymetry of those glaciers remains however unknown and has hampered the study of ice-ocean interactions in this region.

Southeast Greenland is a highly dynamic region characterized by high accumulation rates (mainly through snowfall). This area hosts the fastest moving glaciers of the GrIS (KøgeBugt, Helheim, Ikertivaq) that have flowing rates that can reach more than 10 km/yr. Between 1994 and 1999, this region was a major contributor to sea level rise with significant rates of thinning observed from satellite altimetry [*Krabill et al.*, 1999]. Such changes could not be explained by surface melt alone and suggested a significant contribution from ice dynamics. During the last two decades, several studies have observed distinct pattern of changes in glacier dynamics from one fjord to the next, which indicates different responses to climate forcing at the fjord level [*Bjørk et al.*, 2012; *Howat et al.*, 2008]. In this region, the Irminger current branches off the North Atlantic current and has the potential to fuel high melt rates along glacier margins [*Christoffersen et al.*, 2011; *Murray et al.*, 2010]. The interpretation of the changes in this region has however been hampered by a dearth in bedrock topography and fjord bathymetry data. Offshore, most fjords have not been mapped due to the presence of large iceberg debris in front of the glaciers. On land, radar depth sounder techniques have failed to map the bedrock topography accurately which has induced large uncertainty in Mass-Conservation (MC) reconstruction but also in dynamic ice discharge and ultimately mass-balance estimations [*Morlighem et al.*, 2017]. Hence, accurate ice thickness and fjord bathymetry are essential to (1) understand the changes in dynamics of these glaciers and (2) estimate accurately the mass losses from this sector.

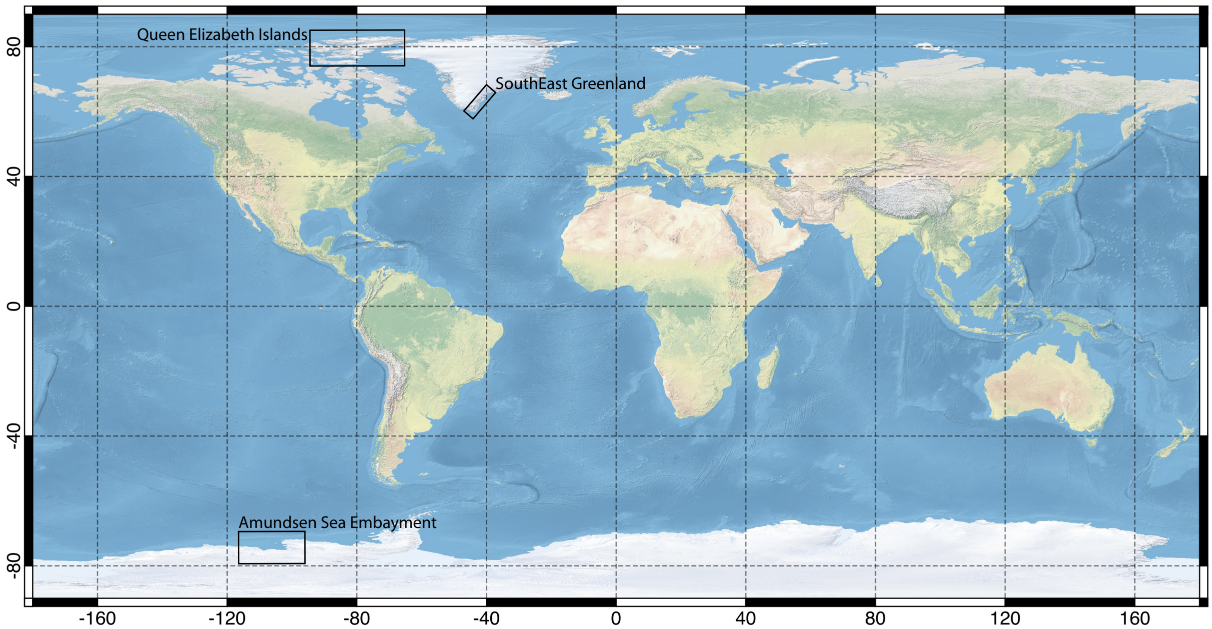

Figure 1.1: *Study regions that will be presented in this thesis.*

1.2 Recent advances in the observation of glaciers and ice sheets

1.2.1 Observation of ice dynamics from satellite remote sensing data

The recent launch of satellites orbiting around the earth has fundamentally changed the way we observe glaciers and ice sheets. While ground-based measurements are spatially limited as well as time and resource intensive, satellite observation have revealed to be perfectly suited for the study of glaciers and ice sheet. Through systematic acquisition of data over vast regions on a regular and repetitive basis over long time-period, these new spaceborne technologies enabled the monitoring of ice masses on continental scales in extraordinary detail [*Rignot*, 2008; *Rignot and Mouginot*, 2012]. For the study of ice dynamics and specifically ice velocity mapping, we distinguished two type of satellite data that will be used in this thesis: *optical* and *Synthetic Aperture Radar* data that are described below.

Optical data. Optical imagery, like ground or airborne photography, uses the reflexion of solar radiation in the visible and infrared domain. This imaging method is only working when the solar illumination is sufficient and when clouds are absent. Optical images can be both use to determine ice flow, with the recognition of surface features (feature-tracking) [*Scambos et al.*, 1992], or to perform land-classication, using band-ratio [*Campbell and Wynne*, 2011]. The USGS Landsat program was initiated in the early 1970s (Landsat-1 was launched in July 1972) and has been providing data on an ongoing basis since then. Now in its eighth generation, the Landsat program has been technically improved over time and its latest satellite has proven to be an asset for glacier and ice sheet research. USGS has committed resources to acquire large amounts of Landsat-8 data over glaciers and ice sheets making Landsat-8 and important resource for researchers. While older Landsat satellites are more challenging in terms of processing, they provide some information to extend the satellite record into the past further than any other satellite mission. Another important optical resource is the Worldview program. These high-resolution satellites collect data in sub-meter resolution in stereo acquisition mode provide an opportunity to generate high resolution digital elevation models. Thanks to a commitment by National Geospatial Intelligence Agency to collect Worldview data in polar regions through the NextView License program and by NASA, Worldview has revolutionized Digital Elevation Models in the Arctic through the availability of open-access accurately time-tagged surface elevations at a resolution of 50-cm [*Howat et al.*, 2014].

Synthetic Aperture Radar (SAR) data. SARs are active instruments that work independent of daylight or cloud cover, making them a key asset in polar regions where solar illumination is absent during winter and clouds are a frequent occurrence. In contrast to nadir looking instruments (like Landsat for example), SARs are side looking sensors, they generate a pulse train of electromagnetic waves that is scattered on the earth's surface with a portion of the signal being reflected back in the direction of the satellite. Measuring the reflection results in two types of information: the amplitude of the reflected electromagnetic signal and its phase, which is a proxy for the distance between the sensor and the point on the ground. This information is stored into a complex image which is commonly referred to as *Single Look Complex* (SLC). Single image analysis is usually restricted to the amplitude only, however, when multiple images are available, phase information becomes an important information source that is sensitive to displacement (i.e. motion on the ground) as well as elevation. SAR therefore has capability to measure simultaneously surface elevation and ice velocity independently of the weather conditions and with extraordinary detail and precision in the range of millimeters for ice velocity and sub-meter for surface elevations [*Joughin et al.*, 2000; *Jaber et al.*, 2013].

During the last two decades, Synthetic Aperture Radar (SAR) have revolutionized the measurements of ice flow and surface elevation. In 1997, the Canadian Space Agency launched the Antarctic Mapping Mission -1, that used SAR images to assemble the first mosaic of Antarctica (Figure 1.2), that had remained one of the most poorly mapped region in the world, due to important cloud cover, high winds and complete night during polar winter. The complete mapping of the Earth South pole was done using a unique technology onboard RADARSAT-1 satellite that allowed him to change the look direction of the SAR, which was not possible before. This mission provided the first high resolution map of the continent and served as a milestone for study of the polar ice sheets.

Measuring ice velocity. The most common way to measure ice velocity using optical images is to track surface features such as crevasses or séras that are conserved between two acquisition, it is referred as *feature tracking*. In the beginning, image matching was

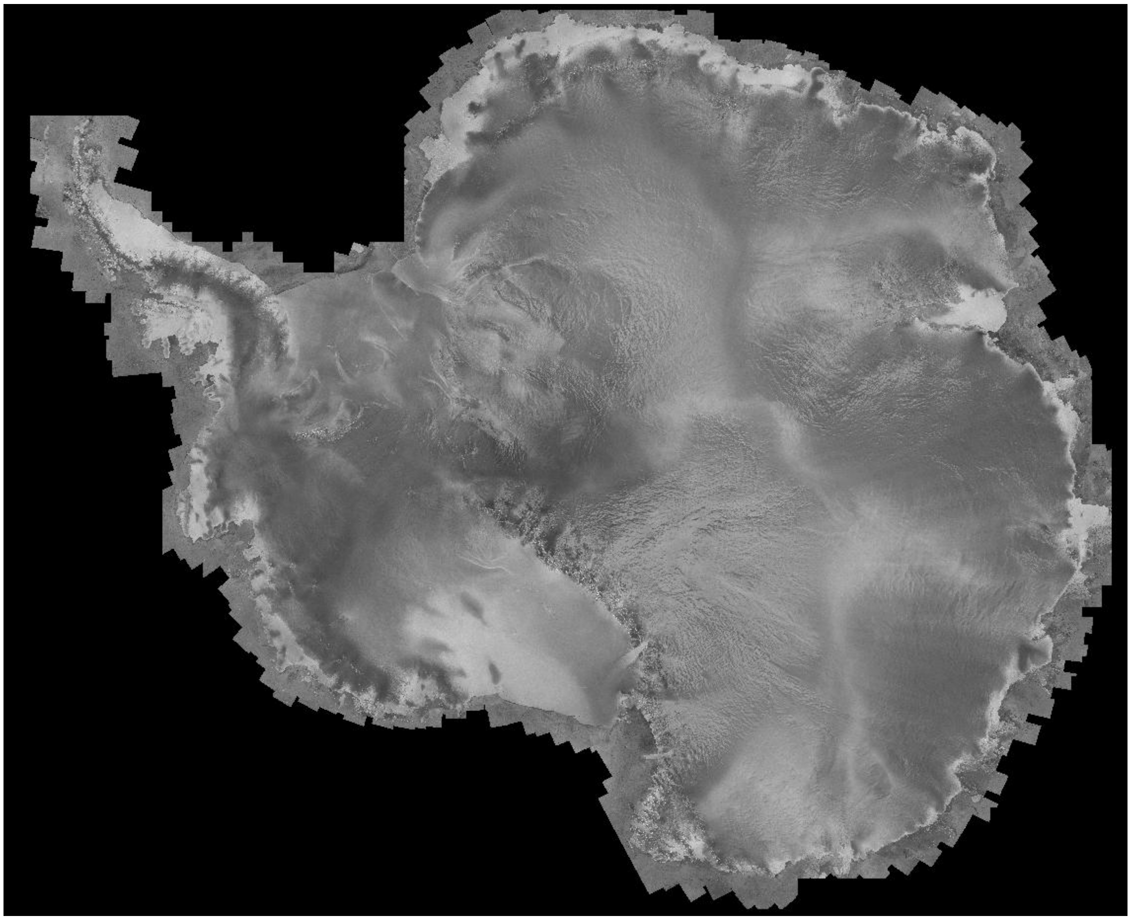

Figure 1.2: *Synthetic Aperture Radar amplitude mosaic obtained from RADARSAT-1 satellite observations. Source: http://www.asc-csa.gc.ca*

performed manually, but rapidly, automatic methods using cross-correlation techniques and Fast-Fourier transforms were developed [*Scambos et al.*, 1992].

Speckle appears as a granular pattern on SAR images and is attributed to the interference of the waves reflected from numerous scatterers on a surface. The classic way in SAR processing is to considered speckle as noise and to minimize its effect by using a compression in azimuth and range direction. However, in interferometric conditions of acquisitions, speckle is conserved between two images. Thus, it is possible to use a cross-correlation algorithm on this phenomenon in full resolution to track glaciers movement. Although less accurate (comparable with the size of the matching window used) than conventional SAR interferometry (few cm in the line-of-sight direction), speckle tracking can yield complementary and additional two-dimensional ice motion information where InSAR analysis breaks down [*Michel and Rignot*, 1999]. Finally, *feature Tracking* is used with optical imagery and uses the same principles as *speckle tracking* buy tracking surface features such as crevasses or seracs that are conserved between two acquisitions instead of speckle.

The principle of *SAR interferometry* (InSAR) is based on the phase difference of two radar images of the same zone acquired with the same geometry i.e. same orbit and incidence angle. The difference between two phases is called an *interferogram* and represents a fraction of a wavelength which is a highly accurate measurement of the change in length between the target and the satellite, and ultimately a measure of the displacement in the line-of-sight of the spacecraft (Figure 1.4). Two types of acquisition can be distinguished: *repeat path*, where images are acquired at different dates (e.g. ERS, RADARSAT...) used from ice displacement calculation and *single path*, where images are acquired at the the same time (SRTM, TanDEM-X) which is mostly used to retrieve topography. The use of traditional interferometric processing to determine ice flow is reasonable in low accumulation regions (<15 cm/yr) such as central Antarctica (Gray et al. (1999)). In higher accumulation area (>30 cm/yr), temporal decorrelation occurs when the time between two acquisitions is greater than 1-3 days [*Lubin and Massom*, 2005]. This is a major limitation, given the large repeat-cycle of satellites (24 days for RADARSAT-1, 35 days for ERS-2, 46-days for ALOS) and complicates the computation of ice motion from phase differencing [*Gray et al.*, 1999].

During the last decade, significant improvements have been made in mapping surface ice flow of glaciers and ice sheets. In 2006, the first map of surface ice flow using radar interferometry at a continental scale, was published for all glaciers at the periphery of Antarctica [*Rignot*, 2006]. Five years later, thanks to launch of new satellites, such as ENVISAT-ASAR, RADARSAT-2 and ALOS PALSAR, a comprehensive map of the flow of the entire ice sheet

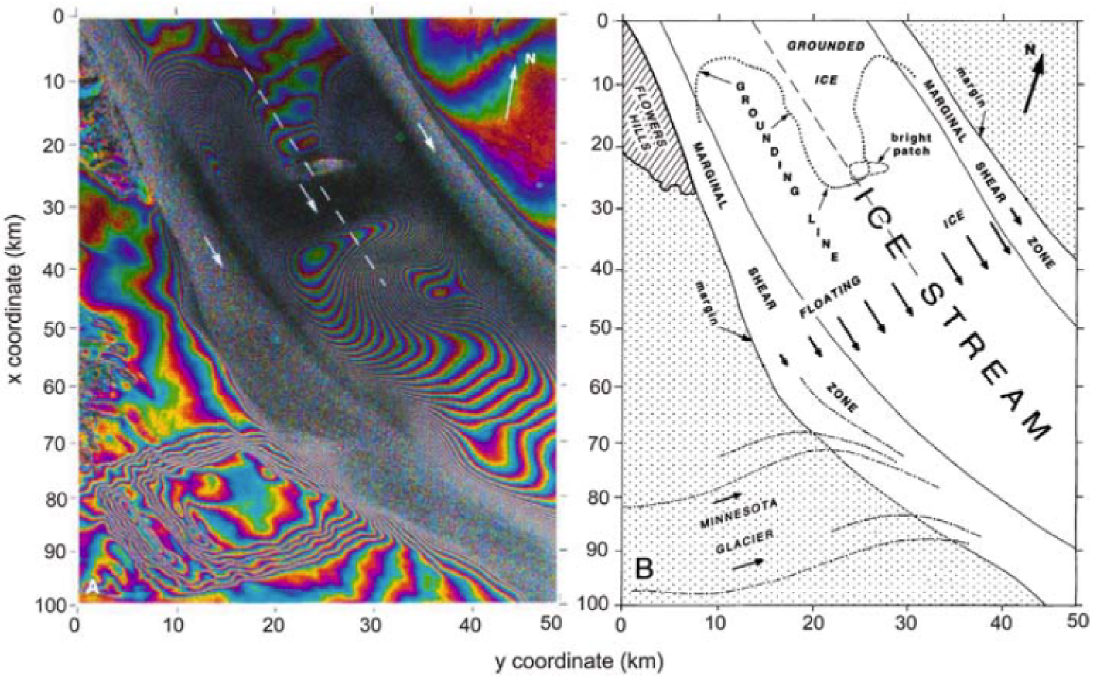

Figure 1.3: *Interferogram of surface ice velocity of Rutford Ice Stream, Antarctica calculated from two ERS C-band (7.5 cm wavelength) SAR scenes [Goldstein, 1993] 1993. The color fringes represent the ice motion toward or away from the spacecraft. A color cycle (yellow to blue) represent a 2.8-cm change in the line of sight direction (half the wavelength of ERS C-band).*

was produced [*Rignot and Mouginot*, 2012]. Same progress was made in Greenland in the same timeframe [*Joughin et al.*, 1997, 2010; *Rignot and Mouginot*, 2012]. These scientific advancements have extensively improved our understanding of the dynamic of the great ice sheets and their contribution to sea level rise. Moreover, large scale ice velocity maps have been extensively used for ice-sheet numerical modeling and specifically to reconstruct bedrock topography under the ice using a Mass-Conservation (MC) approach [*Morlighem et al.*, 2014], which is essential to understand past, present and future evolution of glaciers.

Large scale observation of glaciers and ice caps ice velocity from space has however been more recent. The first regionally comprehensive map of surface glaciers velocities in Alaska, Patagonia and the Canadian Arctic Archipelago have only been published in 2013, 2015

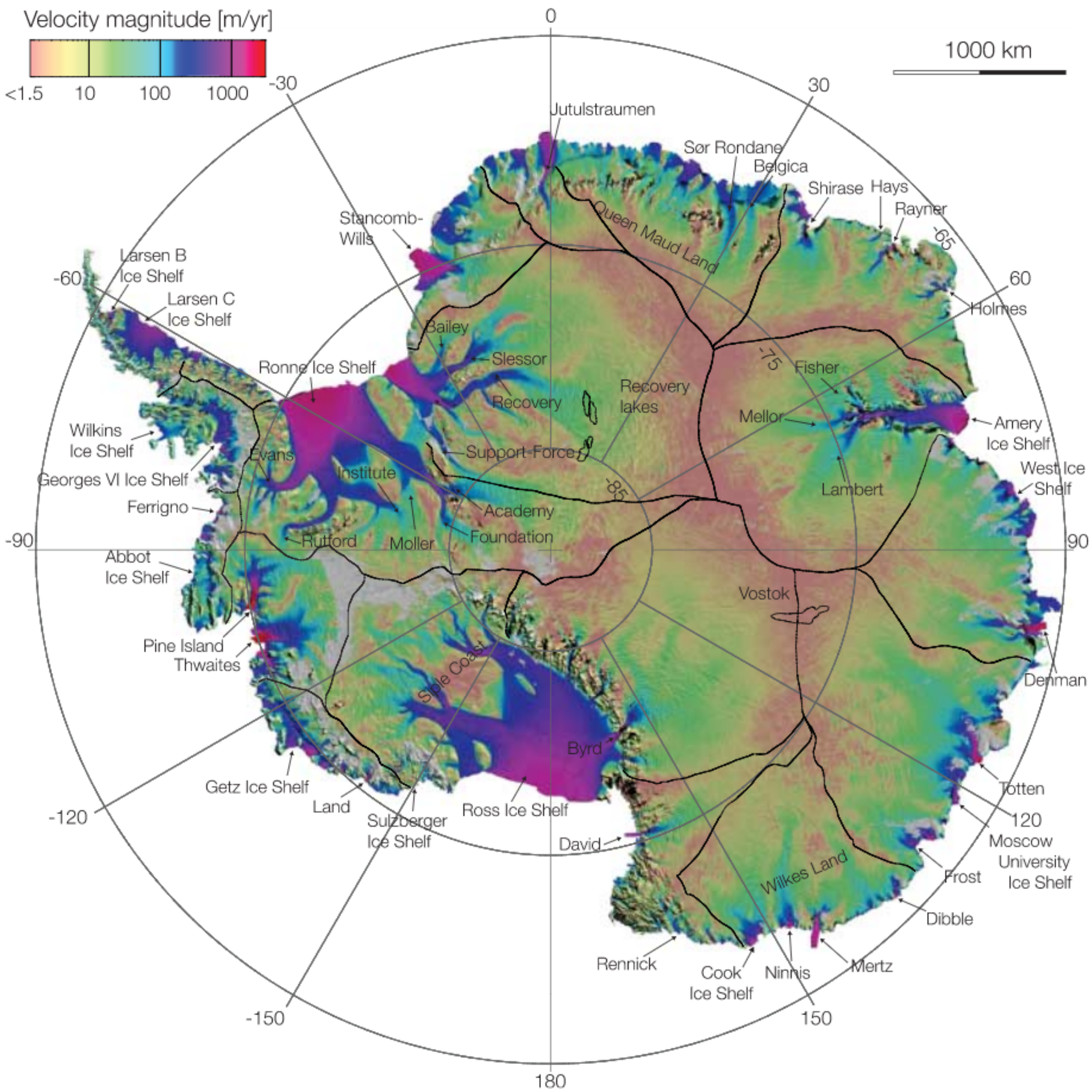

Figure 1.4: *Antarctic ice velocity derived from ALOS PALSAR, Envisat ASA, RADARSAT-2 and ERS-1/2 satellite radar interferometry [Rignot et al., 2011].*

and 2014 respectively [*Burgess et al.*, 2013; *Mouginot and Rignot*, 2015; *Van Wychen et al.*, 2014], which is more than one decade later than the great ice sheets. This has been in part due to a larger interest in surface processes but also more difficult terrain conditions (steep topography) that makes the use of satellite techniques more challenging. To this day, ice flow measurements in this region remain limited in time and more data are needed to analyze and understand the changes in ice dynamics of these sectors.

The Input-Output Method. In order to calculate the net mass loss or gain of glaciers and ice sheets it is necessary to determine the mass-balance, which is defined as the *Surface Mass Balance* (input) minus the *ice discharge* (output).

The surface mass balance is determined using regional climate models from re-analysis data. The most notorious ones are the Regional Atmospheric Climate Models (RACMO) developed by the Royal Netherlands Meteorological Institute (KNMI) [*Ettema et al.*, 2009] and the Modele Atmospherique Régional (MAR) from the University of Liege, Belgium and University of Grenoble, France. The models have the capacity to produce SMB on a daily basis between 1960 and present, by subtracting the total runoff and sublimation from total snowfall and rainfall [*Ettema et al.*, 2009]. Finally, the ice discharge is defined as the mass of ice passing through of flux gate at the grounding line or close to the termini of the glacier. The calculation of ice discharge requires information on the ice flow (from interferometry, speckle and feature tracking) and on the ice thickness at the grounding line (from radar depth sounder). The ice discharge is calculated as:

$$D = \rho_{ice} \int_B^S v(z)dz = \rho_{ice}\bar{v}H \qquad (1.1)$$

where D is the ice discharge in Gigaton per year, ρ_{ice} is the density of the ice, v is the rate of flow integrated from the base of the glacier B, to the surface S, $\bar{v}$ is the depth averaged ice velocity in meters per year and H is the ice thickness.

1.2.2 Mapping bedrock elevation and fjord bathymetry using airborne gravity measurements

The most common and precise way to measure ocean bathymetry is through echo sounding technique. The use of this technique on global scales is however costly and timely expensive so that it would take about 200 years to survey the deep ocean (and even more for coastal areas) [*Carron et al.*, 2001; [*Smith and Sandwell*, 2004; *Cochran and Talwani*, 1977]. Most of the global ocean bathymetry maps come from gravity-based models [*Sandwell et al.*, 2014] The use of gravity data for topographic mapping has been largely discussed during the last centuries: in 1876, Siemens was the first to suggest the use of gravity anomalies to map the ocean floor, even though such experiments were difficult to conduct at that time because of a lack in technological advances [*William*, 1876]. During the last two decades, advanced technologies allowed us to use gravity observations from space to improve ocean bathymetry mapping [*Baudry et al.*, 1987; *Smith and Sandwell*, 2004; *Sandwell et al.*, 2014] but also for the study of glacial isostasy [*Small and Sandwell.*, 1989; *Watts and Cochran*, 1974], plate tectonics [*Wessel and Haxby.*, 1990] and oil and gas exploration [*Paterson and Reeves*, 1985].

The Gravity Potential Theory. The gravity force is based on the gravitational effect that attracts bodies toward each other. The density of an object (product of mass and volume) is the source of the gravity field and can be directly linked to variations in the topography and geology. The force of gravity can be observed between the earth and the moon or the earth and the sun, but not between objects at the surface of our planet because their mass is negligible in comparison. The force of attraction between two objects has been showed by Newton in the seventeenth century with the well-known Newton's third law formula:

$$F_g = G\frac{m_1 m_2}{r^2} \qquad (1.2)$$

where r is the distance between the two objects, m_1 is the mass of object 1, m_2 the mass of object 2 and G the universal gravitational constant equals to $6.674215^{-11} N \frac{m^2}{kg^2}$. For the purpose of geophysical explorations, we measure the gravitational acceleration defined by Newton's second law as:

$$g = \frac{F_g}{m_1} \qquad (1.3)$$

This quantity **g** is measured in m/s^2 or more commonly in **milligals (mGal)** (named after Galileo Galilei, which established the first principles of gravity fields) where **1 mGal = $\mathbf{10^{-5}}$ m/s^2**, which is closer to the change in gravity field caused by variations in subsurface densities.

Measuring gravity. There is two types of gravity measurements: absolute measurements that directly measures the time for an object to free fall and which gives you the actual value of the gravity field in one location, without reference to previous measurements. *Absolute values* are free of any drift and useful for instrument calibrations and studies of the Earth's gravitational field. These measurements are however limited because they are time consuming, gravimeter are too large, expensives and not necessary for geophysical explorations. For most geophysical purposes, *relative measurements* are used. Such gravimeter can only measure the difference in gravitational acceleration between one place and another. The principle used for this technique is to measure the change in length of a spring attached to an object of constant mass inside the gravimeter at different locations relative to a reference station. Finally, the change in spring length is converted to gravitational acceleration through a calibration constant.

Extraneous gravity variations. Gravity measurements are affected by different effects

Figure 1.5: *Airborne gravity survey aircraft for data acquisition in Southeast Greenland by Sander Geophysics. The gravimeter was installed in the rear cabine of the aircraft. (source: SGL technical report)*

apart from the local geological conditions that are the mapping goals of the gravity surveys. Hereafter, the term **gravity anomalies** will refer to the measured gravity corrected from the summation of several planetary effects. A good example is the variation of the gravitational field from the poles to the equator due to a change in the radius of the earth (∼21-km using the best-fitted shape of the Earth i.e. the ellipsoid): this is referred as the **normal gravity calculation**. Also, as the measurements are not always done at the surface of the ellipsoid, the gravity observations are varying with height: the correction for this effect is called the *Faye's* or *free-air correction* because it assumes there is only air between the point of observation and the ellipsoid and does not account for the attraction of the masses. The removal of the influence of the masses (Figure 1.6), is taken into account in the *Bouguer correction*, but will not be considered here, because it is used for the purpose of topographic mapping.

Gravity inversion for topography mapping. The inversion is the step that allows us to pass from gravity measurements to a new and more accurate map of the topography.

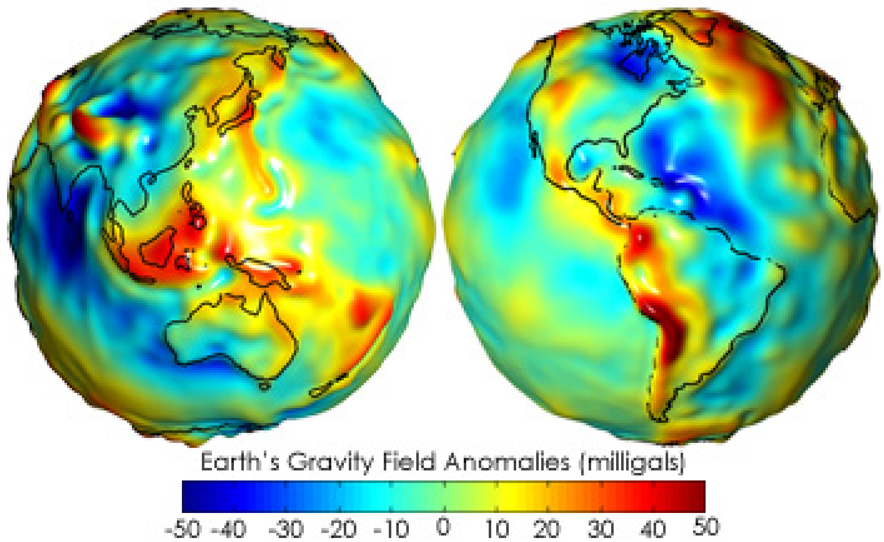

Figure 1.6: *Earth's gravity field anomalies due to the shape and attraction of masses of the earth (Geoid) in mGals measured from the GRACE satellite (source: earthobservatory.nasa.gov)*

It is initiated by a first guess model that is composed of three layers: an ice layer with a density of 0.917g/cm^3, a sea water layer with a density of 1.028 g/cm^3 and a bedrock layer with a density of 2.67 g/cm^3. We calculate the gravity generated by this model (*forward calculation*) and compare it to the measured airborne free-air anomalies. Traditionally, the initial model was decomposed into smaller prism from which people calculated separately the gravity anomaly, and sum it up at the end. When models are complicated, this method is however very time consuming because the calculation time is proportional to NxN, where N is the number of point defining the model [*Grant and West.*, 1965; *Garland et al.*, 1965]. In this thesis, the calculation of gravity anomalies implements the method of Robert Parker developed in 1973. The representation of gravity and magnetic anomaly using this scheme is particularly fast (calculation time proportional to Nxln(N)) because it uses an ingenious factorization method that was highlighted in a special issue of IEEE in 1967. The gravity anomaly from a relief on an horizontal interface is expressed in terms of powers of the Fourier transform of the topographic relief as:

$$F[\Delta g(x\pm, y)] = -2\pi G\rho e^{-kz_0} \sum_{n=1}^{\infty} \frac{k^{n-1}}{n!} F[h^n(x, y)] \qquad (1.4)$$

where F is, the Fourier transform of the quantity into brackets, $\Delta g(x \pm y)$ is the gravity anomaly, h is the depth of the interface, ρ is the density variations across the interface, k is the wavenumber and z_0 is the average depth of the interface. Finally, the initial bedrock is modified iteratively until we find the best match between the modeled and the observed gravity (averaged difference below 0.1 mGal).

The use of airborne gravity observations to map sub-ice shelf, fjord and glacier bedrock topography is a new approach that has not been extensively developed in the literature. In 2004, the first mapping of Lake Vostok's water cavity in East Antarctica was proposed using airborne measurements of gravity and revealed two sub-basins separated by a ridge [*Studinger et al.*, 2004]. Similar mapping has been performed on the Larsen C Ice Shelf and Thwaites glacier in Antarctica [*Tinto and Bell*, 2011; *Cochran and Bell*, 2012] and in the periphery of Greenland's marine terminating glaciers [*Boghosian et al.*, 2015]. These studies however lacked of spatial constraints (2-D vs 3-D) that are essential to relate ice dynamics to bedrock topography [*Tinto and Bell*, 2011; *Cochran and Bell*, 2012] and spatial resolution that smoothes and underestimate the depth of topographic features under Greenland's smaller outlet glaciers [*Boghosian et al.*, 2015].

1.3 Research objectives and outline of the dissertation

The science objective of this thesis is to **improve our understanding of ice dynamics and ice-ocean interactions** in order to understand *How* and *Why* the glaciers and Ice Sheets have been changing throughout time. This science objective is assessed using a multi-sensor approach that combines satellite remote-sensing, airborne gravity, regional climate models and field measurements. We identified three key regions where fast changes are happening and where more observations are needed to better understand ice dynamics and ice-ocean interactions:

- The Queen Elizabeth Islands, which represents the largest source of mass loss of any glacier system outside of the ice sheets, with little to no information on the role of ice dynamics on the total mass budget
- The Amundsen Sea Embayment, which hosts some of the fastest glaciers that contributes the most to sea level rise in Antarctica. The sub-ice shelve bathymetry remain however unknown and can control the amount of warm water melting the grounding line.
- SouthEast Greenland, the first sector to experience a large increase in mass loss in the early 1990s, where no data are available on the bathymetry and bedrock topography which has hampered our interpretation of retreat pattern and mass balance estimations

The technical objectives for each of these regions are as follow:

- Reconstruct the accurate partitioning of the mass losses of the Queen Elizabeth Islands between 1991 and present
- Accurately map the sub-ice shelves cavities of the Amundsen Sea Embayment
- Generate a comprehensive map of bedrock and fjord topography, document the ice front positions since the 1930's and re-estimate the ice discharge of Southeast Greenland glaciers

In **Chapter 2**, we focus on the changes in dynamics of the glaciers and ice caps of the Queen Elizabeth Islands, Nunavut, Canada that has never been documented on decadal to multi-decadal time scales. For this study, we use all the library of Synthetic Aperture Radar and optical data to calculate the changes in ice dynamics of all the glaciers in the region. Finally, we combine those estimates with ice thickness estimations from NASA's Operation Icebridge and the regional atmospheric climate model RACMO to accurately estimate the partitioning of mass losses since 1991. This work was published as:

R. Millan, J. Mouginot, E. Rignot (2017), "Mass budget of the glaciers and ice caps of the Queen Elizabeth Islands, Canada, from 1991 to 2015", *Environmental Research Letters*, **12**, doi:10.1088/1748-9326/aa5b04.

In **Chapter 3**, we design a processing chain to map unknown sub-ice shelf cavity using airborne gravity data. We process NASA's Operation Icebridge free-air gravity anomalies to map the bathymetry under the floating ice tongue of major glaciers in west Antarctica: Pine Island, Thwaites, Crosson and Dotson. This work was published as:

R. Millan, E. Rignot, V. Bernier, M. Morlighem, P. Dutrieux (2017), "Bathymetry of the Amundsen Sea Embayment sector of West Antarctica from Operation IceBridge gravity and other data", *Geophysical Research Letters*, **44**, 1360-1368, doi: 10.1002/2016GL072071.

In **Chapter 4**, we work on understanding the changes in ice dynamics of Southeast Greenland glaciers. We analyze Operation Icebridge and Ocean Melting Greenland data to provide an accurate and comprehensive map of the bedrock topography and fjord bathymetry. This new map is combined with historical ice front position to understand the evolution of these glaciers. Surface ice velocity derived from satellite imagery and a digital elevation model is used to re-estimate the ice discharge contribution of this sector of Greenland. This work was published as:

Millan R., E. Rignot, J. Mouginot, M. Wood, A.A Bjørk, and M. Morlighem (2018), "Vulnerability of Southeast Greenland glaciers to warm Atlantic Water from Operation IceBridge and Ocean Melting Greenland data", *Geophysical Research Letters*, **45**, doi:10.1002/2017GL076561.

Chapter 2

Mass budget of the glaciers and ice caps of the Queen Elizabeth Islands, Canada, from 1991 to 2015

R Millan, J. mouginot, E. Rignot

As presented in:

R. Millan, J. mouginot, E. Rignot (2017), Mass budget of the glaciers and ice caps of the Queen Elizabeth Islands, Canada, from 1991 to 2015, *Environmental Research Letters*, 12, 024016

Abstract

Recent studies indicate that the glaciers and ice caps in Queen Elizabeth Islands (QEI), Canada have experienced an increase in ice mass loss during the last two decades, but the contribution of ice dynamics to this loss is not well known. We present a comprehensive mapping of ice velocity using a suite of satellite data from year 1991 to 2015, combined with ice thickness data from NASA Operation IceBridge, to calculate ice discharge. We find that ice discharge increased significantly after 2011 in Prince of Wales Icefield, maintained or decreased in other sectors, whereas glacier surges have little impact on long-term trends in ice discharge. During 1991-2005, the QEI mass loss averaged 6.3$\pm$1.1 Gt/yr, 52% from ice discharge and the rest from surface mass balance (SMB). During 2005-2014, the mass loss from ice discharge averaged 3.5$\pm$0.2 Gt/yr (10%) versus 29.6$\pm$3.0 Gt/yr (90%) from SMB. SMB processes therefore dominate the QEI mass balance, with ice dynamics playing a significant role only in a few basins.

2.1 Introduction

The glaciers and ice caps of the Queen Elizabeth Islands (QEI), Canada cover an area of 105,000 km^2, which represents 25% of the Arctic land ice outside Greenland [*Lenaerts et al.*, 2013; *Van Wychen et al.*, 2014]. This region is divided into eight major ice caps and ice fields: 1) Northern Ellsmere Icefield (NEI), 2) Agassiz Ice Cap, 3) Prince of Wales Icefield (POW), 4) Devon Ice Cap (DIC), 5) Müller Ice Cap, 6) Steacie Ice Cap, 7) Sydkap Ice cap, and 8) Manson Icefield (Figure B.3). Time series of time-variable gravity and altimetry data indicate that the mass loss from QEI increased significantly to an average of 39$\pm$9 Gt/yr for the time period 2004-2009, mostly the result of ice melt by warmer surface air temperature [*Gardner et al.*, 2011]. A combination of surface mass balance (SMB) output products from the Regional Atmospheric Climate Model Version 2 (RACMO-2) and in-situ observations suggest that the QEI was close to a state of mass balance before year 2000 and started to lose mass from enhanced runoff after 2005 at an average rate of 35 $\pm$ 18Gt/yr for the time period 2005-2011 [*Lenaerts et al.*, 2013].

Complete mapping of 2012 ice velocity [*Van Wychen et al.*, 2014] suggested that the loss from ice discharge is small compared to enhanced runoff and less than 10% of the total mass balance [*Gardner et al.*, 2011; *Van Wychen et al.*, 2014; *Short and Gray*, 2005; *Van Wychen et al.*, 2016]. The Randolph Glacier Inventory (RGI 3.2) [*Pfeffer et al.*, 2014], however, indicates that about half of the QEI is drained by marine-terminating glaciers: 254 marine terminating glaciers drain an ice area of 48,360 km^2 versus 4,284 land-terminating glaciers draining an area of 56,513 km^2. Changes in ice dynamics of tide-water glaciers may play a strong role in the mass balance of the QEI. In Greenland, for instance, 40-50% of the mass loss is driven by the flow of marine-terminating glaciers, with the rest of the mass loss being controlled by an increase in runoff [*Rignot*, 2008]. It is therefore of interest to investigate the partitioning of the mass balance of the QEI glaciers and extend the current time series over several decades to understand how it has been evolving with time and identify the physical processes behind those changes.

Here, we present a comprehensive analysis of the tidewater glaciers in the QEI between 1991 and 2015, including Devon Ice Cap, one of the largest contributors to ice discharge in this region, hence significantly expanding upon recent time series [*Van Wychen et al.*, 2016]. We combine ice velocity from satellite data with ice thickness data from NASA's Operation IceBridge (OIB) from year 2012 and 2014 and surface mass balance (SMB) output products from RACMO-2.3 to determine the mass balance of the QEI, its temporal evolution over the last 25 years, and the exact partitioning of the mass loss between ice dynamics and surface mass balance processes, which has never been directly measured before on such time period. We conclude on the relative importance of ice dynamics in the overall mass budget of the QEI over the last 25 years.

2.2 Data and Methods

2.2.1 Ice discharge

We use Synthetic Aperture Radar (SAR) and optical data from the Japanese L-band sensor ALOS/PALSAR radar satellite (23.6 cm radar wavelength) collected between 2006 and 2011, the Canadian RADARSAT-1 data acquired in C-band (5.6 cm radar wavelength) between 2000 and 2004, the European ERS-1 C-band from 1991 (9 and 12 days repeat cycles), Sentinel 1-a C-band for winter 2015-2016, and the US Landsat 7/8 satellites from 2000 to present (satellite tracks are shown Figure A.1). A speckle tracking algorithm [*Michel and Rignot*, 1999] for ALOS, ERS-1, RADARSAT-1, Sentinel 1-a and feature tracking for Landsat are used to calculate ice velocity. To enhance the surface features in the Landsat images, we use a 3x3 Sobel filter [*Dehecq et al.*, 2015]. Cross-correlation is performed on image patches that are 350m x 350m in size on a regular grid with a spacing of 100m for both SAR and optical

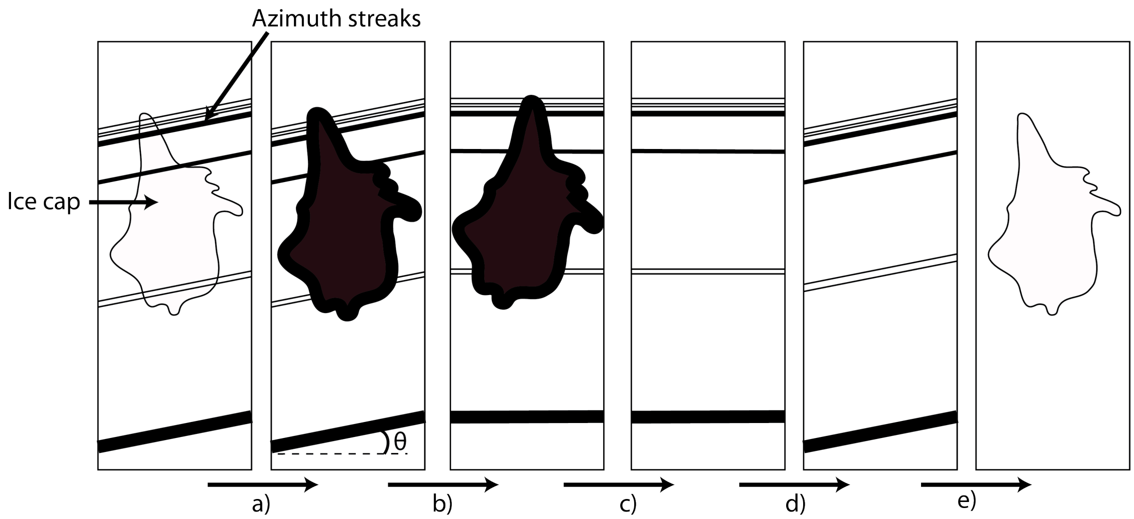

Figure 2.1: *Top panel: Schematic view of the processing steps for ionospheric perturbation reduction of offsets obtained using a speckle tracking technique. 1) Mask glaciers from azimuth offset map, 2) calculation of mean angle of streaks, followed by image rotation, 3) formation of streak model, 4) backward rotation of the streak model, and 5) streak model removed from the original offset map.*

images [*Mouginot et al.*, 2012].

We detect azimuth offsets in the SAR data caused by ionosphere perturbation [*Gray and Mattar*, 2000]. To remove these offsets we mask out the glacier areas and exploit the strong directionality of the streaks to form a "streak model" (Figure 2.1), which is calculated using a linear fit for each line of the azimuth offset map. This model is then removed from the data in the azimuth direction (see Figure 2.2 for example).

The global range and azimuth image offsets are calibrated using areas of presumed zero velocity (mountain outcrops, ice divides). We calculate a quadratic baseline to fit the data in the least square sense [*Mouginot et al.*, 2012]. We mask out sea-ice areas using the SAR amplitude and Landsat images of the same time period. For rectification and geocoding, we employ the 1:250,000 version of the Canadian Digital Elevation Dataset (CDED), Level 1. Tracks are geocoded onto a polar stereographic grid with a central meridian at 45^oW and a secant plane at 70^o N at 100-m spacing. Velocity profiles are extracted along center lines of

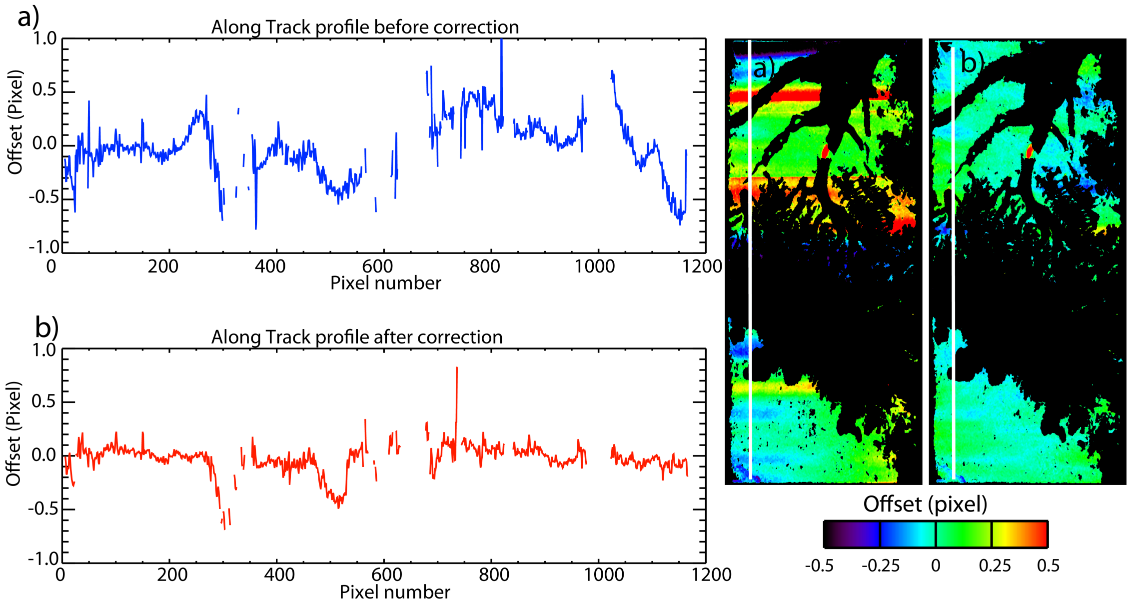

Figure 2.2: *Correction on the azimuth component of an offset map obtained over Iceberg glacier, Axel Heiberg Island. a) Offset (pixels) along A-A' profile shown in c), before correction. b) Offset (pixels) along B-B' profile shown in d), after correction. c) Azimuth component of the offset map before correction. d) Azimuth component of the offset map after correction.*

all major tidewater glaciers to assess changes in ice dynamics since 1991 (see Supplementary Online Material (SOM)). We assemble yearly mosaic of ice velocity (Figure A.2) centered on winter and used later for ice discharge calculation (for example year 1991 corresponds to velocity from July 1991 to July 1992).

We estimate the error in ice speed by calculating the standard deviation of the signal in ice-free areas where ice motion should be zero. The RGI version 3.2 is used to delineate ice field and glacier boundaries [*Pfeffer et al.*, 2014]. Errors are sensor dependent and vary from 3.6 m/yr for ALOS/PALSAR, 7.6 m/yr for RADARSAT-1, 20 m/yr for ERS1, 21 m/yr for Landsat-7 to 25 m/yr for Landsat-8 and 9 m/yr for Sentinel-1a . ERS1, RADARSAT-1 and Sentinel 1-a SAR data have larger errors due to lower image resolution and the stronger ionospheric perturbations.

Where ice thickness is available from OIB data along a glacier cross-section (e.g. Devon Ice

Figure 2.3: *Flow speed of the QEI glaciers averaged between 1991 and 2015, color coded on a logarithmic scale, and overlaid on the CDED DEM in shaded relief. A full map of the QEI with CDED DEM in shaded relief is shown with the position of Nares Strait. Blue basins represent the drainage basins of marine-terminating glaciers and brown basins represent the drainage basins of land-terminating glaciers. Operation IceBridge (OIB) flight tracks are yellow, center flow lines are dash white, flux gates are yellow, and Randolph Glacier Inventory basin boundaries are black. Insets in a), d) and e) show ice front positions of marine-terminating glaciers color coded from black, to blue and white from 1970 to 2015 for a) Otto Glacier, d) Trinity and Wykeham glaciers, and e) Belcher Glacier. Glacier names are provided for major outlet glaciers. Red circles denote glacier acceleration. White circles denote no change in speed. Blue circles denote a slow down in speed during the period 1992 to 2016. Surging glaciers during the 1992-2016 time period are denoted with a black triangle.*

Cap, Prince of Wales Icefield, Mittie glacier), we combine surface velocity with ice thickness to calculate ice discharge, D. The ice thickness was collected between 2012 and 2014 and has a nominal error of 20 m [*P. Gogineni*, 2012]. We calculate D as the mass flux passing through a flux gate close to the terminus of the glacier, converted into water equivalent using an ice density of 917 kg m^{-3}. We combine the errors in velocity and thickness using the root of the sum of square to calculate the error in D. For glaciers with no thickness cross-section (ie 44%), we use OIB ice thickness at the centerline and interpolate across the glacier assuming a U shape-valley as in [*Van Wychen et al.*, 2014]. In this case, the error in ice discharge is calculated assuming that ice thickness is affected by a 12% error as in [*Van Wychen et al.*, 2014].

Yearly D is obtained for 1991 through 2015. We fill data gaps using a linear temporal regression in D. These data gaps may include surge events, and so it is possible that we are underestimating the long-term ice discharge from the region. In total, we survey 80% of the marine terminating glaciers. When there is not enough data to calculate this regression, we extrapolate D using the closest non-surging value in time. We use the area of non-surveyed glaciers to calculate their ice discharge by scaling the median of the total D between 1991 and 2015 for each ice caps individually. We assume a conservative error of 100% for the scaled discharge. Table A.1 summarizes the ice discharge for each glacier, the method employed,

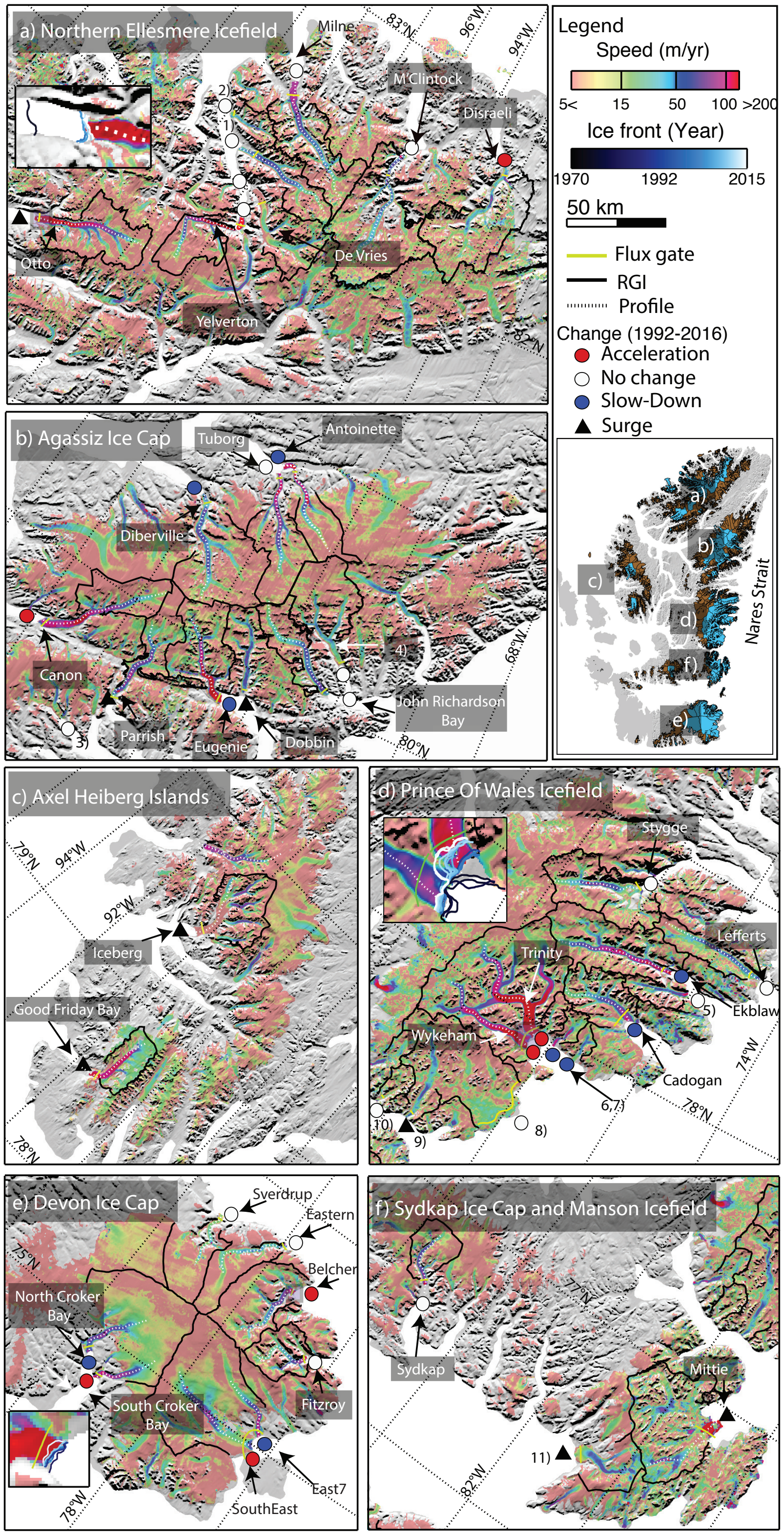

Figure 2.3: *Caption on previous page.*

and the ice area of land-terminating and marine-terminating glaciers.

Additionally, we used Landsat images between 1970 and 2016 and amplitude images between 1991 and 2016 to determine the ice front position for Otto, Trinity, Wykeham and Belcher glaciers. The ice front was digitized manually using the Quantum GIS software.

2.2.2 Surface Mass Balance

We used the Regional Atmospheric Climate Model version 2.3 at 11 km spatial resolution [*Ettema et al.*, 2009] to quantify SMB over the past 25 years. Because RACMO overestimates ice areas under 1,000 m a.s.l [*Lenaerts et al.*, 2013], we use an hypsometry correction from a high-resolution DEM to correct SMB, runoff and precipitation. This DEM was obtain from the combination of 149 individual CDED DEMs derived from 1:60,000 aerial photographs acquired during the period 1950-1960 [*Gardner et al.*, 2011]. The average value of SMB, runoff and precipitation for each DEM class is multiplied by the area at the corresponding elevation interval. The total SMB is then obtained by adding all the different classes together. The change in SMB due to the hypsometry correction averages 25% between 1958 and 2014. The uncertainty in SMB is calculated to be 30% in the QEI, with 10% from precipitation and 28% from runoff as it was determined by [*Lenaerts et al.*, 2013]. The average SMB for the period 1960-1990 is 1.2±0.4 Gt/yr and the rate of mass loss for the period 2005-2011 is 32±9 Gt/yr, which is consistent with [*Lenaerts et al.*, 2013]. The total mass balance is calculated as the difference between SMB and D for individual glaciers and summed up over the entire icefields.

2.3 Results

The velocity maps clearly separate marine-terminating glaciers where ice speed increases continuously up to the ice front, from land-terminating glaciers where ice speed is maximal near the equilibrium line elevation and then decreases to zero at the ice front (Figure B.3). The mapping extends from the ice divides to the ice fronts, i.e. covers the entire ice masses. We observe significant fluctuations in glacier speed over time.

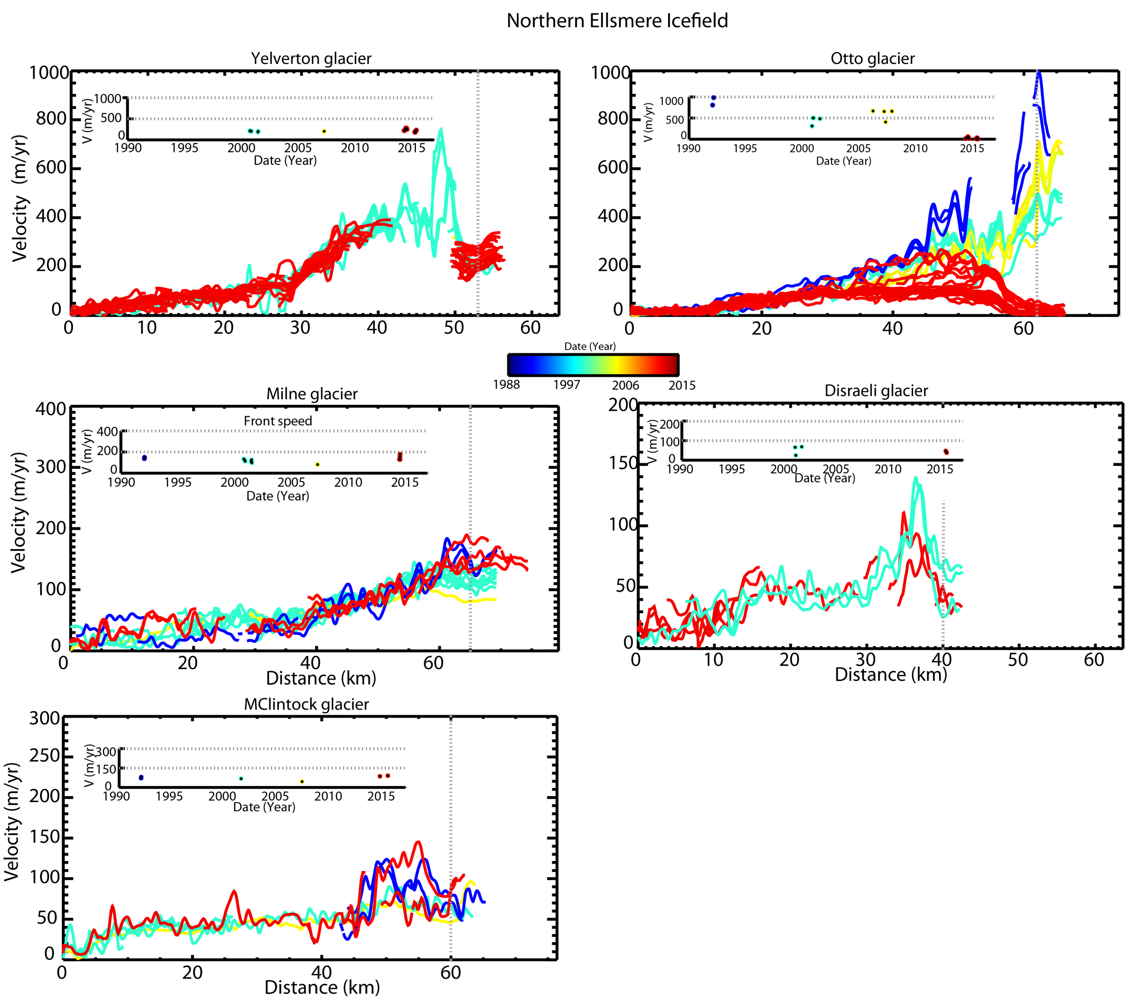

Figure 2.4: *Velocity along flowlines for Northern Ellesmere Icefield. Profile positions and glacier names are shown in Figure B.3. Insets display the speed versus time at the vertical grey dashed on the main plot. Speed is color coded from 1988 (blue) to 2015 (red).*

The Northern Ellesmere Icefield (NEI) includes large-size marine-terminating glaciers on its western and northern flanks (Otto, Milne, Yelverton, M'Clintock and Disraeli) and land-terminating glaciers along its southern and eastern flanks that represent more than 60% of the ice area (16,871 km^2, Figure B.3a and Table A.1). The ice discharge from NEI averaged 0.48±0.08 Gt/yr between 1991 and 2000 (Table A.1). The discharge increased after 2001 to peak at 0.53±0.12 Gt/yr in 2006 during the surge of Otto Glacier (Table A.1 and Figure 2.4). Ice discharge then dropped to 0.31±0.1 Gt/yr in 2015 due to a decrease in speed of most glaciers. Otto Glacier experienced a significant slow down between 1991 and 2015 with a frontal speed dropping from $>$ 800 m/yr in 1991 to $<$ 50 m/yr in 2013-2015 (Figure 2.4). After 2010, more than half of the ice discharge of NEI was driven by Yelverton and Milne glaciers with an average total of 0.15±0.06 Gt/yr between 1991 and 2015 (Table A.1).

The Agassiz Ice Cap, between the POW and NEI, comprises a large number of marine-terminating glaciers that represents 8,844 km^2 (40% of the ice area, Figure B.3b and Table A.1). The ice discharge was nearly constant between 1991 and 2000 with an average of 0.28±0.05 Gt/yr. An average mass flux of 0.5±0.04 Gt/yr is calculated between 2005 and 2007 due to the combined surge of Parrish Glacier and Glacier 5 (Figure 2.5 and Table A.1). The mass flux of 60% of the glaciers decreased during 2010-2015 compared to 1991-2010 (Figure 2.10, Figure 2.5, Table A.1). Cañon, Glacier 4, Dobbin and Tuborg Glaciers are the only ones that maintain a steady state regime during 2000-2015.

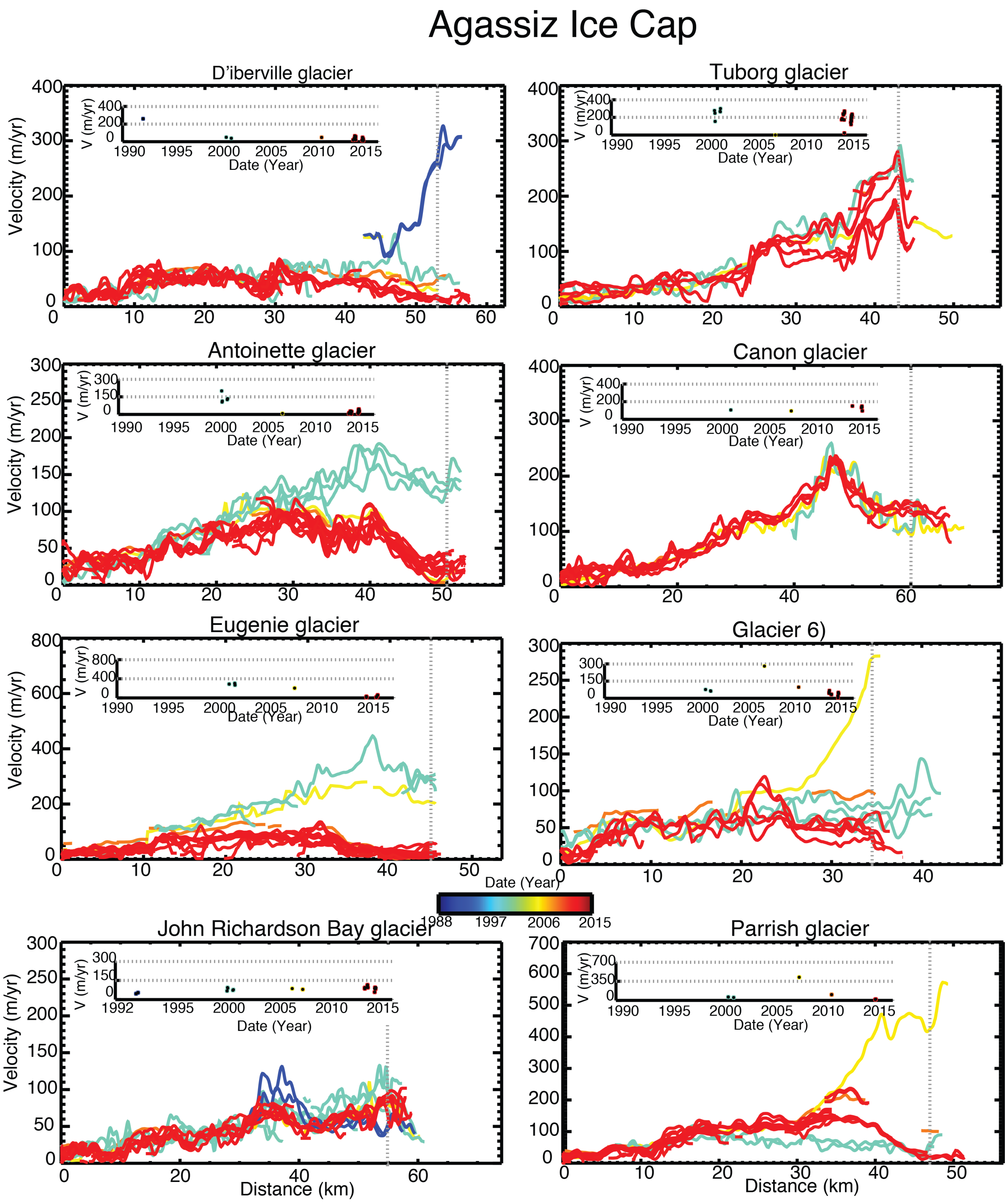

Figure 2.5: *Velocity along flowlines on Agassiz Ice Cap. Profile locations and glacier names are shown in Figure B.3. Insets display the speed versus time at the vertical grey dashed line on the main plot. Velocity is color coded from 1988 (blue) to 2015 (red).*

The POW is located in the central part of Ellesmere Island between 76^{o}N and 78^{o}N (Figure B.3d). The western part only includes land-terminating glaciers whereas the eastern part is drained by large marine-terminating glaciers that drain $> 60\%$ of the total area (Table A.1). The ice discharge of POW averaged 1.6±0.1 Gt/yr between 1991 and 2008 and increased by a factor of 1.5 since then. During the time period 2009-2015, D increased to 2.46±0.4 Gt/yr (Figure 2.10 and Table A.1). 83% of the glaciers slowed down or maintain a steady regime, however, so the increase in D was only due to the acceleration of two glaciers: Trinity and Wykeham (Figure 2.9, Figure 2.10 and Table A.1). Draining from a common basin, these glaciers flow several times faster than any other glacier in the QEI (Figure B.3). Their ice speed (Figure 2.9) was stable in 1991-2009, accelerated by a factor of two to 1,200 m/yr for Trinity and 650 m/yr for Wykeham in 2015. Examination of the position of the ice fronts reveals a continuous retreat of Trinity Glacier since 1991 by 5 km (Figure 2.9). The retreat amounts to 7.7 km since 1976 (Figure B.3d). Wykeham Glacier retreated 1.8 km between 1991 and 2015 and 4.2 km between 1976 and 2015. At present, the northern part of Wykeham ice front is no longer retreating (Figure 2.9).

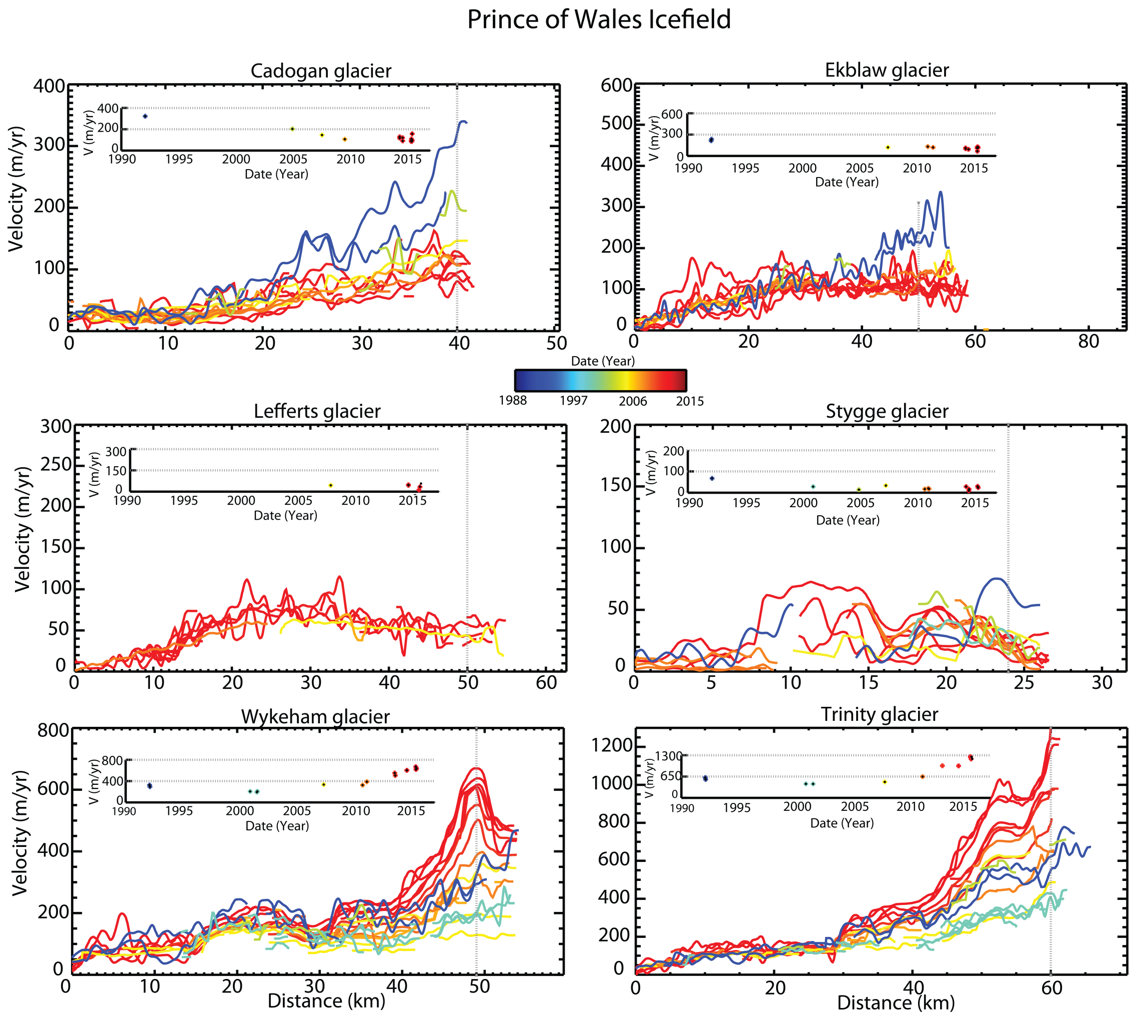

Figure 2.6: *Velocity along flowlines on Prince of Wales Icefield. Profile locations and glacier names are shown in Figure B.3. Insets display the speed versus time at the vertical grey dashed on the main plot. Speed is color coded from 1988 (blue) to 2015 (red).*

South of POW, on Sydkap Ice Cap and Manson Icefield (Figure B.3f), Sydkap Glacier ice discharge dropped from 0.04±0.001 Gt/yr in 1991 to 0.02±0.002 Gt/yr in 2010 and slightly increased to 0.05±0.001 Gt/yr in 2015 (Table A.1). In contrast, we calculate a mass flux in 2000 of 0.9±0.01 Gt/yr for Mittie Glacier, followed by a decrease to an average 0.02±0.002 Gt/yr for 2003-2015. Similar abrupt changes in ice discharge are detected for Iceberg and Good Friday Bay glaciers on Axel Heiberg Islands in 1991 (Figure B.3c and 2.7).

Others

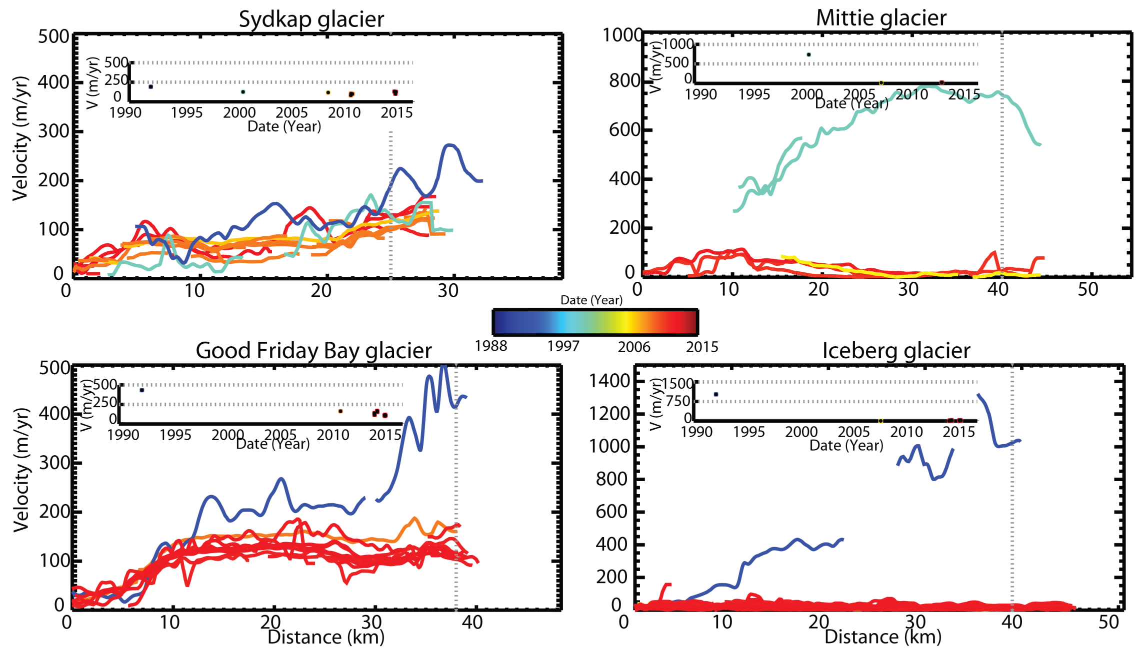

Figure 2.7: *Velocity along flowlines for remaining glaciers. Profile positions and glacier names are shown in Figure B.3. Insets display the speed measured at the vertical grey dashed on the main plot. Speed is color coded from 1988 (blue) to 2015 (red).*

Finally, the DIC is characterized by a dominance of marine-terminating glaciers (10,275 km^2 vs 4,722 km^2 for land-terminating glaciers) (Figure B.3e, 2). The discharge of the entire ice cap increased from 0.46±0.1 Gt/yr to 0.53±0.1 Gt/yr between 1991 and 2015. However the increase in D is within the uncertainty, so we cannot draw solid conclusions on the evolution of this sector. Belcher, South Croker Bay and Fitzroy are the fastest moving glaciers, with speeds of 300 m/yr at their calving fronts. Most glaciers have maintained a steady flow regime since 1991 and the increase in ice discharge is mainly due to the 50% acceleration of Belcher during this period (Table A.1, Figure 2.8). North Croker Bay displays a significant slow down to zero frontal speed in 2015, which suggests that the glacier may have detached from the ocean or have become analogous to a land terminating glacier.

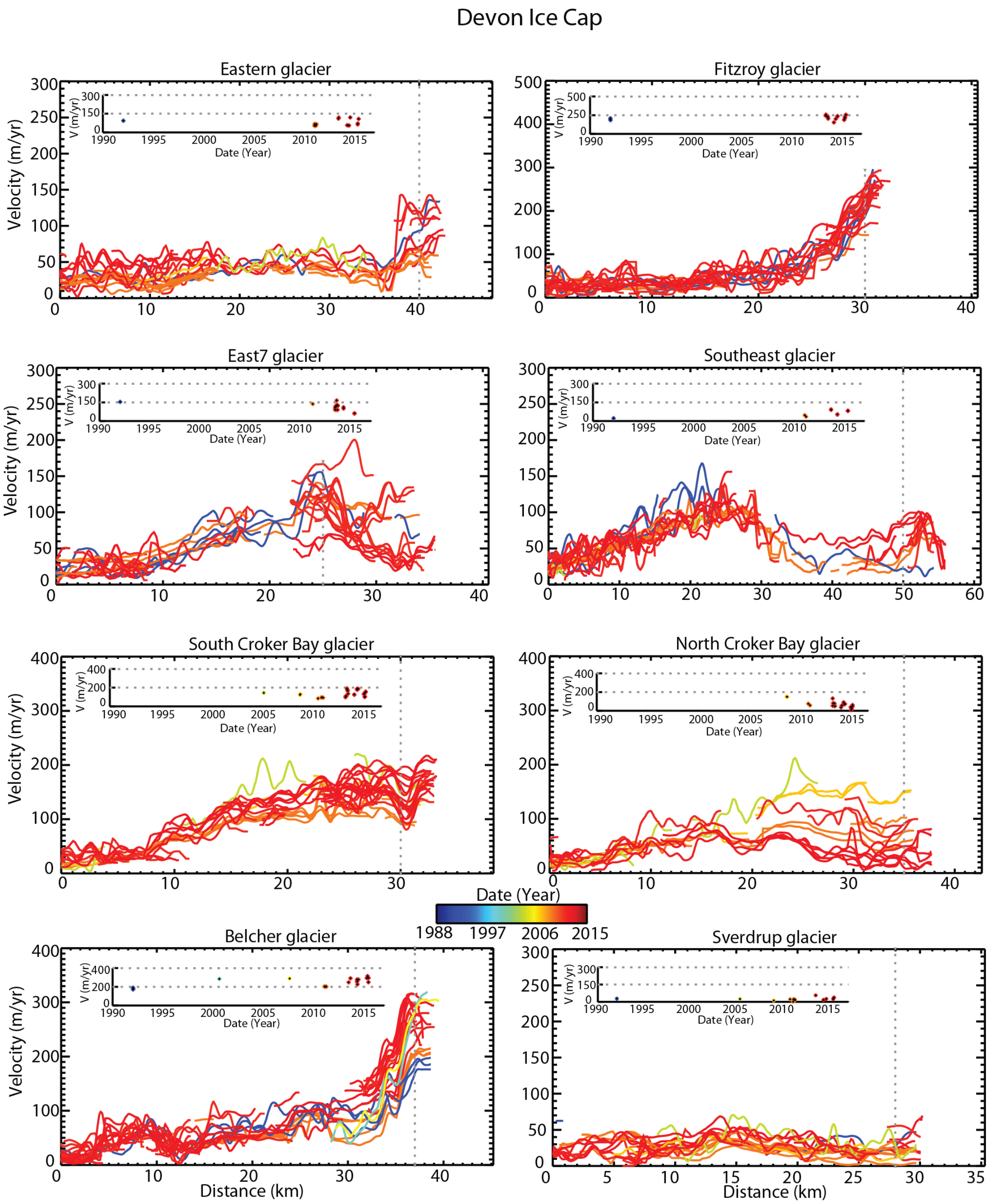

Figure 2.8: *Velocity along flowlines for Devon Ice Cap. Profile positions and glacier names are shown Figure B.3. The insets display the speed measure at the vertical grey dashed on the main plot. Speed is color coded from 1988 (blue) to 2015 (red).*

Overall, more than 60% of the ice discharge was measured for 9 years (outside interpolations and extrapolations) compared to the 5 years of recent studies [*Van Wychen et al.*, 2016], with crucial new data between 2004 and 2010. Importantly, our discharge results extend these studies further back in time from 2000-2015 to measurements between 1991 and 2016, which is important to draw conclusions about long term changes in ice dynamics. Differences in total surveyed ice discharge for common years results from the addition of Devon Ice Cap in our study, which is the second highest contributor to the total ice discharge and from differences in survey area. We estimate that Devon Ice Cap contributes an average 0.46±0.01 Gt/yr discharge over 1991-2015, in agreement with [*Van Wychen et al.*, 2012] for year 2009. The total ice discharge is on average 1.4±0.5 Gt/yr higher than in [*Van Wychen et al.*, 2016] for complete years (i.e. 2000, 2011, 2013, 2014 and 2015).

2.4 Discussion

The difference between surge and pulse type glaciers is defined by the velocity structure, and particularly in the region of initiation and propagation [*Van Wychen et al.*, 2016]. As the definition of pulse-type glacier vary from study to study (e.g [*Mayol*, 1978; *Raymond*, 1987; *Turrin et al.*, 2014; *Van Wychen et al.*, 2016]) and because the difference between these two behaviors is not crucial in the calculation of the mass balance, surge and pulse type glaciers are both referenced as "surge type" glaciers hereafter.

Among the 30 major glaciers surveyed in this study, 60% did not change speed or even slowed down. We detect 6 major surging glaciers : Mittie, Parrish, Dobbin, Good Friday Bay, Middle and Iceberg glaciers that were also documented in [*Copland et al.*, 2003] and [*Van Wychen et al.*, 2016]. However, we report here new informations on the important increase in speed of d'Iberville, Glacier 9 and Glacier 11. The 300 m/yr speed of d'Iberville glacier in 1991 was three times higher than for the period 2000-2015. In 2007, Glacier 11 quadrupled its ice discharge from 0.01±0.01 Gt/yr to 0.04±0.01 Gt/yr. Similarly, Glacier 9 increased its ice discharge to 0.2±0.06 Gt/yr in 2006, which is 8 times higher than in 2000 and for the period 2010-2015. Evidence of surge features such as loop moraines, intensive crevassing or dramatic terminus position are lacking at this time for d'Iberville glacier in 1992. No such features were found on Glacier 11 and Glacier 9. Analysis of the thinning pattern would be necessary to draw conclusions on the changes in dynamics of these glaciers and to determine if it can be attributed to surge episodes. In total, however, the ice discharge from all these glaciers remains low, even after accounting for the surges and short term peak in D. The average D for D'Iberville, Dobbin, Parrish, Otto, Good Friday Bay, Iceberg, Mittie, Glacier 11 and Glacier 9 are, respectively, 0.02, 0.04, 0.04 , 0.1, 0.1, 0.04, 0.1, 0.01 and 0.07 Gt/yr (average of errors across all surging glaciers is below 0.005 Gt/yr). As a result of the surges that took place during the period 1991-2015, we estimate that D increased by 0.2 Gt/yr or 6%. The effect of surges and peak in ice discharge on the decadal mass balance of the glaciers is therefore small.

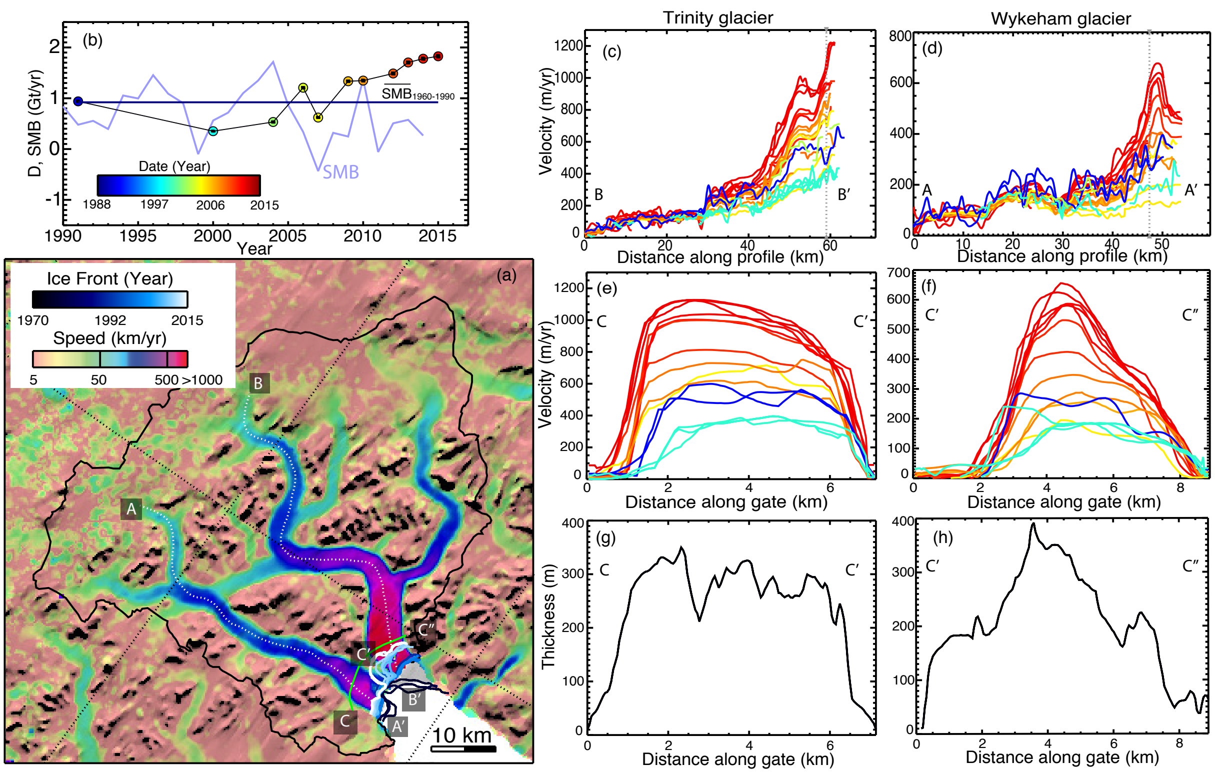

Figure 2.9: *Ice dynamics of Trinity and Wykeham glaciers: a) Ice velocity on a logarithmic color scale with Operation IceBridge (OIB) flux gate in green, Randolph Glacier Inventory basin outline in black, center flow line profiles in dotted white, and ice front positions from 1970 to 2015 color coded on a linear scale from black, to blue, and white; b) ice discharge of Trinity and Wykeham glaciers colored by year from blue to green and red, with SMB (not corrected from hypsometry) in blue and reference SMB for the years 1960-1990 as an horizontal blue line. Speed changes between 1991 and 2015 along c) and d) center flow lines A-A' and B-B' and e, f) across the flux gates C-C' and C'-C" with g, h) corresponding OIB ice thickness. Flow speed in c-f are also coded from blue, to green and red for the years 1992 to 2015.*

In total for QEI, we find that D decreased from 4.5±0.5 Gt/yr in 1991 to 3.5±0.5 Gt/yr in 2000 due to a decrease in flow speed of several glaciers (Figure 2.10 and Table A.1). Between 2000 and 2015, D remained constant because the slow down of most glaciers was compensated by the speed up of Trinity and Wykeham glaciers. At the local scale, however, D is a significant component of the mass balance for Trinity and Wykeham glaciers. Both glaciers experienced the largest increase in ice speed of the entire archipelago. Analysis of the SMB record (Figure 2.9) reveals that these glaciers were in balance between 1991 and

2008 with an ice discharge of 0.6±0.02 Gt/yr (Figure 2.9) versus a SMB of 0.83±0.2 Gt/yr. After 2008, the mass balance decreased from +0.25±0.1 Gt/yr (i.e. a mass gain) to -1.0±0.2 Gt/yr. This increase in mass loss is due to a doubling in runoff production from 0.43±0.02 Gt/yr to 0.83±0.1 Gt/yr and a doubling in ice discharge from 0.6±0.02 Gt/yr to 1.5±0.1 Gt/yr after 2009. The increase in glacier speed tripled the mass loss caused by enhanced runoff alone. In total, these two glaciers contributed a 37% increase in total discharge from QEI since 2010 (Figure 2.10). Yet, this is the only sector in QEI where changes in speed have had a significant impact on total mass balance.

During the time period 1991-2005, the QEI was losing mass at a rate of 6.3±1.1 Gt/yr (Figure 2.10). Ice discharge contributed 52% of the losses (3.4±0.1 Gt/yr discharge vs 3.0±1.1 Gt/yr from SMB). After 2005, the mass budget became strongly negative due to a significant increase in runoff that reduced SMB to -55.6±16.6 Gt/yr in 2012 (Figure 2.10b). During that time period, there was no trend in precipitation, which averaged 28±2.9 Gt/yr (Figure 2.10b). The loss due to ice discharge of 3.5±0.2 Gt/yr therefore contributed only 10% of the total loss, i.e. the loss was dominated by enhanced runoff. This is consistent with previous studies over shorter time periods [*Gardner et al.*, 2011].

The transition in mass balance coincides with a marked increase in summer air temperature around year 2004 that has continued until present [*Gardner et al.*, 2011]. In the period 2013-2014, runoff production decreased and SMB increased from -55.6±16.6 Gt/yr to +8.2±2.5 Gt/yr. This pause in mass loss resulted from colder-than-average consecutive summers following the large melt event of 2012 [*Tedesco et al.*, 2015]. Over the entire time period 1991-2015, the mass loss averaged 16.0±1.7 Gt/yr, with an acceleration of 1.0±0.1 Gt/yr^2. Interestingly, we can notice that mass balance estimates vary significantly with respect to the methods. Indeed, calculation from straight altimetry or gravimetry shows values of 27±7 Gt/yr and 24±6 Gt/yr for 2003-2010 [*Nilsson et al.*, 2015; *Colgan et al.*, 2015]. This number are much lower than the 34±13 Gt/yr from [*Gardner et al.*, 2011] for 2004-2009 that are closer from the 35±18 Gt/yr during 2005-2011 [*Lenaerts et al.*, 2013] and the 33.0±3.0 Gt/yr during 2005-2015 from this study. Thus, it seems that the uses of an input-output method, with a surface mass balance model gives larger estimates than a mass balance derived only from altimetry or gravity.

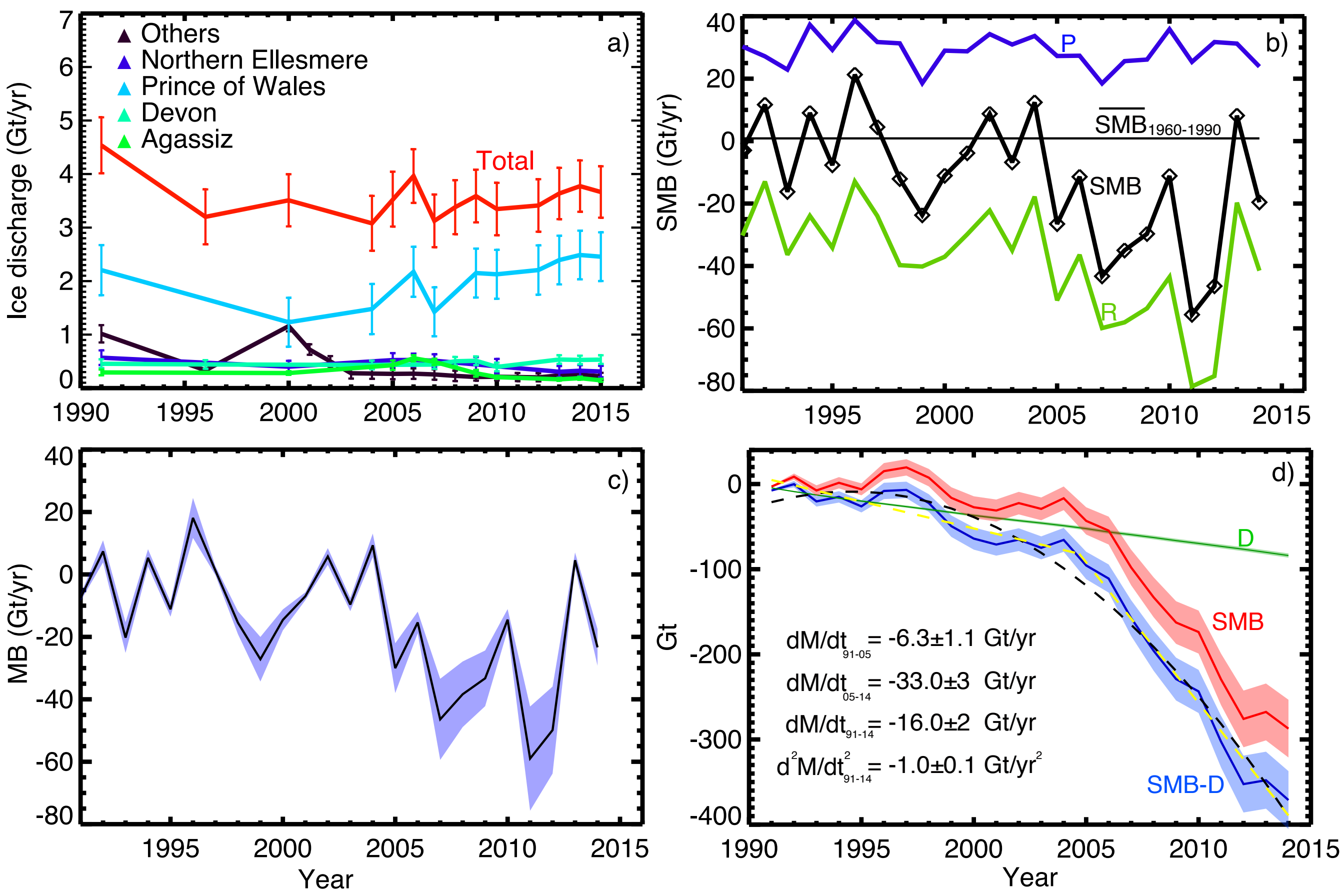

Figure 2.10: *Mass budget of the Queen Elizabeth Islands (QEI), Canada from 1991 to 2015: a) ice discharge for several icefields and for the entire survey domain. "Others" includes Sydkap, Mittie and Axel Heiberg icecaps. Error bars are only shown for years with measurements. b) total surface mass balance (SMB), runoff (R), precipitation (P), and reference SMB for the years 1960-1990 for the entire survey domain, c) total mass balance (MB=SMB-D); d) cumulative surface mass balance, ice discharge, and total mass balance for the entire survey domain. Mass balance trends for 1991-2005, 2005-2015 (yellow dashed line) and quadratic fit for 1991-2015 (black dashed line) are shown in d).*

To understand the evolution of marine-terminating glaciers in POW, it is essential to investigate their interaction with the surrounding ocean because the intrusion of warm ocean waters have the potential to melt ice in contact with it, undercutting the ice fronts and increasing iceberg calving [*Motyka et al.*, 2003; *O'Leary and Christoffersen*, 2013; *Bartholomaus et al.*, 2013]. Ocean currents along POW are driven by the inflow from Nares Strait (see Figure B.3 for location). [*Mnchow et al.*, 2011] report an increase in ocean temperature in Nares Strait after year 2007 which would suggests that ice melting by the ocean must have increased significantly around that time. Enhanced melting of the calving margins may have dislodged the glaciers from their stabilizing positions after 2010, when Trinity and Wykeham start to accelerate and increase their ice discharge significantly (Table A.1, Figure 2.9). From these observations, we suggest that ice melting by the ocean must have started to increase prior to 2010. Details on the bathymetry, glacier bed topography, and ocean temperature in front of the glaciers are, however, lacking at this time to make any firm conclusions about the changes in this sector.

We find that 9 glaciers reduced their frontal speed to zero during the time period (Figure 2.4 to 2.8), suggesting that they lost contact with the ocean, hence stopped calving, as they retreated to higher ground. Alternatively, these glaciers are surge type glaciers that transitioned to a quiescent phase. An analysis of Landsat-8 2015 images indicate that the glaciers were still all in contact with the ocean because we find no moraine deposit separating the ice front from seawater (Figure A.3). Hence, these glaciers remain marine terminating. We note, however, that most of them are rather thin at the ice front, and less than 100 m thick (Figure 2.11). At this level of ice thickness, the driving stress is quite low, i.e. ice may not deform internally [*Hutter*, 1982]. Hence, these glaciers, while reaching the ocean, are more similar to land-terminating glaciers than to tidewater glaciers.

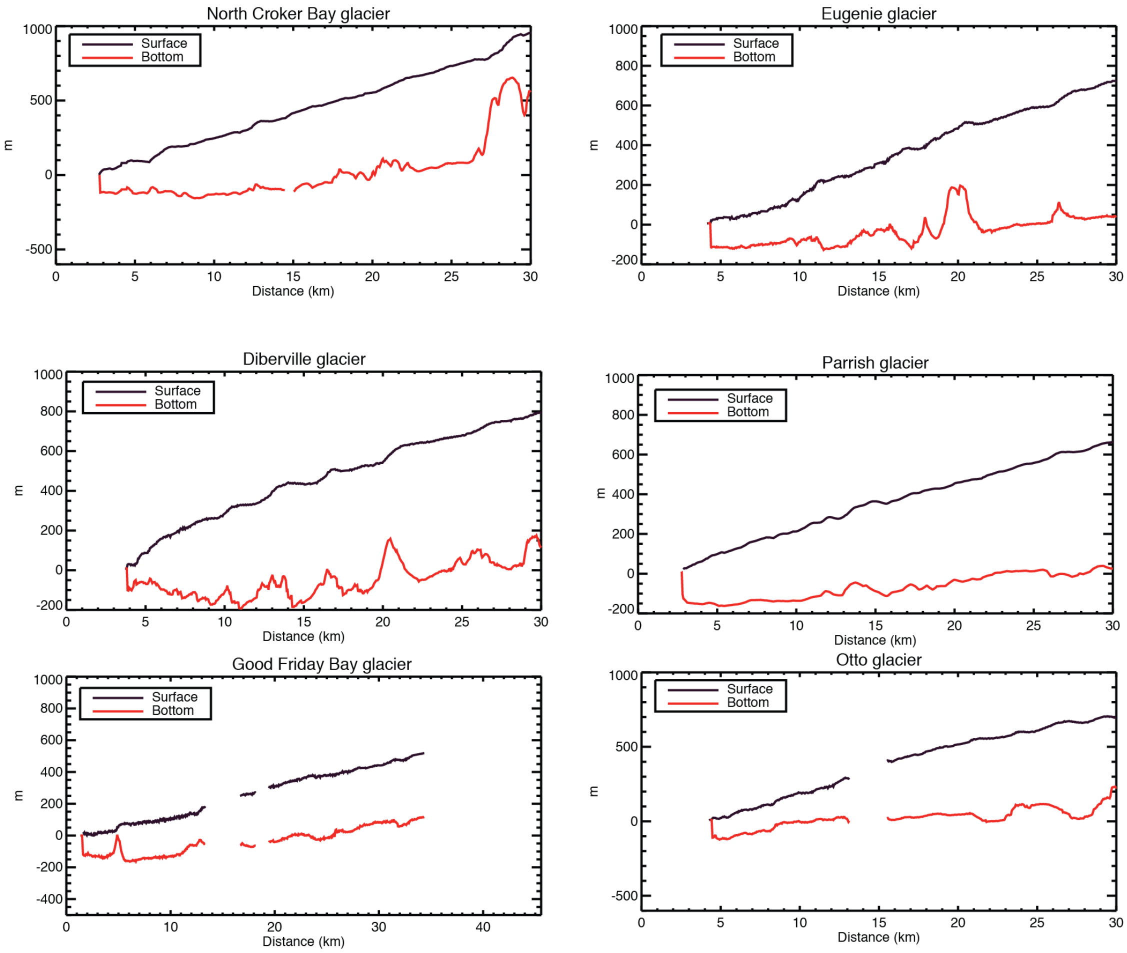

Figure 2.11: *Ice bottom and ice surface elevation of stagnant and near-stagnant glaciers derived from NASA Operation IceBridge (OIB) data acquired in year 2014.*

The mass loss of the QEI averaged over its 105,000-km^2 area is 0.17±0.05 m/yr water-equivalent (w.e) for the time period 1991-2014 (0.06±0.02 m/yr for 1991-2005 and 0.34±0.03 m/yr for 2005-2014). For comparison, Alaskan glaciers experienced a mass loss of 75±11 Gt/yr for the time period 1994-2013 [*Larsen et al.*, 2015], i.e. an average loss of 0.7±0.1 m/yr w.e over their 85,000-km^2 area, or 4 times larger. Conversely, the mass loss of the Patagonia Icefields averaged 24.4±1.4 Gt/yr between 2000 and 2012 [*Willis et al.*, 2012], which corresponds to an average mass loss of 1.3±0.1 m/yr w.e over their area of 21,000 km^2, or 7.6 times larger than for the QEI. Hence, the average mass loss per unit area decreases markedly from low latitudes (Patagonia) to high latitudes (QEI). The QEI currently contributes less mass loss than Patagonia because of its larger area, but we posit that a change in global mean surface air temperature of 0.3-0.5 °C for the period 2016-2035 as projected by the IPCC report [*Church et al.*, 2011] could potentially increase the mass loss of the QEI to reach the values observed in Patagonia, which is one order magnitude larger per unit area.

2.5 Conclusions.

We present the largest time series of glacier velocity and mass balance for the Queen Elizabeth Islands, in Canada spanning from 1991 to 2015 with a complete velocity mapping at 100-m spacing. The acceleration of Trinity and Wykeham between 2010-2015 increased the ice discharge by 37% and accounted for 50% of the total ice discharge from the QEI to the ocean in 2015. Yet, even if ice discharge can play an important role at the basin scale, its contribution to the total mass loss from these icefields remains small. Similarly, glacier surges do not have a significant impact on the long-term mass balance of the QEI. The vast majority of the mass loss is controlled by SMB processes, mainly runoff. Prior to 2005, the rate of mass loss was low and controlled by ice discharge. After 2005, the mass loss increased markedly to transform the QEI into a major contributor to sea level change. With ongoing, sustained, rapid warming of the high Arctic, the mass loss of QEI should continue to increase significantly in the coming decades to century.

Chapter 3

Bathymetry of the Amundsen Sea Embayment sector of West Antarctica from Operation IceBridge gravity and other data.

R Millan, E. Rignot, V. Bernier, M. Morlighem, P. Dutrieux

As presented in:

Millan, R., E. Rignot, V. Bernier, M. Morlighem, and P. Dutrieux (2017), Bathymetry of the Amundsen Sea Embayment sector of West Antarctica from Operation IceBridge gravity and other data, *Geophysical Reseach Letters*, 44, 1360-1368, doi:10.1002/2016GL072071.

Abstract

We employ airborne gravity data from NASA's Operation IceBridge collected in 2009-2014 to infer the bathymetry of sub-ice-shelf cavities in front of Pine Island, Thwaites, Smith and Kohler glaciers, West Antarctica. We use a three-dimensional inversion constrained by multi-beam echo sounding data off shore and bed topography from a mass conservation reconstruction on land. The seamless bed elevation data refine details of the Pine Island sub-ice-shelf cavity, a slightly thinner cavity beneath Thwaites, and previously unknown deep (>1,200 m) channels beneath the Crosson and Dotson ice shelves that shallow (500 m and 750 m, respectively) near the ice shelf fronts. These sub-ice-shelf channels define the natural pathways for warm, circumpolar deep water to reach the glacier grounding lines, melt the ice shelves from below, and constrain the pattern of past and future glacial retreat.

3.1 Introduction

The Amundsen Sea Embayment (ASE) in West Antarctica (WAIS) is a major contributor to present-day sea level rise from Antarctica and holds an ice volume equivalent to 1.2-m global sea level rise [e.g., [*Rignot*, 2008]]. The major glaciers in the ASE include the Pine Island, Thwaites, Haynes, Smith, Pope, and Kohler glaciers. These glaciers are retreating along deep troughs with a bed elevation that decreases inland, a factor long recognized to promote rapid, irreversible retreat [e.g. [*Hughes*, 1981]]. Several studies have suggested that this sector of WAIS may already be in a state of collapse [*Parizek et al.*, 2013; *Favier et al.*, 2014]; [*Rignot et al.*, 2014]. A number of airborne radar surveys were conducted to measure ice thickness and bed topography on land [*Thomas*, 2004]; [*Holt et al.*, 2006; *Vaughan et al.*, 2006; *Leuschen et al.*, 2010]. [*Fretwell et al.*, 2013] combined these data with year 2008 GEBCO bathymetry data to produce the bed topography BEDMAP-2 which includes the sea floor depth. A considerable amount of bathymetric data, including multibeam echo sounding (MBES) data, was subsequently assembled as part of IBCSO [*Arndt et al.*, 2013; *Nitsche et al.*, 2007], but data coverage did not extend into the sub-ice-shelf cavities. As a result, bed mapping between the glacier grounding lines and the ice shelf fronts has been affected by large uncertainties. For example, the BEDMAP-2 and IBCSO bathymetries beneath Crosson and Dotson ice shelves assume zero water column, i.e. the sea floor depth coincides with the ice shelf draft. Such gap in our knowledge makes it difficult to study ice-ocean interactions beneath these ice shelves. Data from neighboring regions [e.g. [*Jenkins et al.*, 2010]] show that deep channels carved on the sea floor by past advances of the glaciers exist beneath all these ice shelves. These bed troughs act as natural pathways for subsurface, warm, salty, Circumpolar Deep Water (CDW) to reach the glacier grounding lines [*Jacobs et al.*, 2011]. Warm CDW induces high rates of ice shelf melt [*Rignot et al.*, 2013] that exert an important control on glacier flow and stability. Conversely, sills in the seafloor or stranded icebergs may partially block the access of CDW to the glaciers [*Jacobs et al.*, 2012].

Resolving the bathymetry beneath the ice shelves is therefore a fundamental prerequisite to investigations of ocean circulation near the coastline, its impact on ice-ocean interactions and glacier retreat, and in turn on understanding the past, present and future mass balance of this sector of WAIS.

On land, the results of airborne radar surveys have been combined with high resolution ice flow vectors from satellite radar interferometry using a mass conservation method (MC) [*Morlighem et al.*, 2011] to produce the first high resolution (350-m), gridded map of ice thickness and bed topography upstream of the grounding lines of all ASE glaciers [*Rignot et al.*, 2014]. These products have revealed erroneous bed picking from the radar echoes beneath Pine Island caused by bottom crevasse formation during the rapid glacier retreat that took place in the years of 2004-2009. Fresh bottom crevasses yield strong radar echoes at their apex that are confused with echoes from the ice shelf draft. The corrected data revealed a deeper bed at the grounding line and the absence of major sills in topography upstream that could halt the glacier retreat. Similar conclusions of unstoppable retreat were reached for Thwaites, Haynes, Pope, Smith and Kohler glaciers, but the shape of the sub-ice-shelf cavities in front of these glaciers remains poorly sampled. This is important to resolve because the shape of the cavities determines how ocean heat reaches the glacier grounding lines, which in turn determines whether the retreat will be rapid (warm water access, high melt) versus slow (no warm water access, low melt).

Since 2009, NASA Operation IceBridge (OIB) has been collecting airborne gravity data to constrain the bathymetry beneath these ice shelves [*Cochran and Bell*, 2010]. These data have been complemented by in-situ measurements beneath Pine Island Shelf from an Autonomous Underwater Vehicle (AUV) [*Jenkins et al.*, 2010] and from seismic methods [*Muto et al.*, 2016] or M2016. On Pine Island, both datasets revealed the presence of an east-west ridge across the ice shelf path that probably acted as an anchor in the past [*Jenkins et al.*, 2010; *Studinger et al.*, 2010] and modulates the access of CDW to the grounding line

[*Dutrieux et al.*, 2014]. On Thwaites, [*Tinto and Bell*, 2011] applied two-dimensional (2D) inversions on data from year 2009 to reveal a prominent ridge, 15 km wide, with two peaks, 40 km from the present front, that may have pinned down the glacier in the past. No result has been published for Crosson and Dotson ice shelves farther west. More important, none of the gravity data has been analyzed and inverted in a seamless fashion to provide consistent topography across the grounding line, match the MBES/IBCSO data off shore, and the MC bed topography inland. This lack of consistency across the grounding zone significantly affects data quality and limits what can be done with ice sheet and ocean numerical models using these data. In particular, large discontinuities in bed topography across the grounding line are a major impediment to correctly reconstruct ice flow evolution.

Here, we employ a methodology that combines the OIB gravity data from years 2009 to 2014 with high resolution MC bed mapping inland and MBES/IBCSO mapping off shore using a three-dimensional (3D) inversion to obtain a consistent and comprehensive bed topography across the entire ASE domain beneath ice shelves and extending along the glacier grounding lines. In addition, for Pine Island, we use the AUV and seismic data collected on the shelf to constrain the inversion. We estimate the uncertainty of the inversion and discuss the impact of the results on the identification of natural pathways of CDW toward the grounding lines, their impact on the ice shelf melt regimes, and their impact on the past, present and future pattern of glacial retreat.

3.2 Data and Methods

We use OIB gravity measurements acquired between October 2009 and November 2014 by the Sanders Geophysics Airborne Inertially Referenced Gravimeter (AIRGrav). AIRGrav flies a draped survey at about 400 m above ground on average [*Cochran and Bell*, 2010]. The gravimeter measures the Earth's gravity field and accelerations at a sampling frequency of 128 Hz. Anomalies are decimated to 2 Hz. Data are filtered and delivered at a spatial resolution of 4.9 km in this area using a 70 second full wavelength filter at an aircraft speed of 150 m/s. Eotvos, normal gravity, free-air, static and level corrections are applied on the data to yield free-air gravity anomalies, which we refer to as gravity data in the remainder of the paper. An analysis of cross overs indicates a measurement error of 0.5 mGal for the gravity data.

We select 32 OIB tracks with an absolute elevation of less than 1,500 m above mean sea level (msl) (Fig. B.1). All data are upward continued to the maximum plane elevation within the survey domain, i.e. the gravity data collected at various elevations are extrapolated upward to a common elevation which is the highest aircraft elevation within the survey. We divide the survey domain into three blocks for ease of computation: 1) Pine Island, 2) Thwaites, and 3) Kohler and Smith glaciers, with Haynes split between domain 2 and 3 (Figure 3.1). The gravity data are "upward continued" to 1,600 m for Pine Island, 1,700 m for Thwaites and 2,000 m for Kohler/Smith. We employ the Geosoft GM-SYS 3D software which implements [*Parker*, 1973]'s method on a 3D representation of the study area with three horizontal layers: 1) a solid ice layer with a density of 0.917 g/cm^3; 2) a sea water layer with a density of 1.028 g/cm^3; and 3) a rock/sediment substrate layer with a uniform density of 2.88 g/cm^3. Density selection for rock is discussed later on. Ice surface elevation and ice shelf thickness are from BEDMAP-2. Ice shelf thickness does not impact the gravity inversion since the ice shelves are in hydrostatic equilibrium, but it is used to calculate the height of the water column beneath ice shelves.

To complete the gravity observations and obtain gravity values at every point of our polar stereographic grid (71°S secant plane, 1000-m spacing), we employ a 3D forward model of the gravity field based on an initial guess of the bed elevation, ice/water depth, and densities over the entire domain. We apply a 70-second full wavelength filter on the forward model gravity data. The initial bed combines the MC solution inland and IBCSO offshore (Fig.

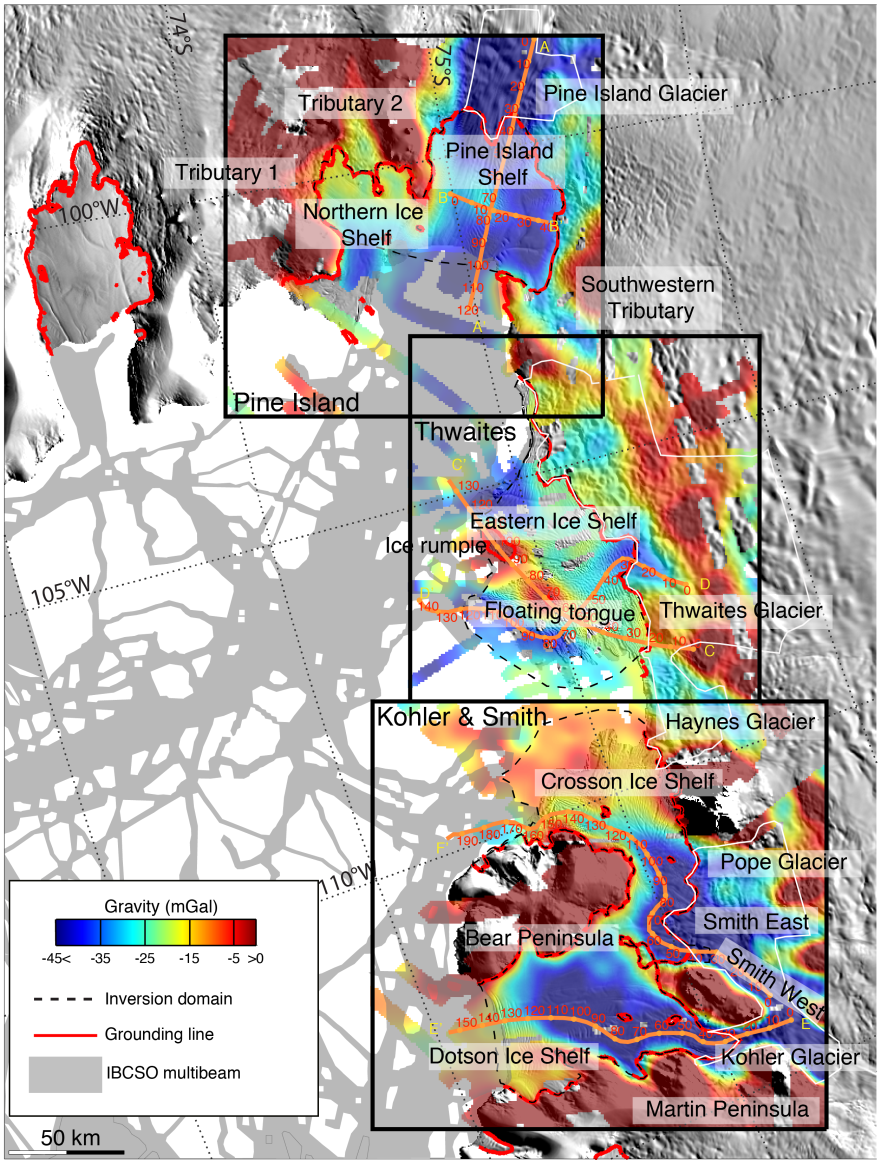

Figure 3.1: *Free-air gravity anomalies in the Amundsen Sea Embayment (ASE) sector of West Antarctica with the Pine Island, Thwaites, Haynes, Pope, Smith and Kohler glaciers overlaid on a MODIS mosaic of Antarctica from year 2004 on a grey scale. Areas mapped with multi beam echo sounding (MBES) are light blue. Glacier grounding lines from year 1996 are red. The limits of the gravity inversions are thin black dash lines within each black box. The limits of the MC inversion are thin white lines.*

B.2). We merge the modeled and observed gravity by matching their mean value over land within a subregion of the MC domain. We allow for a 10-km wide transition boundary between the observed and modeled gravity. The approach of filling data gaps with modeled gravity minimizes edge effects along data gaps on the 3D inversion [*Gourlet et al.*, 2016] and improves the 3D inversion near large gravity anomalies such as mountain blocks.

For Pine Island, we employ an additional procedure with the AUV and seismic data. The initial bed solution combines MC on land, IBCSO on the ocean, and the AUV and seismic data beneath the shelf interpolated linearly with a Delaunay triangulation. We run the forward model to calculate the corresponding gravity field, form the difference between the forward model and the observed gravity, and best fit the result with a minimum curvature surface (Fig. 3.2). The result is a gravity correction that we subtract from the OIB gravity field over the inversion domain. The corrected gravity is then completed with a forward model of the gravity, as described earlier, to fill data gaps with the rectangular domains of the inversion. In the case of Pine Island, the merging of observed and modeled gravity uses the mean gravity anomaly values in front of the glacier where MBES/IBCSO data are available.

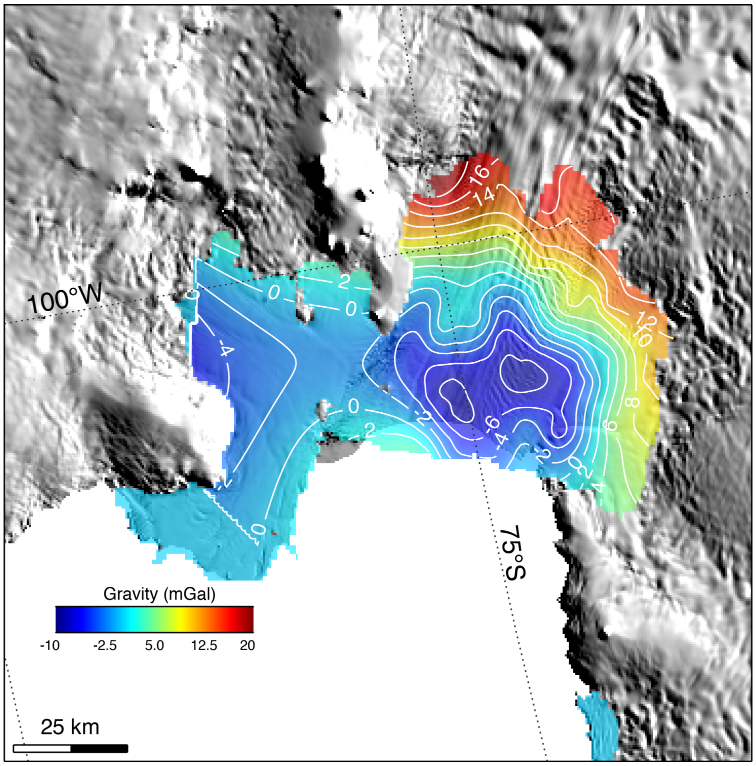

Figure 3.2: *Gravity correction applied to the OIB data in Pine Island Bay to best match the AUV and seismic data, with values varying from -4 mGal to +16 mGal. Contours are every 2 mGal. Background is a MODIS mosaic of Antarctica from year 2004.*

The inversion domain extends from the MC domain to the MBES/IBCSO data or the limits of the gravity survey. We allow a 10-km wide smooth transition at the ocean boundary and at the grounding line. In the transition region, the inversion is modulated by a factor linearly varying between 0 (no gravity inversion) to 1 (full gravity inversion). No data inversion is performed on land (inversion factor is zero). We only invert the gravity data on the ice shelf and portions of the ocean not surveyed by MBES (inversion factor of one). During the inversion, the unknown bed elevation is modified iteratively until we obtain the best match between modeled and observed gravity. The iteration stops when the standard deviation of the error gets lower than a user-provided value, here 0.1 mGal (1 milli-gal or 1 mGal = 10^{-5} m^2/s) (Fig. 3.9). In order to provide a consistent topographic dataset, we gridded our final bed elevation to the spacing of the MC data, here 450 m, which is not representative of the resolution of our gravity data (4.9 km).

To define an optimal average bed density beneath the glacier and the ocean, we calculate the rate of convergence of the solution in the gravity data misfit, i.e. modeled minus observed gravity, for densities varying from 2.2 to 3.4 g/cm^3 with a step of 0.05 g/cm^3. We find a minimum at a density of 2.88 g/cm^3 for Pine Island (Fig. 3.3). We do not find a minimum for Thwaites and Smith/Kohler, so we use 2.88 g/cm^3 by default. A density greater than the standard 2.67 g/cm^3 is consistent with [*Damiani et al.*, 2014] for Thwaites (2.80 g/cm^3) and the presence of a rather pure crystalline bedrock in front of Pine Island shelf [*Lowe and Anderson*, 2003], but is not consistent with the presence of thick sediments in M2016. To determine the robustness of our solution to the density selection, we compare the results obtained on Thwaites Glacier using a lower density of 2.78 g/cm^3. We find a shift in bed elevation of 35$\pm$13 m.

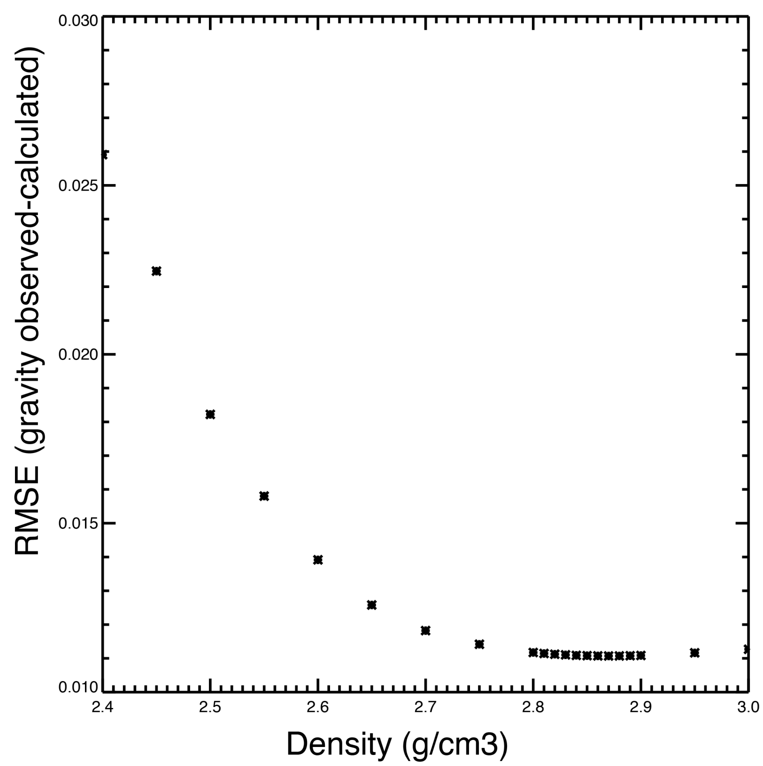

Figure 3.3: *Density sensitivity study for Pine Island Glacier, West Antarctica. Over an area with MC topography and OIB gravity observations, we calculate the misfit between observed gravity and modeled gravity as a function of the density of the bed substrate, with values varying from 2.4 to 3.0 g/cm3 in 0.05 g/cm3 steps and from 2.8 to 2.9 g/cm3 in 0.01 g/cm3 steps. A minimum misfit is obtained for a density of 2.88 g/cm3.*

We use the gravity misfit, or modeled gravity minus observed gravity, to quantify the uncertainty of the inversion (Fig. 3.9). To translate the gravity misfit into an error in bed elevation, we calculate the gravity field using GM-SYS 3D obtained after shifting the bed solution by +100 m and comparing the results with the original gravity field. We find an average shift of 5.8±0.5 mGal in gravity per 100 m of water for the inversion of the Kohler/Smith bathymetry. The statistics of the misfit (mean and standard deviation) are 0.2±3.7 mGal for Pine Island, 0.1±3.7 mGal for Thwaites, and 0.01±3.1 mGal for Kohler/Smith (Fig. 3.9). These misfits translate into an uncertainty in bed elevation of 50 to 65 m. These numbers are a factor 2 to 3 lower than the ±150 m errors quoted by [*Studinger et al.*, 2010] for a 2D, unconstrained inversion, i.e. without AUV, seismic, MBES/IBCSO and MC data.

3.3 Results

The bed elevation deduced from the gravity inversion closely follows variations in free-air gravity anomaly, as expected (Figure 3.4). The results indicate that the glaciers flow down deep troughs that extend on the sea floor beneath the ice shelves and onto the continental shelf (Fig. B.3) [*Jacobs et al.*, 2012]. Bed elevation beneath the ice shelves exceeds 800 m on Pine Island and Thwaites, 1,200 m on Crosson and 1,500 m on Dotson.

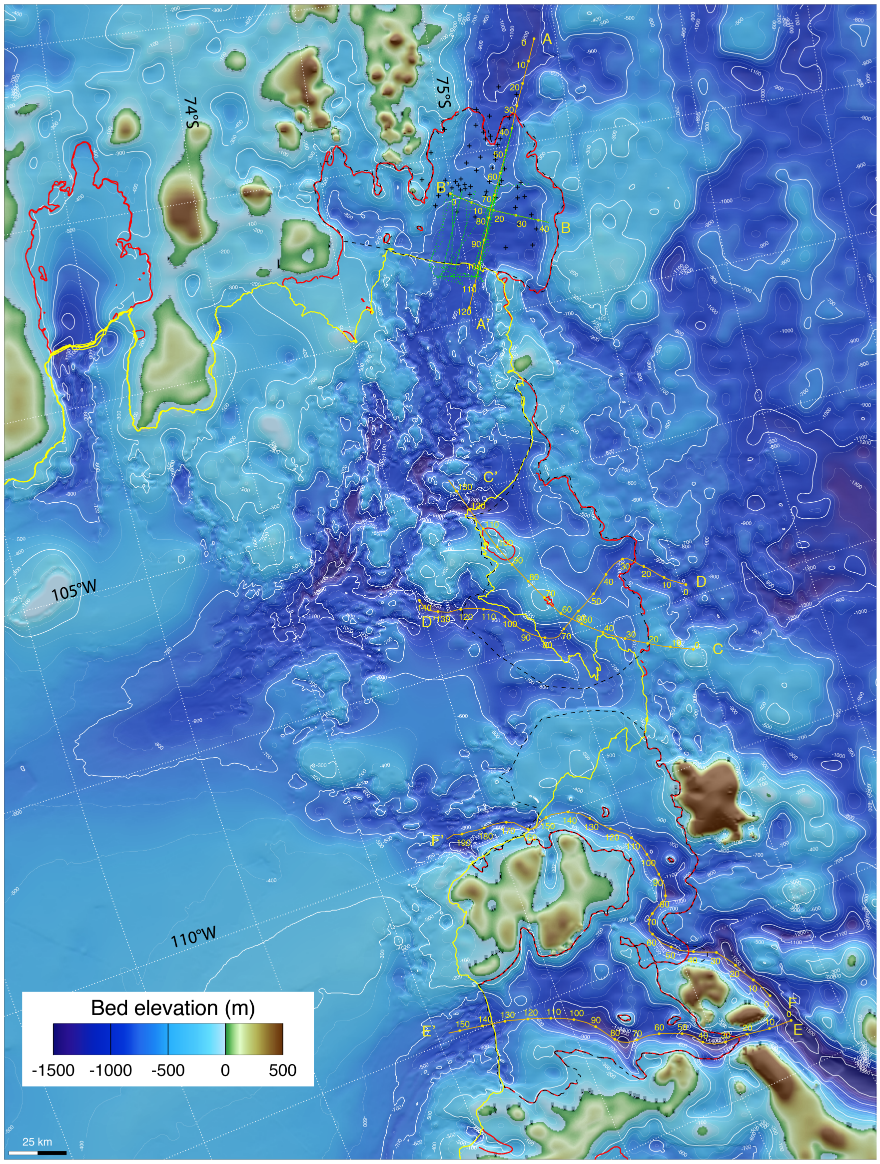

Figure 3.4: *New bathymetry of the Amundsen Sea Embayment (ASE) of West Antarctica with the a) Pine Island, b) Thwaites/Haynes and c) Smith/Kohler glaciers. Grounding line positions are red (year 1996), ice front positions (year 2008) are yellow, AUV tracks are green, and seismic data are black crosses. Bed elevation is color coded from brown/yellow and green (above sea level) to light blue and dark blue (-1,400 m), with light contours every 100 m and thick contours every 400 m. Profiles A-A' to F-F' in orange with dots every 10 km are shown in Figure 3.8.*

Below the Pine Island Shelf, the difference in bed elevation between the AUV data and our inversion drops from -115±101 m without gravity correction to -30±25 m with correction, i.e. a reduction in standard deviation by four (Fig. 3.5). For comparison,the difference

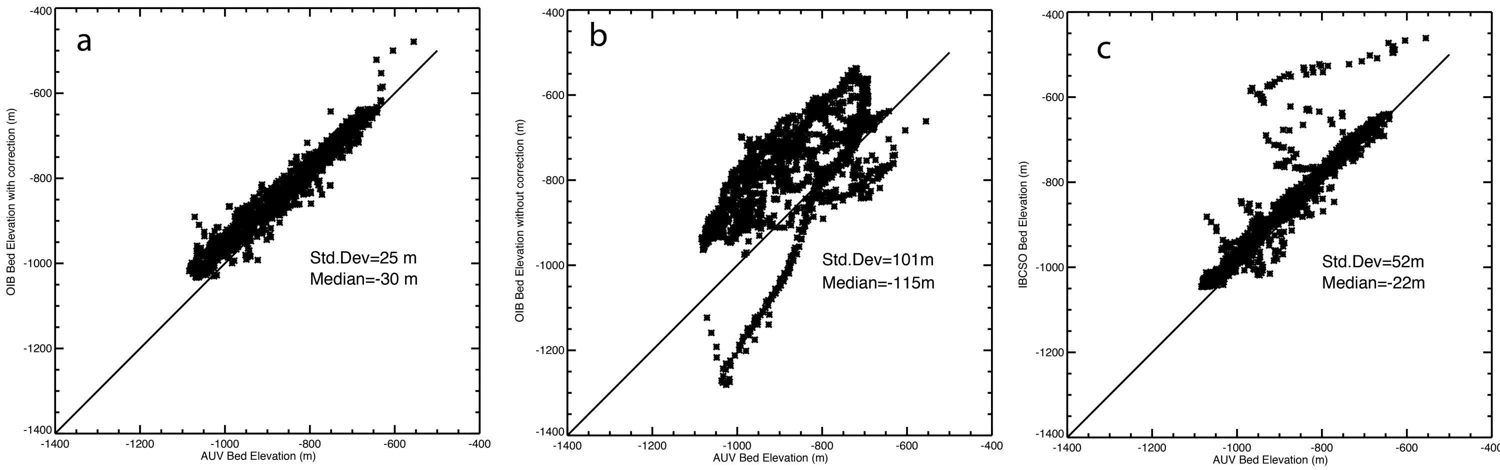

Figure 3.5: *Bed elevation in meters above sea level from Autosub Vehicle (AUV) data in Pine Island Bay, West Antarctica versus bed elevation from OIB (a) with correction for AUV and seismic, (b) without correction, and (c) from IBCSO. Insets indicate the median and standard deviation of the difference between (a) (OIB-AUV), (b) (OIB with no correction - AUV), and (c) (IBCSO - AUV).*

between AUV and IBCSO is -22±53 m. Along profile B-B', the difference between and our solution is -16±31 m versus -162±101 for IBCSO (Fig. S8).

We are in good agreement with the grid from M2016 (Fig. B.5). The difference between their solution and ours improves from -35±127m without correction to -40±103 m with correction (Fig. 3.6). With respect to the seismic data, our solution improves from -38±97 m to -37±57 m with the correction (Fig. 3.6), i.e. a factor two. For comparison, the difference between M2016 and seismic is 21±77 m (Fig. S11). The improved AUV/seismic fitting from our solution also partially reflects the coarser resolution (2.5 km) of M2016.

Our solution confirms that the main channel beneath Pine Island Shelf is undercut by an north-south ridge with a bed elevation at 650 m depth, dropping by 50 m, 5 km south of km 60 in A-A'. Our solution offers a smooth transition with the MC topography and a seamless transition with MBES/IBCSO at the ice front. At the center of the 1996 grounding line, our bed elevation is 200 m lower than BEDMAP-2 and M2016 (red blotch in Fig. B.5 at 100°W,

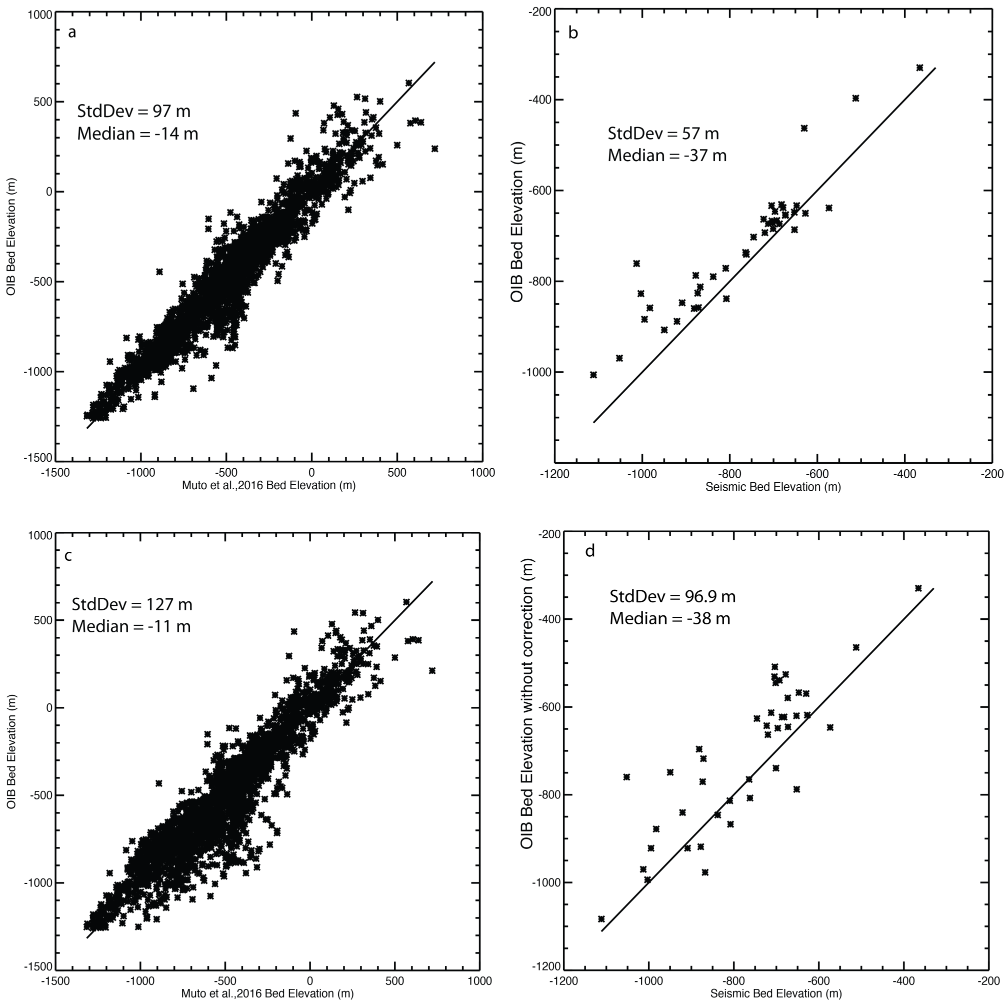

Figure 3.6: *Bed elevation in meters above sea level from this study (a, b) with correction for AUV and seismic data and without (b, d) versus bed elevation from Muto et al. [2016] in (a, c), respectively and versus bed elevation from seismic data in (b, d), respectively, in Pine Island, West Antarctica. Insets indicate the median and standard deviation values of the difference.*

75.25°S). This is an important feature controlling the glacier dynamics. The inversion also reveals a new channel beneath the northern ice shelf of Pine Island, not included in M2016, IBCSO, or BEDMAP-2. The northern channel is 600-800 m deep, with a water column of about 400 m (Fig. 3.7). It connects with two northern tributaries of Pine Island Glacier (Figure 3.1 and B.3). The inversion also highlights a second channel to the southwest, present in M2016 but not in IBCSO or BEDMAP-2, which connects with a southwestern tributary of Pine Island Glacier (Figure 3.1 and B.3). This trough is deeper (about 700-800 m) than the northern channel and extends far inland with depths in the range of 800-1,000 m (Figure 3.4).

For Thwaites, our inversion improves the transition with grounded ice and MBES/IBCSO compared to the inversion of [*Tinto and Bell*, 2011] along the eastern ice shelf and at the grounding line of the fastest-moving portion of the glacier (km 40-20 in profile D-D', Figure 3.4). The bed elevation beneath the eastern ice shelf is on average 100 m higher than the results from [*Tinto and Bell*, 2011]. The water column thickness remains greater than 400 m and bed elevation is about 700 m on average. The east-west ridge, which forms the ice rumples in front of the glacier, is broader and shallower in our solution but more consistent with our delineation of the grounding line from radar interferometry (km 70 and km 90-110 on C-C', Figure 3.8). These improvements result from a 3D inversion constrained with MC, MBES/IBCSO, and OIB gravity data collected after 2009.

Several channels undercut the east-west ridge of Thwaites, one from the east at 1,000 m depth (km 70 in D-D'), rising to 700 m beneath the eastern ice shelf (Figure 3.4). A second one is found along the central part (km 60 in D-D'), starting at 1,000 m depth, but shallowing to 600-650 m as it intersects the east-west ridge (km 50-60 in C-C'). A third pathway is found at km 25-30 along C-C' at a depth of 700 m. At the grounding line, we find a 100-m sill in topography at km 25 on D-D' between the 1996 and 2011 grounding lines along the main trough of Thwaites.

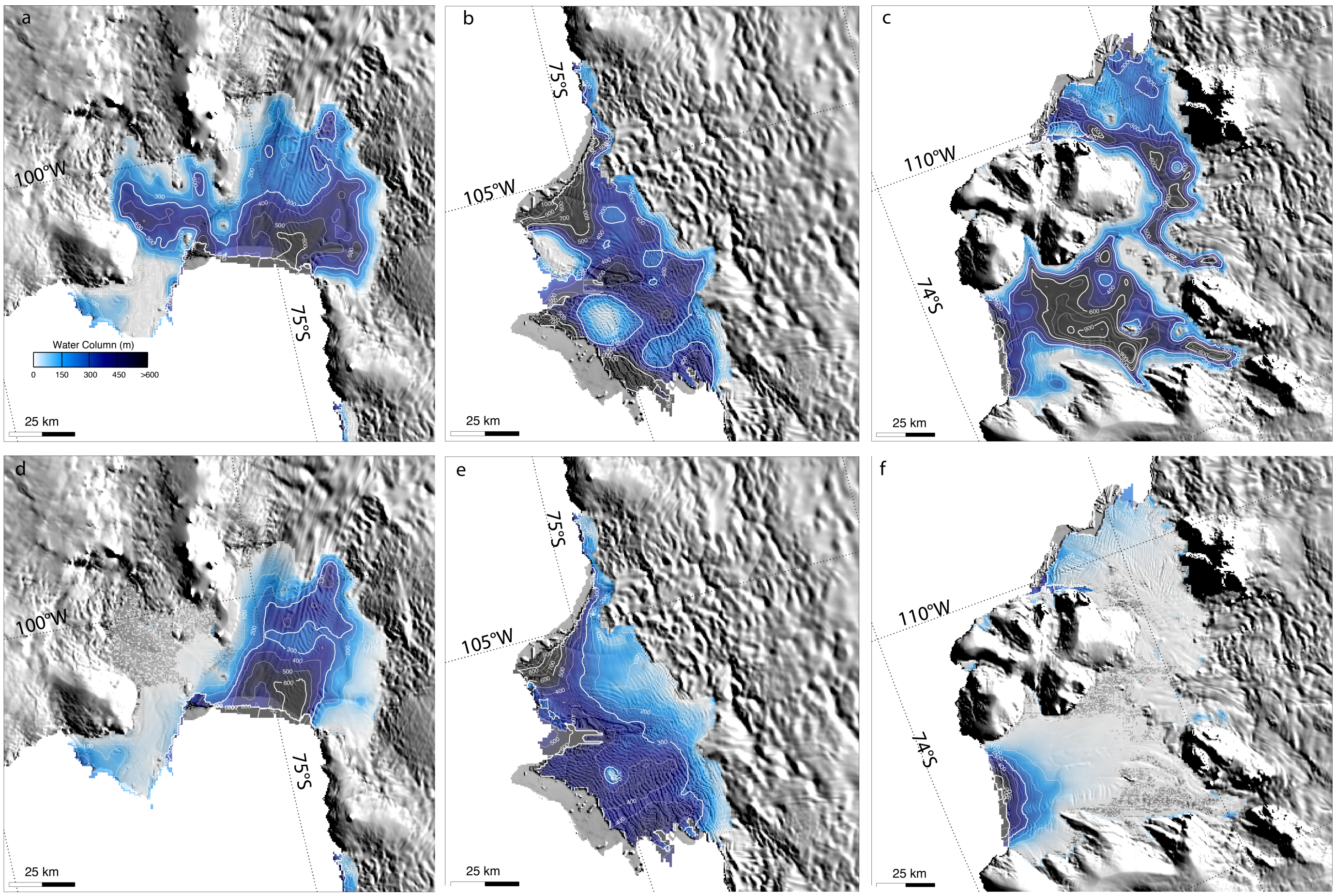

Figure 3.7: *Water column in meters for the sub-ice-shelf cavity in front of a) Pine Island, b) Thwaites, and c) Smith/Kohler glaciers, in West Antarctica, calculated using the bed elevation from this study and the BEDMAP-2 ice shelf thickness, color coded from 0 (white), to 150 m (blue), 300 m (dark blue) and 600+ m below sea level (black) with contour levels every 100 m. No water height is indicated off the ice shelves. Background is a MODIS mosaic of Antarctica from year 2004. For comparison, (d, e, f) show the water column in meters from BEDMAP-2 [Fretwell et al., 2013].*

The most significant improvements in sub-ice-shelf mapping are for the Crosson and Dotson ice shelves since these cavities had virtually been unexplored (Figure 3.4). The inversion reveals deep channels beneath both ice shelves. The bed trough beneath Crosson is at 800 m depth on average and deepening to 1,200 m inland where the glacier has undergone a fast retreat. The trough connects with Pope, Smith East and Smith West. The grounding line of these glaciers follows an east-west ridge with several mounds at 600 m depth. The main bed trough rises to 500 m at km 150 along F-F', near the ice shelf front. The shallow part of the trough at km 150 is only 7-8 km wide. A set of three OIB gravity lines constrain that ridge, which lays only 1 km south of the MBES/IBCSO data, hence relatively well constrained by observations (Figure 3.1 and 3.9). If a narrow passage exists, it has to be narrower than the resolution of the gravity data, or 5 km.

The channel beneath Dotson is deeper, exceeding 1,500 m below sea level at km 30 and 75 in E-E' (Figure 3.4.). At km 30, the over-deepened bed coincides with the confluence of Kohler, a tributary glacier to the west, and a narrowing of the ice shelf to fit the 8-km wide terminal valley of Kohler. The bed rises rapidly along that terminal valley. Near the ice front, at km 125 on E-E', we find the shallowest part of the trough, an east-west ridge at 750 m depth that connects Bear Peninsula and Martin Peninsula. The ridge is about 25 km wide. The water column is more than 400 m thick. The inversion is constrained by MBES/IBCSO along the ice shelf front. We also note an 8-km channel connecting Crosson and Dotson, 700 m in depth, with a water column of 200 m, hence deep enough for water exchanges between the two cavities. Note that all the ice rises have been preserved in the inversion. The presence of many of them on the ice shelves could give the impression that Dotson Ice Shelf - and to some extent Crosson Ice Shelf, have a shallow cavity, but our results reveal that these ice rises correspond to isolated peaks rather than major ridges. The deep ice shelf cavities beneath Crosson and Dotson do not exist in IBCSO and BEDMAP-2 (Fig. 3.7)

3.4 Discussion

The results obtained beneath Pine Island Shelf confirm and complete M2016 by providing a better fit with the MC reconstruction inland and the MBES/IBCSO off shore. The seamless map resolves the pinning point at the center of the glacier (5 km to the east of A-A' at km 45 in Figure 3.4), which plays an important role in the ice dynamics [*Joughin et al.*, 2016]. This pinning point cannot be resolved from gravity alone because of data resolution (about 5 km) but is reproduced on land with MC. The new map reveals a channel to the north that connect with shallow tributaries of Pine Island and a deeper channel to the southwest which connects with a deep tributary.

In this region, the warmest waters have been consistently observed below 700 m, and most of the decadal to sub-decadal variability in ocean temperature is confined to shallower depths [*Dutrieux et al.*, 2014]. Hence the propencity of the region to harbor trough sills that would block access to the ice front for the warmest waters is significant. The east-west ridge in Pine Island between 650 and 700 m depth plays a major role in controlling the advection of CDW to the sub-ice-shelf cavity [*Dutrieux et al.*, 2014]. The deepest part of the ridge, a saddle in the south west, is about 750 m, such that the inner part of the cavity leading to the deep ($>$ 1,000 m) grounding line of the fast flowing trunk is only accessed by the shallower, more variable ocean heat content. Similarly, access to a deep southern tributary in the outer part of the cavity may be limited to a water shallower than 750 m. The northern Pine Island channel is slightly shallower, but the ice shelf draft there ($<$ 450 m) is already self-limiting.

Beneath the Thwaites eastern ice shelf and the central ice tongue, the bed elevation also narrows down to about 700 m depth. These CDW pathways are therefore deep enough to enable intrusion of CDW but limited to shallower, more variable waters above the more consistently warm CDW.

Based on our results, considerable thinning ($>$ 100 m) would be required to detach the

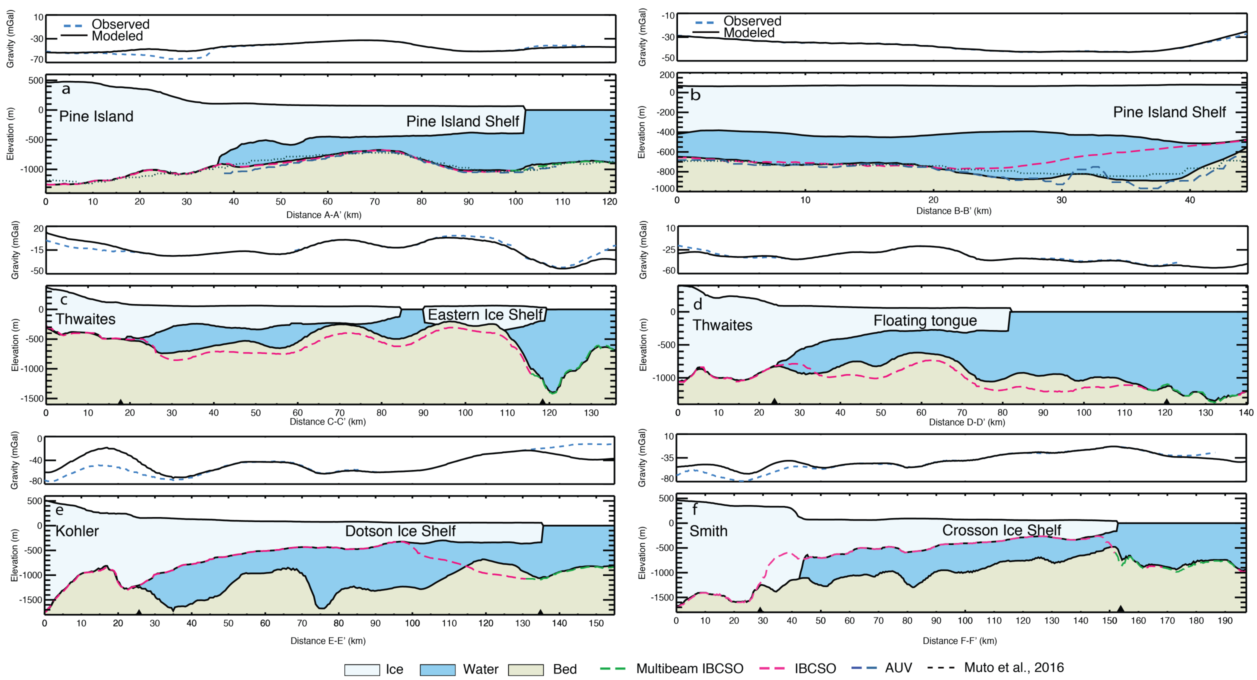

Figure 3.8: *Surface and bed profiles along A-A' to F-F' (Figure 3.4) of a-b) Pine Island, c-d) Thwaites and e-f) Smith/Kohler glaciers associated with Crosson and Dotson ice shelves with the observed (dotted blue) vs modeled (black continuous) gravity on the upper plot, surface elevation from BEDMAP-2, ice bottom elevation from BEDMAP-2, and bed elevation from this study (black), M2016 (dotted black line), multi-beam echo sounding (MBES) from IBCSO (dotted green), IBSCO (dotted red), and Autosub Vehicle (AUV dash blue). Ocean is blue, ice is light blue, and the glacier bed is light brown.*

Thwaites eastern ice shelf from its pinning points (Figure 3.8), which makes this ice shelf more stable than could be deduced from the surface appearance of the ice rumples. At the center of Thwaites, near the grounding line, we find a shallower sill in topography at km 30 in D-D', which is consistent with the rate of fast, continuous and sustained retreat of the glacier at that location [*Rignot et al.*, 2014].

Beneath the Crosson, we find a deep trough that could channelize CDW deep into the cavity but is undercut by a narrow ridge at km 150 in F-F'. The ridge is a robust feature of the inversion but the gravity data are limited to a spatial resolution of 4.9 km.To determine if the ridge blocks the access of CDW or if a passage narrower than 4.9 km exists, higher-resolution data and/or complementary observations would be required.

Beneath the Dotson, we find a similar but broader (20 km for Dotson vs less than 10 km for Crosson) channel with a shallow passage near the ice front, however, deep enough (700-750 m) to enable CDW intrusion. Ice shelf melt rates inferred from remote sensing data collected in 2003-2009 are lower on Dotson (7.8 m/yr) than Crosson (11.9 m/yr) [*Rignot et al.*, 2013]. The bathymetry suggests that CDW has an easier access beneath Dotson Ice Shelf than beneath Crosson Ice Shelf, which is opposite to the contrast in ice shelf melt rate. We conclude that the difference in ice shelf melt rate does not reflect differences in sub-ice-shelf bathymetry but must reflect differences in the source of CDW. Indeed, a lighter, cooler version of modified CDW accesses Dotson Ice Shelf through the Dotson/Getz western trough on the continental shelf [*Jacobs et al.*, 2013] versus the Pine Island eastern trough on the continental shelf that accesses the Crosson Ice Shelf.

Immediately inland of our inversion, the misfit between modeled and observed gravity is significant (Fig. B.2), up to 16 mGal, which suggests that our density selection is not optimum. A more complete inversion would require a more complex geology and the presence of sediments. The misfit however decreases inland and does not affect our solution on land where we use the MC reconstruction. To improve the results beneath the cavities of Thwaites,

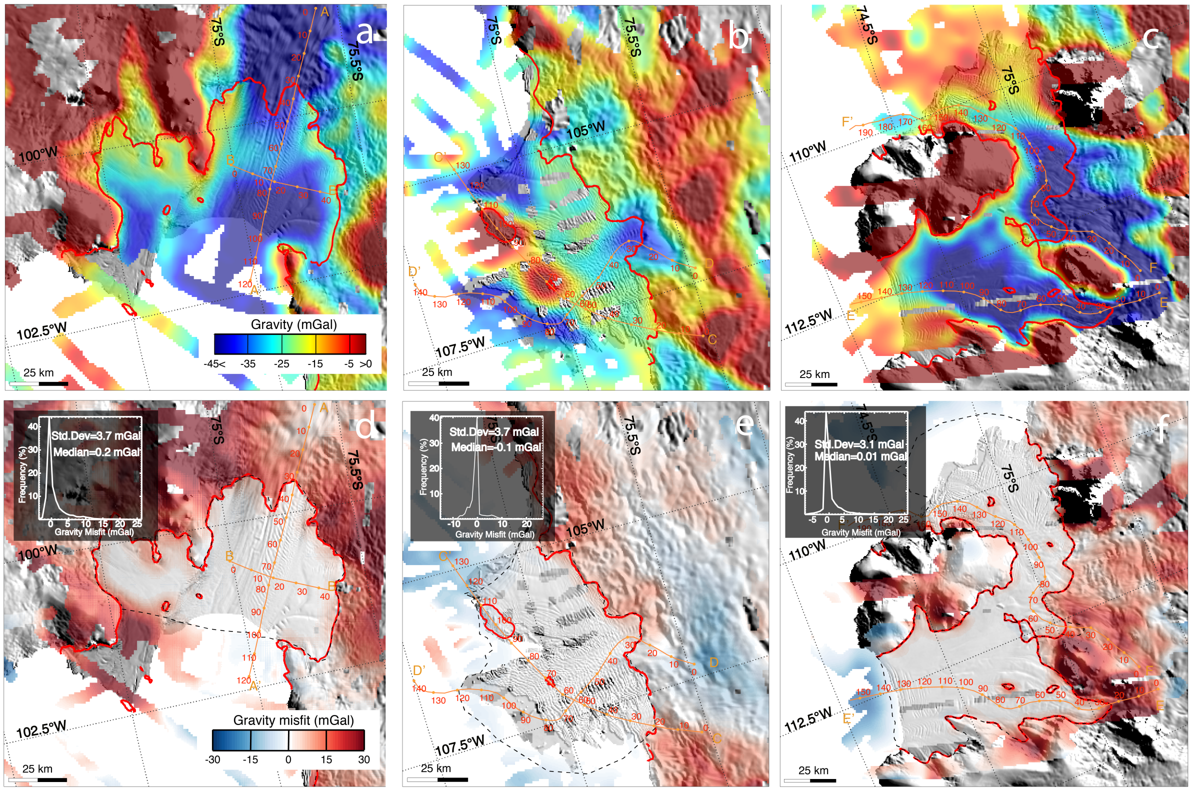

Figure 3.9: *Free-air gravity anomalies (a-c) and modeled gravity minus observed gravity (d-f) in milliGal (mGal) over (a, d) Pine Island, (b, e) Thwaites, and (c, f) Kohler/Smith glaciers, West Antarctica. Insets in (d-f) are histograms of the modeled minus observed gravity with median and standard deviation values.*

Crosson and Dotson ice shelves, additional constraints such as AUV or seismic would be needed. In the case of Pine Island Glacier, the addition of such data reduced errors from 100 m to 25 m. Without additional constraints, errors in bed elevation probably remain above 64 m. The addition of new data would not change the location of the main troughs, but it would also refine spatial details and in particular address the possibility of narrow, unresolved channels (< 5 km).

The novel bathymetry reveals the natural pathways for CDW to access the glaciers, which are critical for ocean modeling and ice sheet flow modeling. The inversion is affected by uncertainties in bed elevation, especially in unconstrained areas. The mapping of sub-ice-shelf channels from gravity however provide invaluable guidelines for future hydrographic and bathymetric surveys. A seamless topography between MC and IBCSO also remains a long awaited critical product in this part of West Antarctica for ice-sheet/ocean numerical modeling studies. Prior mappings, such as BEDMAP-2, do not provide reliable geometries beneath the shelves or realistic transitions at the grounding lines. The new bathymetry should help reduce uncertainties in numerical model simulations. A similar methodology combining MC, IBCSO, OIB gravity and other data should be applied to many other ice shelves around Antarctica that remain unexplored.

3.5 Conclusions.

We presented a novel 3D inversion of the OIB gravity data in the ASE sector of West Antarctica constrained at the land boundary by a high resolution reconstruction of bed topography from mass conservation, off shore by MBES/IBCSO data, and in between by AUV and seismic data in the case of Pine Island. The results refined the details of the Pine Island sub-ice-shelf cavity, suggest a slightly shallower cavity beneath Thwaites and a smoother transition to the grounded ice, and reveal deep channels beneath the Crosson and Dotson Ice Shelves that were not known previously. These troughs provide natural access of CDW to the cavities up to a range of about 700 m depth over the entire glacier system. We expect these data to be of considerable importance for interpreting recent and past changes of this sector of West Antarctica, assist numerical models of ocean circulation, ice sheet flow, and ice-ocean interactions. The data will provide guidelines for future and detailed in-situ surveys.

Chapter 4

Vulnerability of Southeast Greenland glaciers to warm Atlantic Water from Operation IceBridge and Ocean Melting Greenland data.

As presented in: **Millan R., E. Rignot, J. Mouginot, M. Wood, A.A Bjrk, and M. Morlighem (2018), "Vulnerability of Southeast Greenland glaciers to warm Atlantic Water from Operation IceBridge and Ocean Melting Greenland data", *Geophysical Research Letters*, 45, doi:10.1002/2017GL076561.**

Abstract

We employ NASA's Operation IceBridge (OIB) high-resolution airborne gravity from 2016, NASA's Ocean Melting Greenland (OMG) bathymetry from 2015, ice thickness from Operation IceBridge (OIB) from 2010-2015, and BedMachine v3 to analyze 20 major southeast Greenland glaciers. The results reveal glacial fjords several hundreds of meters deeper than previously thought; the full extent of the marine-based portions of the glaciers; deep troughs enabling warm, salty Atlantic Water (AW) to reach the glacier fronts and melt them from below; and few shallow sills that limit the access of AW. The new oceanographic and topographic data help to fully resolve the complex pattern of historical ice front positions from the 1930s to 2017: glaciers exposed to AW and resting on retrograde beds have retreated rapidly, while glaciers perched on shallow sills or standing in colder waters or with major sills in the fjords have remained stable.

4.1 Introduction

The Greenland Ice Sheet has been losing mass rapidly and the rate of ice-mass loss has been accelerating [e.g. [*Rignot et al.*, 2011; *Enderlin et al.*, 2014]. Between 1996 and 2000, Southeast Greenland (SEG) was a major contributor to the mass loss from the Greenland Ice Sheet. In 1994-1999, ice thinning extended to the ice divide with a total mass loss above 17 Gt/yr [*Krabill et al.*, 1999]. This could not be explained by an increase in ice melt alone and required a significant participation from ice dynamics [*Abdalati et al.*, 2001; *Rignot et al.*, 2004; *Rignot*, 2006]. During the last two decades, the glaciers experienced distinct periods of synchronous speed-up and slowdown [*Howat et al.*, 2008]. Individual glaciers have however shown high variability in flow regime and frontal position, indicating that the glacier response to climate forcing is not uniform at the fjord level [*Bjørk et al.*, 2012; *Murray et al.*, 2010].

Off the coast of SEG, the Irminger Current branches off from the North Atlantic Current to bring warm, salty Atlantic Water (AW) in contact with Greenland glaciers to fuel high melt rates along coastal margins [*Christoffersen et al.*, 2011; *Murray et al.*, 2010]. Interpreting the glaciological changes in this region, however, has been hampered by a dearth of data, including knowledge of glacier thickness, fjord depth, and ocean temperature. Most fjords have not been mapped, many glaciers have no name, and measurements of glacier thickness in terminal valleys are affected by uncertainties due to high snowfall and liquid water content that makes the radar depth sounder (RS) challenging [*Mige et al.*, 2016]. The presence of sills or deep fjords that could block or facilitate the access of AW is unknown or has remained hypothetical [*Buch and Meteorologisk Institut*, 2002]. Without these details, it is difficult to understand the impact of ice-ocean interactions on the glaciers and resolve the pattern of ice retreat that affected the ice sheet mass balance in this region in the past decades [*Enderlin et al.*, 2014].

Upstream of the glacier fronts, RS have only measured ice thickness at high elevation ($\geq$ 2,000m), tens of kilometers from the calving fronts [*P. Gogineni*, 2012]. The radar results have been used to reconstruct the bed topography using a mass conservation (MC) approach [*Morlighem et al.*, 2014, 2017]. Downstream of the flux gates, few ice thickness data exist since bed echoes are rare in the echograms. The quality of the MC depends on the precision of the Surface Mass Balance (SMB) reconstruction in a region with steep topography and narrow fjords (a few km) versus the resolution of regional atmospheric climate models (11-km for RACMO2.3, [*Noel et al.*, 2016]. The MC method also requires a precise knowledge of glacier thinning, which is obtained from sparse tracks of OIB or spaceborne altimetry [*Khan et al.*, 2014] over complex topography. Hence, the uncertainty in ice thickness reconstruction accumulates toward the glacier fronts and is maximal at the ice margin, possibly exceeding hundreds of meters in this region.

The 2016 Ocean Melting Greenland mission (OMG) collected multi-beam echo sounding (MBES) data in the fjords of SEG. In some fjords, the data extended to the glacier fronts, providing precise constraints on calving front thicknesses. In other fjords, the glacier fronts could not be reached by boat due to the presence of heavy brash ice and iceberg debris in front of the glaciers. In 2016, we conducted an extensive airborne high-resolution gravity survey of key glacier fronts to complement the OMG data and provide observational constraints on the most challenging sectors of Greenland. This gravity survey builds upon prior efforts at using high-resolution gravity data to resolve bed topography in challenging sectors [*An et al.*, 2017].

Here, we combine the OIB airborne gravity data and OMG MBES data in 10 major fjords occupied by more than 20 outlet glaciers. We constrain a three-dimensional inversion of the gravity data using the MBES data in the fjord and MC on land to obtain a seamless bed-bathymetry mapping across the ice margin. We estimate the uncertainty of the reconstruction and discuss the impact of the results on interpreting the detailed, recent deglaciation history of this part of Greenland.

4.2 Data and Methods

Southeast Greenland is characterized by a rough topography, with elevation ranging from sea level to 3,000 m elevation for the surrounding peaks. The region includes some of the fastest tidewater glaciers in Greenland, with ice velocity ranging from 2 to 8-km/yr (KøgeBugt C., Fig. 4.2). The drainage basin is 81,109 km^2 in area [*Mouginot et al.*, 2017] with a sea-level equivalent of 0.3 m (Table S1). We adopt the glacier name nomenclature of [*Rignot and Mouginot*, 2012]. The survey area is divided into 9 blocks spreading from Narsarsuaq in the south to north of Sujunikajik (Fig. 4.1). The 9 blocks include: B1 for the 4 Ikertivaq glaciers, B2 for 3 KøgeBugt glaciers, B3 for Graulv and Gyldenløve, B4 for A. P. Bernstorff, B5 for Skinfaxe and Rimfaxe, B6 for Tingmiarmiut and 3 Mogens glaciers, B7 for 2 glaciers south of Puisortoq, B8 for Anorituup, and B9 above Qajuutap and Eqalorutsit glaciers (Fig. 4.1).

OIB Gravity data were acquired on a AC.150-B3 helicopter by the Sanders Geophysics Airborne Inertially Referenced Gravimeter (AIRGrav). Eight flights took place between July 27 2016 and August 9, 2016 for a total 5,445-km between Narsarsuaq and Kulusuk airports, which were used as gravity references (Fig. 4.1). The gravity lines were flown at a line spacing of 1 km, with a ground clearance of 80 m, and at a ground speed of 70 knots. The gravity field is sampled at a frequency of 128 Hz. GPS data were recorded at 10 Hz. We used a Riegl® laser altimeter with a single optical laser beam to measure distance to the ground, with a range of 1,500 m, a resolution of 1 cm and an accuracy of 5 cm at a 3.3-Hz sampling rate. Eotvos, normal gravity, free-air, static and level corrections were applied to the data to yield free-air gravity anomalies, which we refer to as "gravity data" in the remainder of the paper. The final product we use was processed using a 20s filter, gridded and low-pass filtered with a 750-m half-wavelength. Data noise has been estimated at less than 0.2 mGal based on a cross-over analysis.

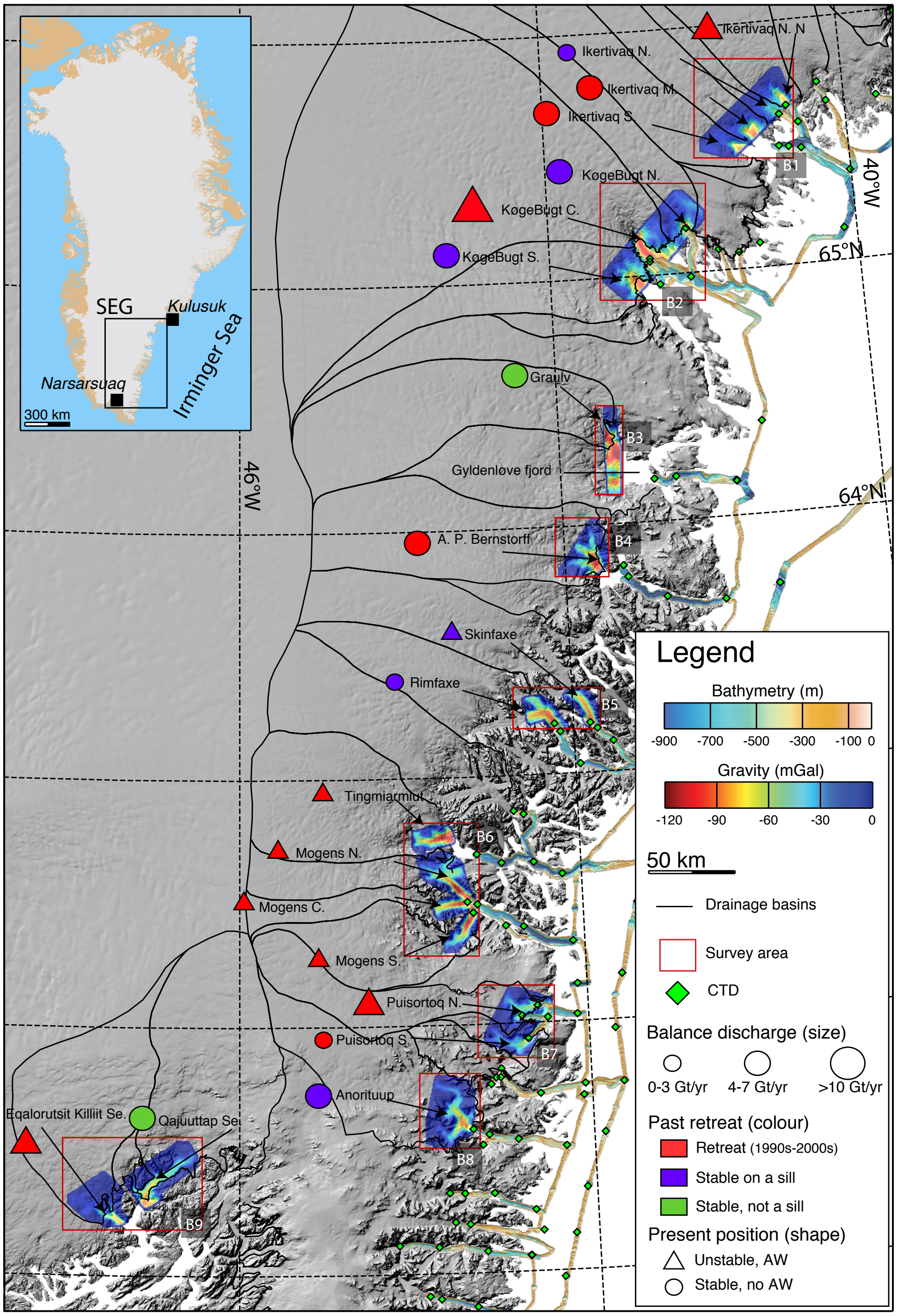

Figure 4.1: *Free-air gravity anomalies (red to blue) in Southeast Greenland overlaid on a shaded relief of the 30-m resolution GIMP-3 DEM. OMG multi beam echo soundings are in shaded relief on a color scale from blue (deep) to orange (shallow). Green diamonds are OMG CTD measurements. Glacier symbols mark the stability of the present front (unstable = triangle, stable = square), size of symbol is proportional to the balance flux, color qualifies the retreat (red=retreat, blue=no retreat on a sill, green = no retreat, not understood).*

Gravity inversion is performed using Geosoft® GM-SYS 3D, which implements the method of [*Parker*, 1973] on a 3D representation of the surveyed area with: 1) a solid ice layer with a density of 0.917 g/cm^3; 2) a sea water layer with a density of 1.028 g/cm^3; and 3) a rock substrate layer with a density discussed below [*Gourlet et al.*, 2016; *An et al.*, 2017; *Millan et al.*, 2017]. A 3D forward model of the gravity anomalies is obtained by combining BedMachine version 3 (referred as BM3) over land, OMG at sea, and a linear interpolation in between to obtain gravity values at every point of the inversion domain (Fig. 4.1). We merge the modeled and observed gravity by adjusting their mean value (or DC-shift) within a sub-region where the OIB gravity and OMG MBES overlap. Where there is no overlap, we use an open land area to calculate the DC-shift (B3, B4 and B9). We allow for a smooth transition between observed and modeled gravity over a length scale of 500 m to 1,500 m depending on the width of the fjord. The inversion is conducted everywhere on grounded ice and extends from the edges of the OMG data to the limit of the OIB gravity survey. The resolution of the gravity data is 750 m but the results are gridded at a 150-m spacing for consistency with BM3 [*Millan et al.*, 2017].

We calculate an optimal bedrock density as the density that minimizes the root mean square error between modeled and observed gravity [*Gourlet et al.*, 2016; *Millan et al.*, 2017; *An et al.*, 2017]. Where we do not find a minimum, we use a default rock density of 2.67 g/cm^3. Because we have no independent information on sediment thickness [*Overeem et al.*, 2017], our gravity inversion does not include a sediment layer. [*An et al.*, 2017] showed that a 100-m thick sediment layer only changes the bed elevation by 30 m, which is within the uncertainty of our inversion defined as the misfit between modeled and observed gravity. We translate this misfit into meters of ice or water using the procedure in [*An et al.*, 2017] and [*Millan et al.*, 2017], which uses a conversion factor of 5.8±0.5 mGal in gravity per 100 m of water. Where reliable RS data are available, we use them to verify the accuracy of our gravity-derived bed elevation.

Ice fluxes are used to evaluate the quality of our gravity-derived bed elevation and ice thickness. We calculate ice discharge at the ice front using ice velocities spanning from 1985 to 1995 derived from Landsat and synthetic-aperture radar (SAR) observations [*Mouginot et al.*, 2012, 2017]. Ice thickness is deduced from the gravity-derived bed elevation and a digital elevation model for 1981-1985 [*Korsgaard et al.*, 2016]. Ice fluxes are compared with the average Surface Mass Balance (SMB) accumulated in each basin for the years 1961 to 1990 using the RACMO2.3 model downscaled at 1 km [*Noel et al.*, 2016]. We define glacier basins using flow direction from a surface velocity reference [*Mouginot et al.*, 2017] (fast flowing ice) and from a reference topographic slope smoothed over 10-thickness from [*Howat et al.*, 2014] (slow moving ice). Our hypothesis is that the glaciers were near balance in the late 1980's, so ice front fluxes should be close to the reference RACMO2.3 balance fluxes [*Rignot et al.*, 2008].

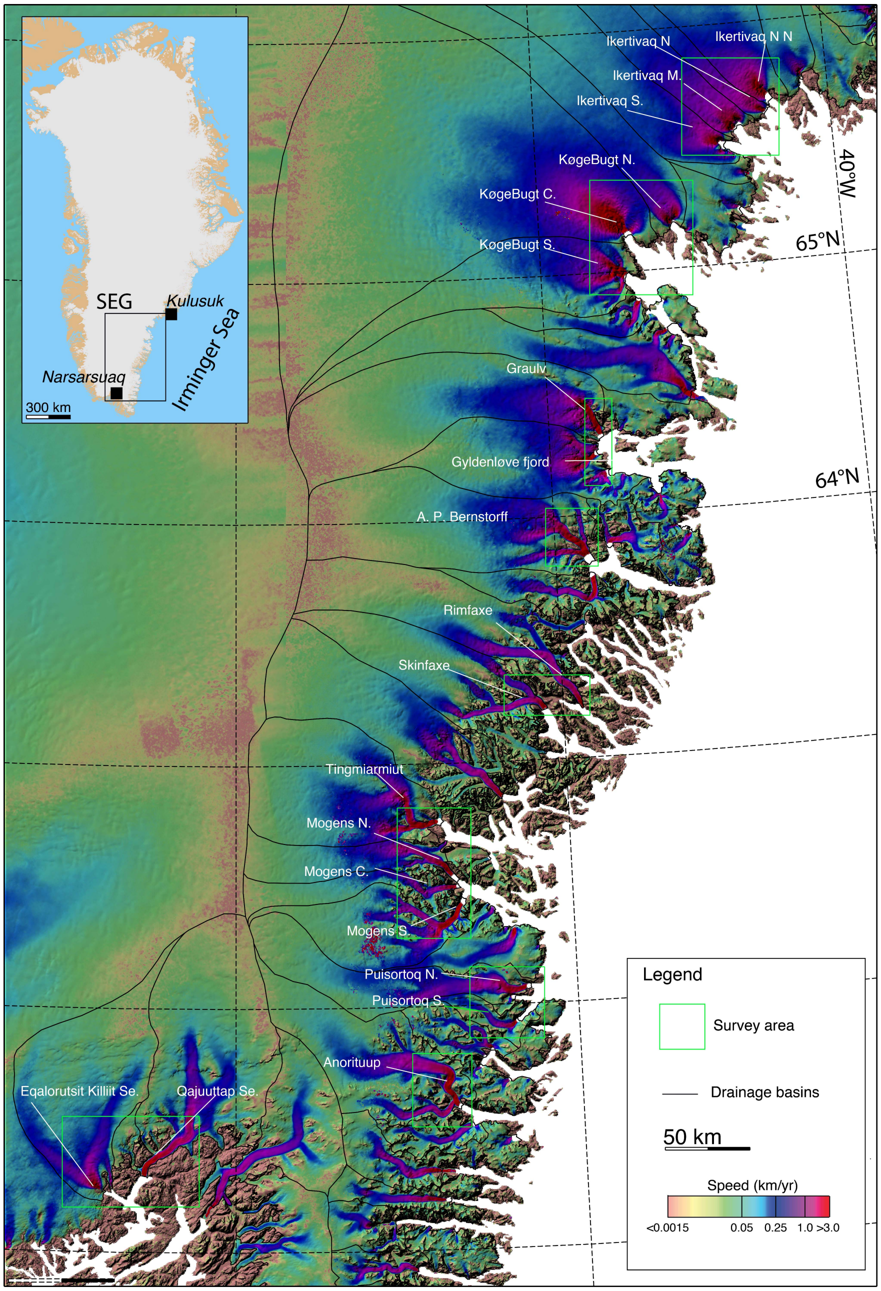

Figure 4.2: *Ice velocity of Southeast Greenland glaciers in 2016 derived from satellite and optical imagery overlayed on a shaded relief version of GIMP3. Green rectangle shows the studied area.*

Ice-front positions are digitized for the last 80 years from aerial photos and historical satellite images. We choose aerial photos from mid to late summer from 1930 to 1985 and Landsat 1-8 images from summer 1990 to summer 2017 [*Bjørk et al.*, 2012] We measure the average ice front position each year (Fig. 4.7 and 4.8) and changes in position following the methods of [*Bjørk et al.*, 2012; *Jiskoot et al.*, 2012].

Ocean temperature and salinity were obtained by OMG in September 2016 in each fjord using 2 conductivity-temperature-depth (CTD) sensors: an AML Oceanographic Minos X CTD in thick brash/sea ice conditions and a Valeport Rapid CTD in ice-free waters. The measurements were taken at a sampling rate of 16Hz. We use the Gibbs-SeaWater Oceanographic Toolbox to convert the conductivity profiles into absolute salinity and pressure into depth. We average CTD profiles in 1 m bin to smooth spurious sensor readings.

4.3 Results

The inversion combines 3 datasets in a seamless fashion: 1) OMG in the fjords, 2) BM3 upstream, and 3) OIB gravity data at the ice-ocean transitions. We find minimum densities for B1, B2, B4, B5, B6 and B9 (Fig. 4.1 and Fig. 4.3) that are ranging from 2.5 to 2.85 g/cm^3, which are consistent with the density of granodiorite and orthogneiss found in this region [*Henriksen*, 2009; *Pechnig et al.*, 2005].

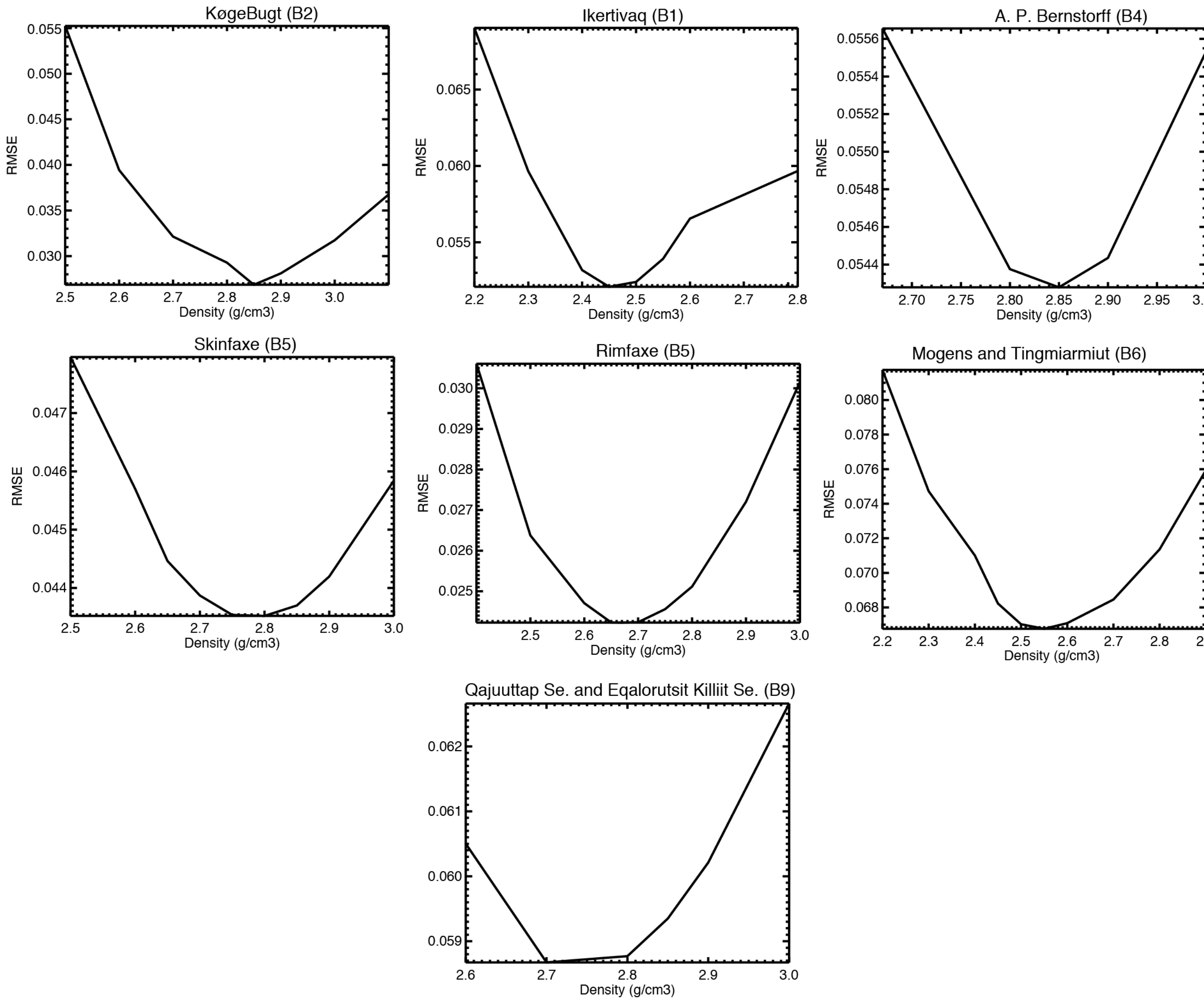

Figure 4.3: *Density sensitivity study for Kogebugt, Ikertivaq, Rimfaxe, Skinfaxe, Mogens, Fimbulgletscher, Qajuuttap Se. and Eqalorutsit Killiit glaciers, Southeast Greenland showing the normalized root mean square error (NRMSE) between observed and calculated gravity as a function of the bed density over the inversion domains shown in Fig. 4.6. Density values varies in increments of 0.05 to 0.1 g/cm3.*

After the inversion, the gravity misfit drops from 8.1 to 1.7 mGal (Table S1). Translated into meters of bed elevation, the inversion reduces the uncertainty in bed elevation from ∼140 to ∼30 m. Differences between BM3 and the gravity inversion are >100 m, hence reflect net improvements in bed elevation mapping. For 5 glaciers (Ikertivaq N. N., M., S., KøgeBugt N. and Eqalorutsit), we observe larger differences in areas where bed mapping with MC did not extend to the coastline and was completed using a krigging interpolation. Finally, in areas with quality RS, the gravity results are in better agreement with the RS observations (Fig. 4.4).

We compare our results with the 2-D gravity-based bathymetry from [*Boghosian et al.*, 2015]. We find that the bed elevation from [*Boghosian et al.*, 2015], were on average 160 m higher. In several places, the frontal bed elevations from [*Boghosian et al.*, 2015] are hundreds of meters shallower than the OMG MBES data (Fig. C.3). This underestimation is explained by the lower resolution of the earlier gravity data (4.5 km for [*Boghosian et al.*, 2015] vs 750 m for our data) which smears the ocean-floor topography in fjords only a few km wide (Fig. C.3 A, B, E, G).

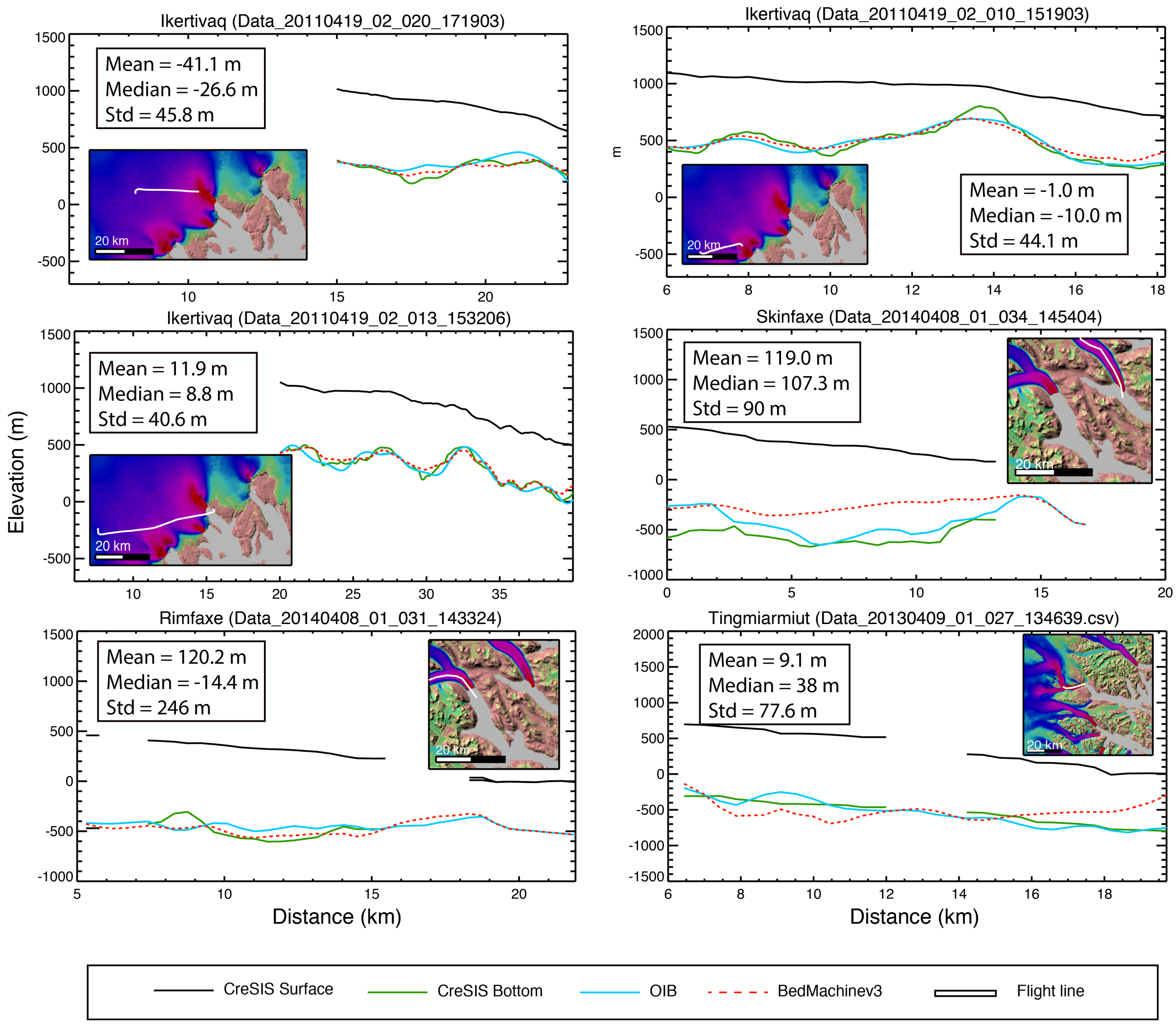

Figure 4.4: *Comparison of bed elevation from CReSIS radar depth sounder data with OIB and BedMachinev3 bed elevations. The inserts show the positions of the flight line and the statistic of the difference between the radar sounder and OIB bed elevations.*

Our new bathymetry includes fjords with no prior depth information (Fig. C.4). In B1, we find a 500-m deep channel in front of Ikertivaq N N (Fig. 4.6A and 3) and a 800-m deep channel for Ikertivaq M and Ikertivaq S S that extends offshore and inland. These deep troughs are not present in BM3. In B2, KøgeBugt C has an 8-km wide, 600-m deep, relatively flat-based fjord (Fig. 4.6B and 4.7). In B3, our new bathymetry reveals a 800-m deep fjord in front of Gyldenløve (Fig. 4.6C and 4.8). The gravity data extends the bathymetry mapping significantly in B4 (A. P. Bernstorff, Fig. 4.6D), B6 (Mogens and Tingmiarmiut, Fig. 4.6F) and B9 (Eqalorutsit and Qajuutaap, Fig. 4.6I) for the first time (4.6 and C.4). Conversely, in B5 and B7-8, the OMG coverage already extended to the ice fronts.

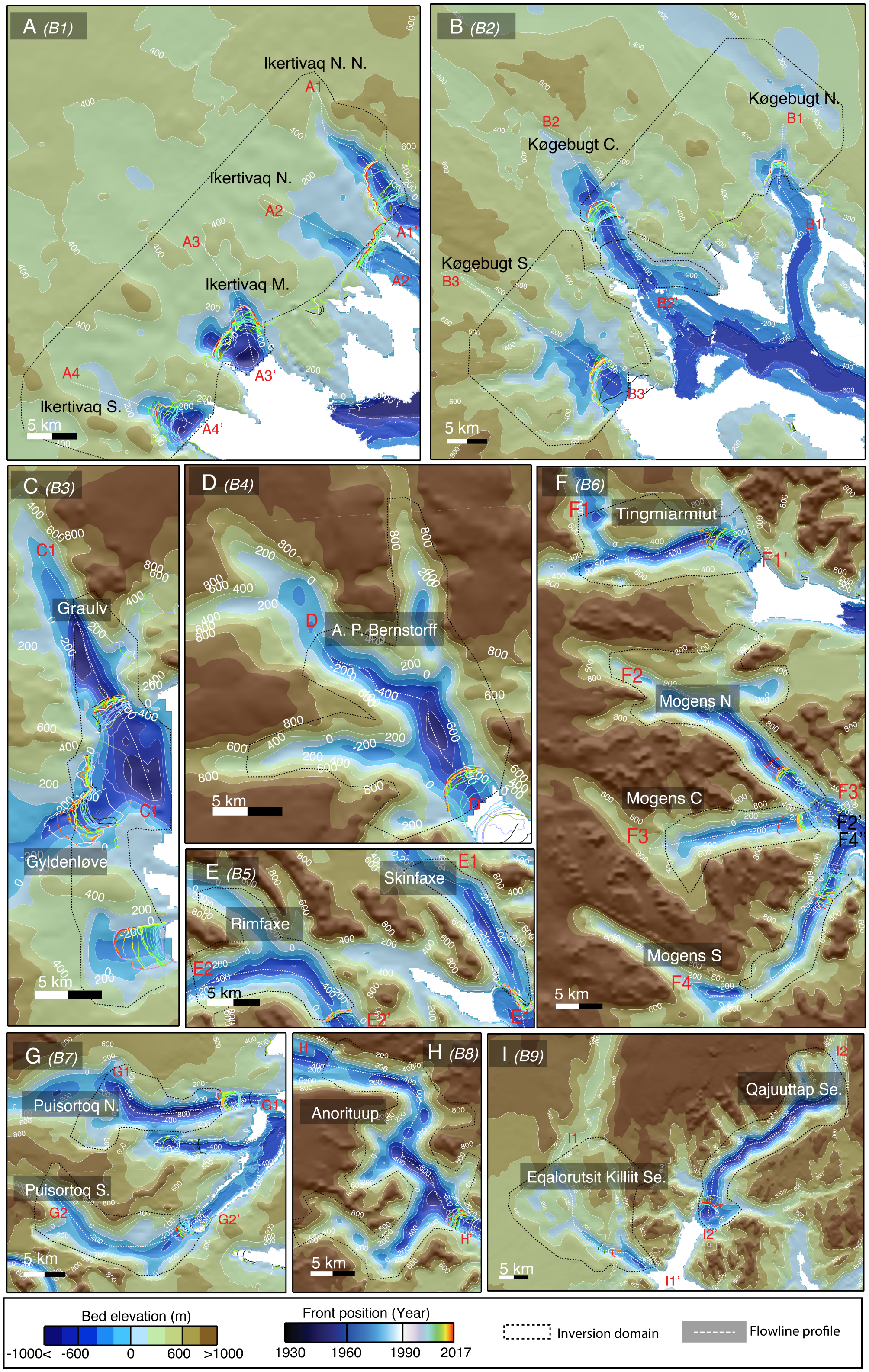

Figure 4.5: *Bed elevation from this study over (A) Ikertivaq (B1), (B) KøgeBugt (B2), (C) Gyldenløve and Graulv (B3), (D) A. P. Bernstorff (B4), (E) Rimfaxe and Skinfaxe (B5), (F) Tingmiarmiut and Mogens (B6), (G) Puisortoq (B7), (H) Anorituup (B8), (I) Qajuuttap Se. and Eqalorutsit Killiit Se. (B9). Contour lines are shown at a 200-m interval. White is no data.*

Inland, our new gravity-derived bed elevation shows significant improvements compared to BM3. In B1, the trough below Ikertivaq N N extends 10 km farther upstream of the ice front than in BM3 (Fig. 4.6A and C.4). For all 4 glaciers, the troughs are on average 400 m deeper than BM3 but shallowing inland by ~500 m over 2-3 km (Fig. 4.7 and 4.8). In B2-B4, our bed elevation is deeper than BM3 for all glaciers (Fig. 4.7 and S9). On Skinfaxe (B5), our bed elevation agrees with BM3 at the edges of the domain but is 200-m deeper at the center (Fig. 4.6E and 4.7) and consistent with available RS data (Fig. 4.4). In B6, the gravity-derived bed elevation is 200 m deeper than BM3 in the ice front region for Tingmiarmiut glacier (Fig. 4.7), but in agreement with RS data (9±78 m in Fig. C.4). Beneath Mogens N in B6, we find a 12-km long, 700-m deep channel, 400 m deeper than BM3, rising to sea level between km 5 and 10 (Fig. 4.6F and 4.7). In B8, the bed is shallower for Puisortoq N., but deeper for Puisortoq S., upstream of the ice front (Fig. 2G and 4.8). In B9, the channels are 300-500 m deeper than in BM3 (Fig.4.6H and 4.7). Qajuuttap Se. and Eqalorutsit Killiit Se. are marine-terminating glaciers instead of land terminating as shown in BM3 (Fig. 4.6I, 4.7 and 4.8).

In terms of ice fluxes, the revised fluxes are within 0.2±0.5 Gt/yr of the 1960-1990 balance fluxes vs 0.8±1.5 Gt/yr with BM3 (Table S1), hence reducing errors by a factor three. More importantly, the total ice discharge for all 20 glaciers is 64.7 Gt/yr, or +5% above the balance flux, versus 47.2 Gt/yr or 24% too low with BM3 (Table S1). The ice fluxes are therefore in better agreement with the balance fluxes. Discrepancies are only found for Anorituup and Ikertivaq S., with a flux in excess of 1.7 Gt/yr and 1 Gt/yr respectively. Explanations for the difference includes: overestimation of the bed elevation, the glaciers were not in a state of balance, or SMB is too low.

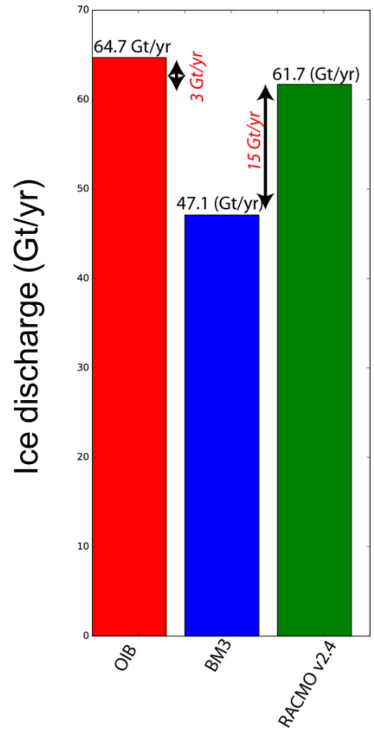

Figure 4.6: *Total ice discharge in Gt/yr of SEG glaciers with ice thicknesses calculated using OIB gravity data (red), BM3 (blue) and balance fluxes for the period 1960-1990 using RACMO v2.4 SMB model. Black arrows and red numbers indicate the difference relative to the balance fluxes.*

The pattern of ice front retreat varied significantly from fjord to fjord (Fig. 4.7). Fast retreats took place along retrograde slopes and retreats slowed or stopped where the glaciers met prograde slopes. We find that 9 of the 14 glaciers for which we have complete coverage advanced on prograde slopes by up to 1 km during the period 1930-1940 (4.6. and 4.8). In contrast, KøgeBugt C., S. (B2) and Puisortoq N. (B7) retreated by 3, 1.5 and 1 km, respectively, on retrograde slopes (Fig. 4.7 and 4.8). Between 1970 and 1990, 13 out of 20 glaciers remained stable or re-advanced on prograde slopes (Fig. 4.6, 3 and 4.8).

Going from north to south, in B1, Ikertivaq N has been stable on a 1.5-km wide and 170-m deep sill for 80 years, while Ikertivaq N N started retreating in 1990 along a retrograde bed and retreated by 4 km until it met a 450-m-deep sill in 2010. The glacier sped up by

1 km/yr or 20 %, while Ikertivaq N, M and S maintained steady speeds [*Mouginot et al.*, 2017]. In this sector, glaciers with no retreat in the last 10 years have been standing on a sill or had retreated to higher ground by 2005. Since the 1990s, KøgeBugt N., S. have been stable (4.6 and 3 and 4.8). For KøgeBugt C, the largest retreat of 3 km took place from 1990 to 2015 along a retrograde slope (Fig. 4.7). Rimfaxe and Skinfaxe have been the most stable glaciers in the region, with an ice front migration of less than 500 m since the 1930s, which we explain by the presence of sills only 350 m deep (Fig. 4.7). Farther South in B6, we detect the largest retreat (8 km) on a retrograde bed for Mogens N after 1965 (Fig. 4.6 and 3). This glacier doubled in speed since the 1990s [*Mouginot et al.*, 2017]. Between 1972 and 1981, the ice fronts of Mogens C and N split in half (Fig. 4.6) and retreated 1.4 km in 10 years. During 2003-2016, Mogens C has remained stable on a 2.5-km wide and 1-km long sill. In 2016-2017, glaciers in B6 experienced a widespread retreat along retrograde slopes of 1.3 km (Mogens N), 2 km (Mogens C) and 0.9 km (Mogens S) (Fig. 4.7 and Fig. 4.8). We note three anomalies: Graulv in B3, Anorituup in B8, Qajuutaap Se. in B9 that retreated less than 2-km since the 1930s despite deep fjords (Fig. 4.7 and 4.8).

Using the 2016 CTD data, we find warm, salty AW widespread in the northern part of the study region (B1, B2, B5) with potential temperatures greater than 3°C below 350-m depth. In the southern part, e.g. in Mogens fjord, the warm water layer (> 3°C) starts at 250-m depth. In Puisortoq N, Puisortoq S and Anorituup fjords, nearly entire water column is warm. We find no major sill at fjord entrances, except for Puisortoq N and Anorituup, where we detect sills less than 300 and 200-m deep, respectively (Fig. C.6). Ocean temperature is high in these fjords and reaches 5°C below -200 m (Fig. C.6). The sills, however, seem to limit the access of warm AW since water temperature is at least one degree lower upstream (Fig. C.6).

4.4 Discussion

These results shed new light on the spatial pattern of glacier retreat in Southeast Greenland. The stability of 70% of the glaciers before 1990 is corroborated by two factors: 1) most calving fronts rested on prograde slopes and 2) sea-surface temperature (SST) were stable in 1930-1940 and cooled down by 1°C in 1960-1970 [*Bjørk et al.*, 2012]. The anomalously fast retreats observed in B2 in 1930-1940 is consistent with the presence of retrograde slopes. In B1, Ikertivaq N N is the only glacier that retreated due to a retrograde bed in a fjord with warm AW. In this area, BM3 has ice fronts at sea level, which is not compatible with the observed changes. In B4, the stability of A. P. Bernstorff since 2005 is explained by a fjord depth of 300 m (vs 500-m in BM3), which means low exposure to AW based on mapped fjords nearby. In B3, Graulv has been stable for 80 years despite its ice front being grounded at 400 m deep. We have no CTD measurements near the ice front and no data between the OIB gravity inversion and the OMG campaign (green circle in Fig. 4.1). We posit that a sill may exist in the fjord that limits the access of AW. Farther South in B6, BM3 is not compatible with the evolution of Mogens N because it displays a shallow (200-m depth) prograde bed elevation not exposed to AW. The widespread retreat observed in 2016-2017 in B6 is however consistent with our mapping: the ice fronts were dislodged from their stabilizing sills (Fig. 4.7 and Fig. 4.8) to retreat along retrograde beds.

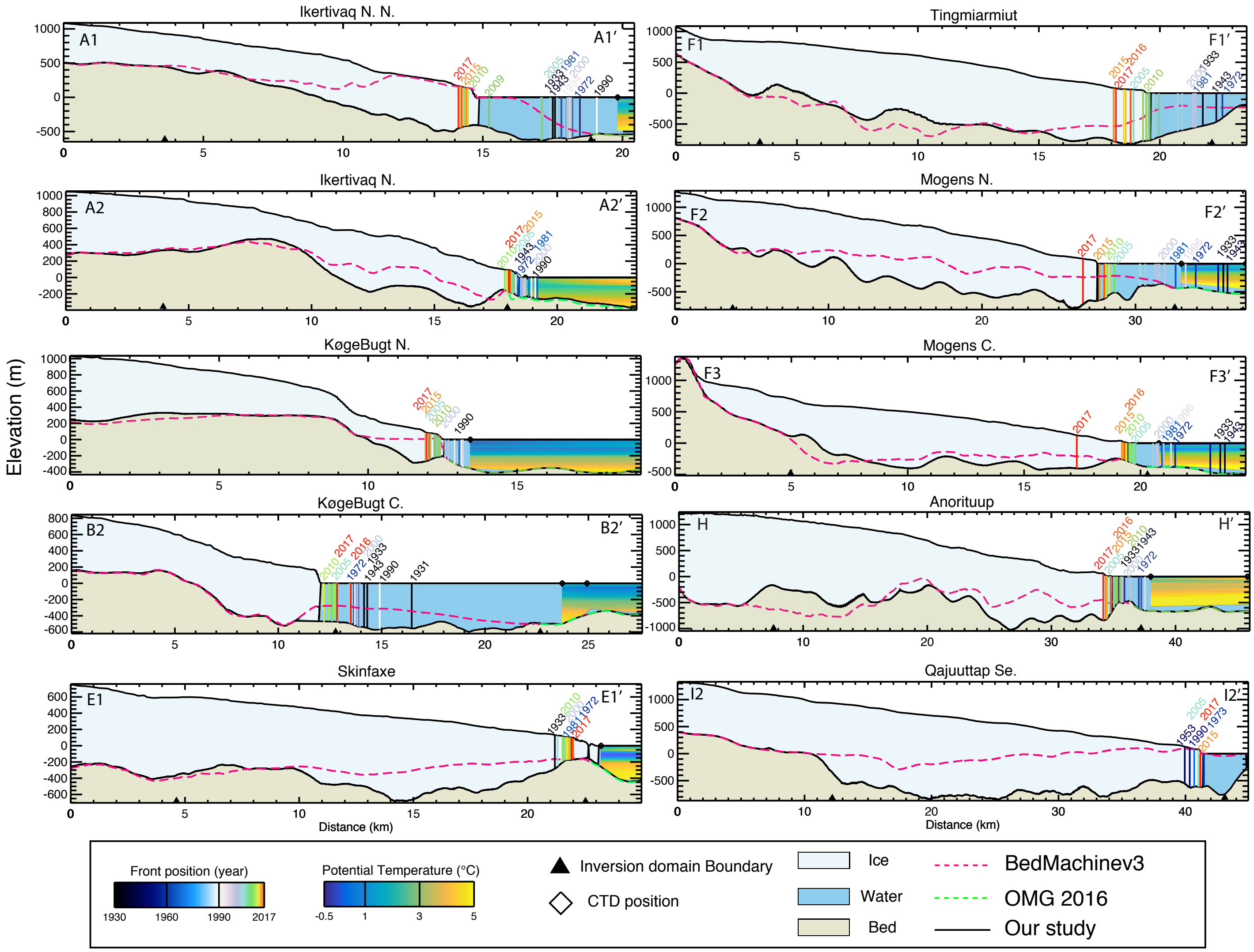

Figure 4.7: *GIMP v2.1 (from BM3) surface elevation along profiles in Fig. 4.6 with bed elevation from BM3 (dotted red), OMG bathymetry (dotted green) and bed elevation from this study (solid black). Ocean is blue, ice is light blue, and bed is light brown. Ice front positions are color coded from blue to red and labeled by year. OMG temperature from CTD casts in 2016 are color coded from blue (cold) to yellow (warm), with CTD position as a diamond. Limits of the gravity inversion are black triangles.*

We note three low retreat anomalies in B3, B8 and B9. In B8, the fjord has a 200-m-deep sill that limits the access of warm AW to Anorituup (Fig. C.5). This glacier also calves at 12 m/d, which is one order of magnitude higher than typical ocean-induced melt rates at ice fronts [*Rignot et al.*, 2016]. In B3 and B9, we have no CTD or bathymetry data outside of the OIB survey and cannot determine the cause of the stability. We speculate that a sill may be present in the unmapped part of the fjord that limits the access of warm AW to the ice. Overall, except for 2 glaciers (Qajuuttap Se. and Graulv) for which we need additional data, the new bed map reveals pathways for warm AW to reach glacier fronts. For 17 out of 20 glaciers, we find bed elevations several hundreds of meters deeper than BM3, which makes the glaciers more vulnerable to AW (Fig. C.5). We have confidence in the results because the derived ice fluxes for 1980s-1990s are in better agreement with the balance fluxes, our results match available RS data, and the misfit between observed and modeled gravity is lower (Table S1). The 20 glaciers that drain this sector of Greenland occupy 5% of the ice sheet in area, with a balance flux of 64 Gt/yr, or 17% of Greenland's ice mass flux in the 1980s-1990s.

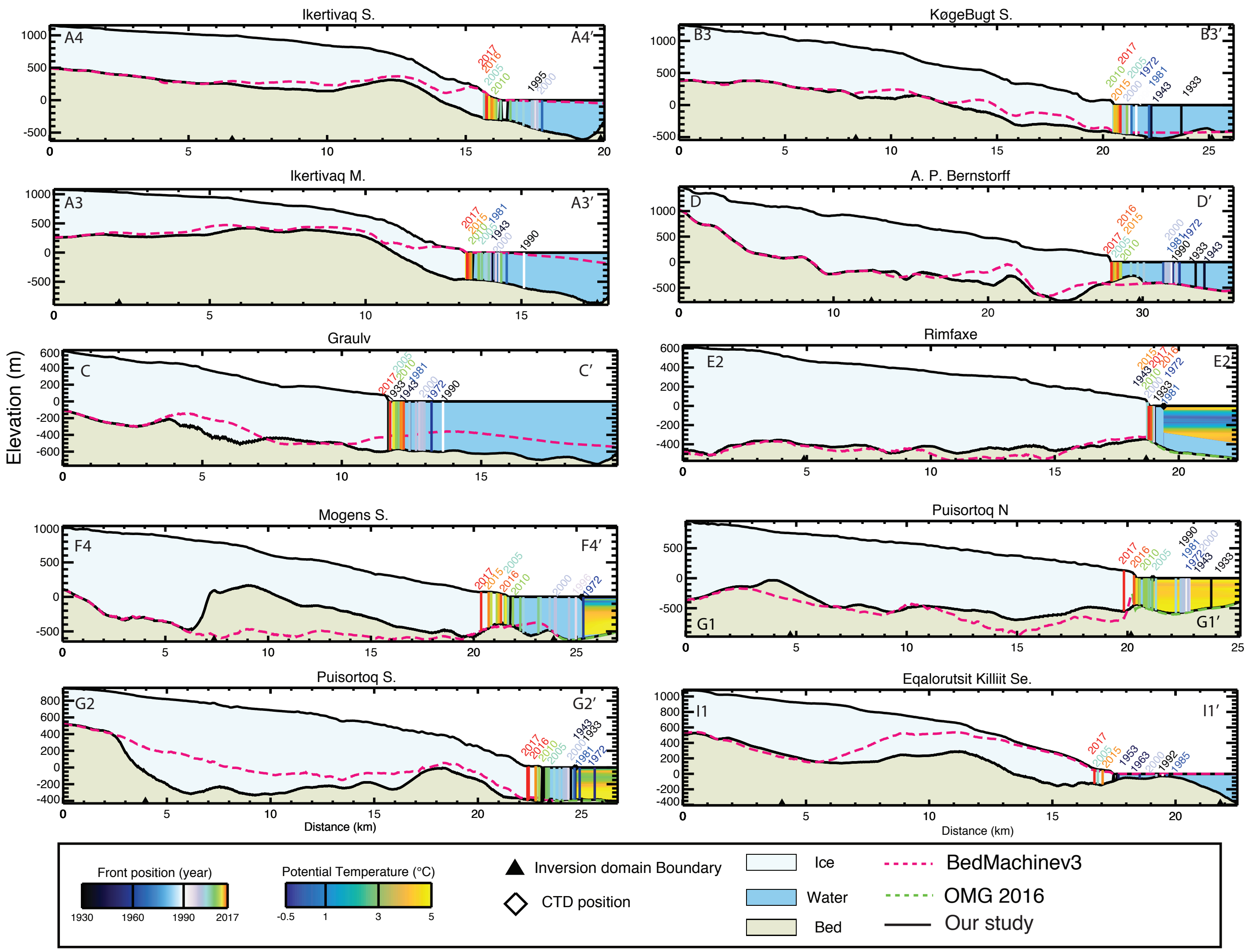

Figure 4.8: *Surface (GIMP v2.1 (from BM3) surface elevation along profiles in Figure 2 with bed elevation from BM3 (dotted red), OMG bathymetry (dotted green) and bed elevation from this study (solid black). Ocean is blue, ice is light blue, and bed is light brown. Ice front positions are color coded from blue to red and labeled by year. OMG temperature from CTD casts in 2016 are color coded from blue (cold) to yellow (warm), with CTD position as a diamond. Limits of the gravity inversion are black triangles.*

During the 1930-1990 period, the ice-front positions were several kilometers downstream of the present positions for 16 out of 20 glaciers (Fig. 4.1). Around the year 2000, 12 glaciers started a significant retreat, while 8 glaciers remained stable (Fig. 4.1). Among the glaciers that retreated, the new CTD data show that more than 60% were exposed to warm AW greater than 3° C (Fig. 4.1). For the remaining 40% without CTD data, the fjords are deep enough that exposure to AW is highly likely. Among the glaciers that have remained stable, >60% have ice fronts with low exposure to warm AW and/or standing above 300 m depth (Fig. 4.1). For 2 glaciers (Graulv and Qajuuttaap Se.), we need additional oceanographic data to understand the stability of the glaciers (Fig. 4.1).

The simultaneous retreat of 6 glaciers in summer 2017 (KøgeBugt C., Mogens N.-C.-S., Puisortoq N.-S.) is consistent with the retrograde bed upstream of the 2016 front positions. We expect that these glaciers will continue to retreat by several km before reaching a more stable bed position (Fig. 4.7 and Fig. 4.8). This new evolution provides additional confidence in our results because earlier maps did not indicate the presence of deep retrograde bed and could not explain this retreat.

4.5 Conclusions.

We present a new bathymetry and bed mapping of Southeast Greenland from a 3D inversion of OIB gravity data over 20 glaciers in 10 major fjords. Our multi-sensor approach provides the first reliable mapping of these inner fjords and terminal valleys where glaciers have been retreating during the last 80 years. The results reveal deep channels hundreds of meters deeper than estimated previously that provide natural pathways for AW to reach the glaciers. The uncertainty in bed elevation has dropped to 30-50 m, or only about 10% of the ice front thickness (versus >50% in BM3). Where we have reliable RS data, we confirm the precision of the inversion. In addition, the ice fluxes from the 1980s are much closer to the balance fluxes, as expected. We also find that the pattern of retreat or advance of nearly all glaciers is consistent with three major factors: 1) the presence of warm AW in the fjords; 2) the existence of retrograde bed and 3) the presence of stabilizing sills or prograde slopes. These results provide multiple, independent lines of evidence of the reliability of the gravity-based bed mapping. We recommend that other glaciers be mapped using a similar method to obtain a reliable glacier and fjord depths. Surveys should extend from the glacier fronts to the mouth of the fjords to fully understand the connection with the surrounding ocean.

Chapter 5

Conclusions

The work conducted in this thesis aims at improving our knowledge of the dynamics of glaciers and Ice Sheets and ice-ocean interactions. In Chapter 2, we have been able to understand *How* the ice dynamics of the glaciers and ice caps of the QEI has been changing through time and its role in the total mass budget. In the ASE (Chapter 3), we provided a detailed mapping of the bathymetry beneath major ice-shelves which gives important insights on the influence of CDW in melting the glaciers at the grounding line. Finally, in Chapter 4, we mapped the bathymetry and bedrock topography at the ice-ocean transition of SEG glaciers and compare it with the 80-year long ice front history, hence understanding *How* and *Why* the glaciers have been retreating. Overall, the work from this thesis presents new estimations of the mass losses, new observations on glacier retreat and new mapping of bedrock and fjord bathymetry to examine the evolution of key regions and the underlying cause for the recent deglaciation observed at the poles.

5.1 Summary of the results

In **Chapter 2**, we reconstructed a 25-year time series of ice discharge of the glaciers and ice caps of the Queen Elizabeth Islands to evaluate its impact on the total losses of the region. Among the 30 major glaciers surveyed in this study, 60% remained stable or even slowed down. We find that 9 glaciers reduced their frontal speed to zero during the time period, suggesting that they stopped calving, as they retreated to higher ground. In total for QEI, we find that D decreased from 1991 to 2000 due to a decrease in flow speed of several glaciers. Between 2000 and 2015, D remained constant because the slowdown of most glaciers was compensated by the speed up of only two glaciers: Trinity and Wykeham. The acceleration of these two glaciers between 2010-2015 accounted for 50% of the total ice discharge from the QEI. At the local scale, D is a significant component of the mass balance for Trinity and Wykeham glaciers. Their acceleration in recent years has tripled the mass loss in their drainage basin. During the time period 1991-2005, the ice discharge contributed 52% of the mass losses, hence was a significant component of the mass budget. After 2005, the mass balance became strongly negative due to a massive increase in runoff. This transition in mass balance coincides with a marked increase in summer air temperature around year 2004 that has continued until present [*Gardner et al.*, 2011]. The loss due to ice discharge therefore contributed only 10% of the total loss, i.e. the loss was dominated by enhanced runoff. The QEI currently contributes less mass loss than Patagonia because of its larger area, but we posit that a change in global mean surface air temperature of 0.3-0.5C for the period 2016-2035 as projected by the IPCC report could potentially increase the mass loss of the QEI to reach the values observed in Patagonia, which is one order magnitude larger per unit area.

In **Chapter 3**, we present a complete sub-ice shelf bathymetry map of the Amundsen Sea Embayment, West Antarctica. The results indicate that the glaciers flow down deep troughs that extend on the sea floor beneath the ice shelves and onto the continental shelf

[*Jacobs et al.*, 2011]. Bed elevation beneath the ice shelves exceeds 800 m on Pine Island and Thwaites, 1,200 m on Crosson and 1,500 m on Dotson. Below Pine Island Shelf, our results are in better agreement with seismic and submarine data from [*Muto et al.*, 2013]and [*Jenkins et al.*, 2010]. The most significant improvements in sub-ice-shelf mapping are for the Crosson and Dotson ice shelves since these cavities had been unexplored. The inversion reveals deep channels beneath both ice shelves. The bed trough beneath Crosson is at 800 m depth on average and deepening to 1,200 m inland where the glacier has undergone a fast retreat. The channel beneath Dotson is deeper, exceeding 1,500 m below sea level. These troughs provide natural access of circumpolar deep water to the cavities up to a range of about 700 m depth over the entire glacier system. We expect these data to be of considerable importance for interpreting recent and past changes of this sector of West Antarctica, assist numerical models of ocean circulation, ice sheet flow, and ice-ocean interactions. The data will provide guidelines for future and detailed in-situ surveys.

In **Chapter 4**, we present a new bathymetry and bed mapping of Southeast Greenland from a 3D inversion of OIB gravity data over 20 glaciers in 10 major fjords south of Kulusuk. Our new bathymetry includes fjords with no prior depth information, hence the gravity data extends the bathymetry mapping significantly. Inland, our new gravity-derived bed elevation shows significant improvements compared to the mass-conservation approach, where 18 out of 20 fjords are several hundreds of meters deeper than any previous estimations. The inversion reduces the uncertainty in bed elevation by more than a factor of 4. Finally, in areas with quality radar depth sounder, the gravity results are in better agreement with the observations. In terms of ice fluxes, the total revised ice discharge is within 5% of the balance fluxes from the SMB model RACMO. Hence, we are finally able to provide an accurate dataset for mass balance estimation in this region [*Mouginot et al.*, submitted to PNAS]. Using our new bathymetry product, we are finally able to interpret the complex pattern of retreat in this region. During the 1930-1990 period, the glacier margins were several kilometers downstream of the present positions for 16 out of 20 glaciers. Among the glaciers that retreated, the ocean temperature data show that the majority were standing in deep, incised bed, exposed to warm Atlantic water greater than 3C. Conversely, we find that glaciers that have remained stable have ice fronts with low exposure to warm water and/or bed elevation standing above -300-m.

5.2 Future implications

The glaciers and ice caps of the Queen Elizabeth Islands, are currently one of the largest contributors to sea level rise. The detailed velocity mapping from satellite imagery has revealed that several marine terminating glaciers have decreased their frontal speed dramatically and now behave as land-terminating glaciers. Further research is needed to monitor these alarming changes with greater spatial and temporal resolution using the latest new era spaceborne ice sheet observations (CryoSat-2, Sentinel-1a/b and -2a/b), that acquires data every six days. Currently, fjords bathymetry, ocean temperature and salinity remain unknown in the Queen Elizabeth Islands. These datasets are crucial to understand the influence of ice-ocean interactions on the unique evolution of marine terminating glaciers (e.g Trinity and Wykeham glaciers) [Chapter 4, *Rignot et al.*, 2016]. Furthermore, our analysis should be extended to other ice masses (Patagonia, Svalbard, Russian Arctic) to accurately understand the evolution of tidewater glaciers and the role of ice discharge on the total mass budget, which remain the largest uncertainty in climate models and SLR projections. Overall, the need for spatially and temporally dense time series of ice discharge is growing as ice sheets models become more complex in the implementation of an ice-ocean boundary, where changes can occur on short time periods [*Mouginot et al.,* 2017]. Variations in surface ice flow velocities are influenced by short-term variations in ice front position, ocean circulation, surges and extreme melting events that directly impacts the ice discharge. Currently, such changes are not properly considered in the mass balance calculations (annual vs seasonal estimates), and ultimately causing biases those estimates. Moreover, while most studies have been limited to the last two to three decades to examine the evolution of glaciers, very few describe the complete pattern of dynamic changes that happened during the last century. Several expeditions were launched in the beginning of the twentieth century that gathered a considerable amount of high-resolution aerial images [*Bjørk et al.*, 2012; *Carbonnell et al.*, 1968; *Bauer et al.*, 1968], that allows for the derivation of changes in surface elevation, ice velocity, and frontal position. Therefore, it is essential to make an extensive use of such datasets to understand the recent deglaciation with regards to the long term evolution of glaciers, and also provide an appropriate observational and numerical description of the ice sheets, before envisioning reliable projections.

The lack of accurate bedrock, fjord and sub-ice shelf bathymetry remain a major challenge for modern ice-sheet numerical modeling intended to constrain ice-ocean interaction that directly impacts the dynamic losses of the ice sheets. Therefore, bedrock topography is essential to analyze past and future patterns of retreat in addition to estimating glacier contribution to sea level rise and understanding the role of ice-ocean interaction in modern glacier changes. In this study, we mapped sub-ice shelves cavities of the fastest glaciers of the West Antarctica Ice Sheet, whose mass loss is channelized through Pine Island and Thwaites glaciers and could soon outpace all other sources of sea level rise [*Mouginot et al.*, 2014; *Dutrieux et al.*, 2014]. The method presented here provides a simple, yet powerful way to map sub-ice shelf cavity with uncertainty that can be easily quantified and reduced when coupled with in-situ observations. The largest source of error remains the simple geology model used. Although, geological studies remain time and financially consuming in Antarctica, our model provides invaluable insights on the shape and depth of the sub-ice shelves cavities that are essential for ice-sheet numerical modeling and sea-level rise predictions. The sea-level rise equivalent of Antarctica is 58-m [IPCC AR5] with more than 90% of this potential contribution coming from the East Antarctic Ice Sheet. The area mapped here represents ~53,895 km^2 or 47% of the ice shelf cavities outside of the large Ronne and Ross ice shelves in West Antarctica. More than 95% of the ice shelf area is unknown and requires additional mapping. This work should be extended to the entire Antarctic Ice Sheet in order to provide accurate sub-ice shelf bathymetry maps for immediate use in ice-sheet and ocean models.

The work presented in Southeast Greenland, allowed us to estimate the true depth of the fjords and bedrock topography at the ice-ocean transition and to interpret 80 years ice front retreat, which was not possible before. Future work in this sector in this sector would be to estimate the exact rate of undercutting to conclude on the influence of ice-ocean interactions on the evolution of marine-terminating glaciers [*Rignot et al.*, 2016; *Wood et al.*, under review]. Over the 10 major fjords that have been surveyed, large portions remain unmapped but are essential for ocean and ice-sheet models because they can hide topographic features that have the potential to block or ease the access of sub-tropical warm waters to the edges of the ice sheet. In this study area, more bathymetry observations are needed to bridge and refine our gravity inversions, specially in the vicinity of Narsarsuaq, Tingmiarmiut fjord, A. P. Bernstorff fjord, Gyldenløve fjord, Køgebugt S., Ikertivaq M. and S. The method developed here also provides a new technique to estimate ice discharge independent of SMB models when other methods have failed to map ice thicknesses, thus reducing uncertainty in mass balance calculations. Similar analysis to estimate ice thickness is needed in other Greenlandic regions such as Central-East and North Greenland where uncertainties in ice discharge remain high, mainly because of a lack of in-situ observation (bathymetry, radar sounder). Finally, while most studies have focused on the fjord level, a more comprehensive mapping is needed on the continental shelves of both Greenland and Antarctica, where bathymetry knowledge is a pre-requisite for the modeling of warm water advection in the fjords. Currently, considerable efforts have been made to gather a comprehensive datasets of fjord bathymetry from in-situ observation, as part of NASA's OMG, the International

Bathymetry Chart of the Arctic and the BM3 product. These field campaign remain time and financially consuming and some large part of the seafloor remain unmapped. The extensive multibeam mapping can be combined with airborne gravity data and bring a crucial spatial constraint to the inversion process that has the potential to provide a comprehensive map of the seafloor bathymetry. While the continental shelf off the coast of Northwest, Southeast and NorthEast Greenland has been covered, more airborne gravity campaign data is needed in Central West, Central East, North and South Greenland, in order to produce large scale bathymetric map of the ocean seafloor. Without such product, uncertainties will remain prominent in ocean and ice-sheet models that intend to understand and predict current and future state of glaciers and ice-sheets in Greenland and Antarctica.

Chapter 6

Next directions and ongoing projects

In this chapter, we briefly present three other ongoing projects that are direct answers to the openings presented in Chapter 5 using the approach described in Chapter 1-4 . We will first (Section 6.1.1) present a project that was performed in collaboration with the University of Copenhagen, that aims at extending the documentation of ice velocity using the large archive of historical aerial images from the National History Museum of Copenhagen. In a Section 6.1.2, we describe how we are currently extending our sub-ice shelve bathymetry mapping in Antarctica, with the mapping of the Getz Ice Shelf. Finally (Section 6.1.3), we present the extension of the techniques developed in Chapter 3 and 4 to provide the first map of ice thickness of the Patagonian Icefield. These projects will soon be submitted to internationally peer-reviewed scientific journals.

6.1 Extending Greenland's ice velocity record using structure from motion technique on historical aerial photography. The case of Store gl. one of Greenland's most stable glacier.

6.1.1 Introduction

Mass losses from the Greenland Ice Sheet has been increasing during the past two decades. The share of these mass losses is due to enhanced runoff (61%) and increased ice discharge from marine terminating glaciers (39%) [*Andersen et al.*, 2015]. In recent times, mapping of ice velocity has improve our ability to calculate large scale mass budget of glaciers and ice sheets [*Mouginot et al.*, 2017]. Specifically, high resolution SAR and optical images made possible to detect accurate glaciers dynamic changes from seasonal to decadal scales between 1990 and present [*Joughin et al.*, 2004; *Moon et al.*, 2014; *Mouginot et al.*, 2017]. Several expeditions were launched in the beginning of the twentieth century that gathered a considerable amount of high-resolution aerial images that allows to derive changes in surface elevation, ice velocity and frontal position [*Bjørk et al.*, 2012; *Carbonnell and Bauer*, 1968; *Bauer*, 1968]. It is thus essential to make an extensive use of such datasets to understand the recent deglaciation with regards to the long term evolution of glaciers, but also to provide an appropriate observational and numerical description of the ice sheets, before envisioning reliable projections.

In this study, we propose to map half a century of ice velocity of a large outlet glacier of the Northwest Greenland coast: Store (70^o22 N , 50^o38 W) using aerial images stored in the Museum of Natural History of Denmark. Store glacier has an ice front that is 5-km wide and has been flowing at a speed of 7 km/year in 2016. The flow and the ice front position of this glacier has been incredibly stable since the 90s, which gives us a good point of comparison for ice velocity derived in the 50s from historical aerial images.

6.1.2 Data and Methods

Historical and aerial data Images have been scanned from various sources. Pictures from 1953 and 1964 were scanned from contact copies on a flatbed scanner with a resolution of 600 dpi. The airborne images from year 1957 were scanned from a film on a flatbed scanner with a resolution of 1200 dpi. All images were recorded on 24x24 cm film with a focal length of 153mm. The 1953 campaign was part of a general topographic mapping campaign in the area, and we take advantage of overlap between flight lines recorded on different days. The 1957 and 1964 images were part of two dedicated missions to map glacier velocities [*Bauer*, 1968; *Carbonnell and Bauer*, 1968].

We further supplement our mid-20th Century aerial photographs with historical velocity measurements measured in 1893 during the Gronland-Expedition der Gesellschaft fur Erdkunde zu Berlin led by Erich von Drygalski [*Drygalski*, 1897]. These early measurements were pioneering in providing the first estimates of ice movement to the sea, and serve here as a testimony of a very stable outlet. The timing of Drygalski's measurements are of particular interest as they fall immediately after the end of the Little Ice Age, during a period where many glaciers in the region were rapidly retreating [*Weidick*, 1968]. The frontal portion of Store Glacier, has in contrast remained remarkably stable both in terms of its frontal position and also as Drygalski's velocity measurements suggest in terms of speed.

For comparison, we test out method of speed generation from print copies and negatives to those made during the EGIG-expeditions [*Carbonnell and Bauer*, 1968; *Bauer*, 1968]. As we are able to provide a full map of speeds we can measure the differences on the point observations provided in the original work.

Ortho Image processing Prior to analysis, images were processed in Adobe Photoshop in order to highlight contrast on white snow/ice and on dark bedrock. Large frames and strip information is cropped from images, but not spatial distortion or correction is performed.

We used the software Agisoft PhotoScan Ver1.3.1. to perform the bundle block adjustment of the images and create the orthorectified images used for the velocity analysis. We do not incorporate Ground Control Points (GCPs) in the first phase of the process, but instead generate a dimensionless relative elevation DEM from which the orthorectification is based on. This relies on the calculated camera position for relative geometry and assumes that the images were recorded with a perfect vertical camera alignment. In the second phase the orthoimages are georectified by tying it to a referenced orthoimage, in this case a 2-m aerial picture from year 1985 referenced to WGS84, UTM zone 22N. For each pair, we rectify one image to the 1985-orthoimage [*Korsgaard et al.*, 2016]. The orthoimage chosen for the first georectification is the one of the two with the most ice-free area available. This first rectified ortho image of the pair is then used as the master for the rectification of the second image. We rectify using a minimum of four points surrounding the target of interest (in this case the glacier ice). We use only a first order polynomial-rectification, which fits the image to a flat plane, thus assuming that the initial orthorectification was correct. We test this assumption by evaluating the root mean square (RMS) of the residuals from the tie points used in the georectification. With RMS values ranging from 1.28-9.89m for the six images used (see Table 6.1), we argue that the initial orthorectification without the use of GCPs has been satisfactory. By relying on the relative elevation model created for the orthorectification, we bypass a potential high error in locating absolute (x,y,z) GCPs from other remote sensing products.

Date	Ortho-reproj error (pixels)	Ortho-reproj error (m)	Ortho-pixel size (m)	Georec RMS (m)	Ortho-error (m)
1953-07-03	0.6	0.9	1.6	9.9	9.9
1953-07-08	0.8	1.4	1.7	5.2	5.3
1957-07-12	8.9	2.7	0.3	3.4	4.3
1957-07-17	4.3	1.3	0.3	2.2	2.5
1964-06-08	0.5	0.9	2.0	3.9	4.0
1964-06-22	1.2	2.3	2.0	1.3	2.6

Table 6.1: *Uncertainty from the orthorectification and georectification process for each images. Date is in column 1, ortho reprojection error in column 2 and 3, pixel size in column 4, georectification root-mean square error in 5 and error on the ortho-image is in column 6.*

The RMS value along with the image displacement from the orthorectification process is used in the calculation the total error of the velocity (see Table 6.2). The biggest source of error is originating from the georectification to the 2-m 1985 orthophoto, while the error coming from the reprojection during the orthorectification process is almost substantially lower.

Date of the Pair	Ortho-pair error (m)	Cross-correlation error (pixels)	Speed error (m/yr)
1953	11.3	0.1	839
1957	6.9	0.1	511
1964	5	0.1	24

Table 6.2: *Source of uncertainty for each pairs. Orthorectification error is shown in Column 2, cross-correlation error in Column 3 and final speed accuracy on the speed in Column 4.*

One of the problems faced by the original EGIG study of 1957 was the short time interval between the repeat images, leaving a larger relative uncertainty in the measurements. Since no information is available on the time of the capture (only the date), we take into account the position of the sun in the images, and thereby calculate a more precise interval between acquisitions.

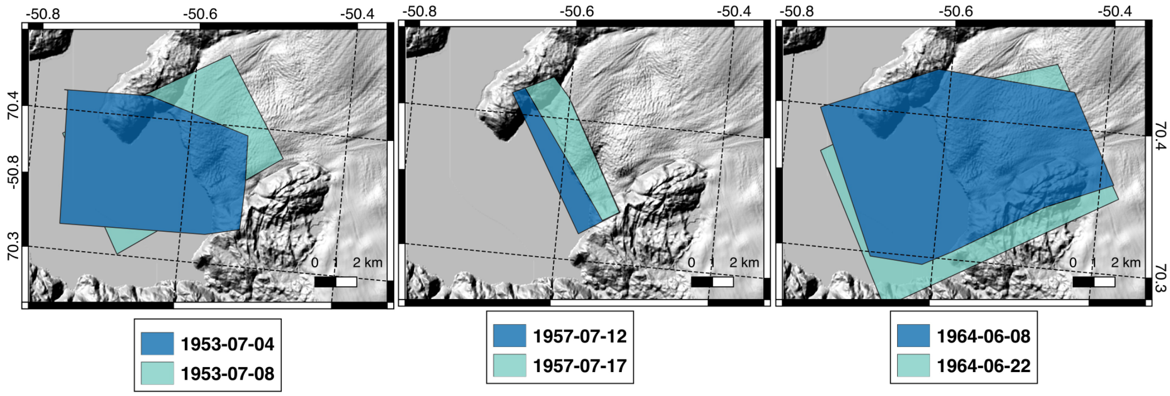

Figure 6.1: *Pair of aerial imagery used in this study overlaid on a shaded version of GIMP Digital Elevation model.*

Ice velocity For historical ortho-images (Figure 6.1), we used trackable surface features such as crevasses or seracs to track the ice flow. A 3x3 Sobel filter was used to enhance surface features, reduce saturation and effect of albedo changes [*Dehecq et al.*, 2015]. The ice displacement was computed using ROI PAC's ampcor routine. Due to the high resolution (2-m) of the pictures, we used large windows size adapted for the temporal baseline of each pairs (see Table 6.3). The uncertainty on the ice velocity is calculated by taking into account the error on the orthorectification and georefencing of the original aerial images.

Date of the Pair	Window size
1953	16x16
1957	128x128
1964	256x256

Table 6.3: *Windows sized used for each pairs in ampor algorithm.*

We supplement our analysis with data from recent satellite sensors between 1970 and present. We use Synthetic Aperture Radar (SAR) and optical data from the Japanese L-band sensor

ALOS/PALSAR radar satellite (23.6 cm radar wavelength), the Canadian RADARSAT-1/2 data acquired in C-band (5.6 cm radar wavelength), the European ERS-1/2 C-band, Sentinel 1-a C-band, and the US Landsat 7/8 satellites. The same feature and speckle tracking algorithm as for the aerial images is used to calculate ice velocity. Cross-correlation is performed on image patches that are 350mx350m in size on a regular grid with a spacing of 150-m for both SAR and optical images [*Mouginot et al.*, 2012, 2017].

Ice fronts Additionally, we mapped ice front position between 1943 and present. We used aerial pictures for the period 1943-1980 and recent Landsat 1-8 images for the period 1980-present. The average ice front position is used for comparison with the ice front velocity.

6.1.3 Results

Our new maps provide ice velocity at a resolution of 2-m that covers the entire cross section at the glacier front but have different coverage inland. In 1953, our mapping extends 3-km upstream of the ice front whereas the map from 1957 cover an area that extend only 1-km inland, due to the limited overlap between the two aerial pictures (Figure 6.1). The pair from 1964 has the largest coverage, up to 6-km upstream of the ice margin, hence increasing significantly the mapping done by the EGIG survey. Uncertainty on the ice velocity combines error on the ortho-rectification and on the cross-correlation algorithm (see Table 6.2). The most complete ice flow map is obtained for the pair in 1964, where repeat images are 75 days apart, with an uncertainty of 20-m which is comparable to modern-day satellite remote sensing data. As expected, the uncertainty on the ice velocity is the largest for the 1953 pair (800 m/yr) where the images are only 5 days apart and where the orthorectification error is the largest (11-m). Overall, this maximum uncertainty represents only 10% of Store average ice velocity during the last 20 years. Hence, using this method for slower glaciers would require large temporal window, in order to reduce the noise level.

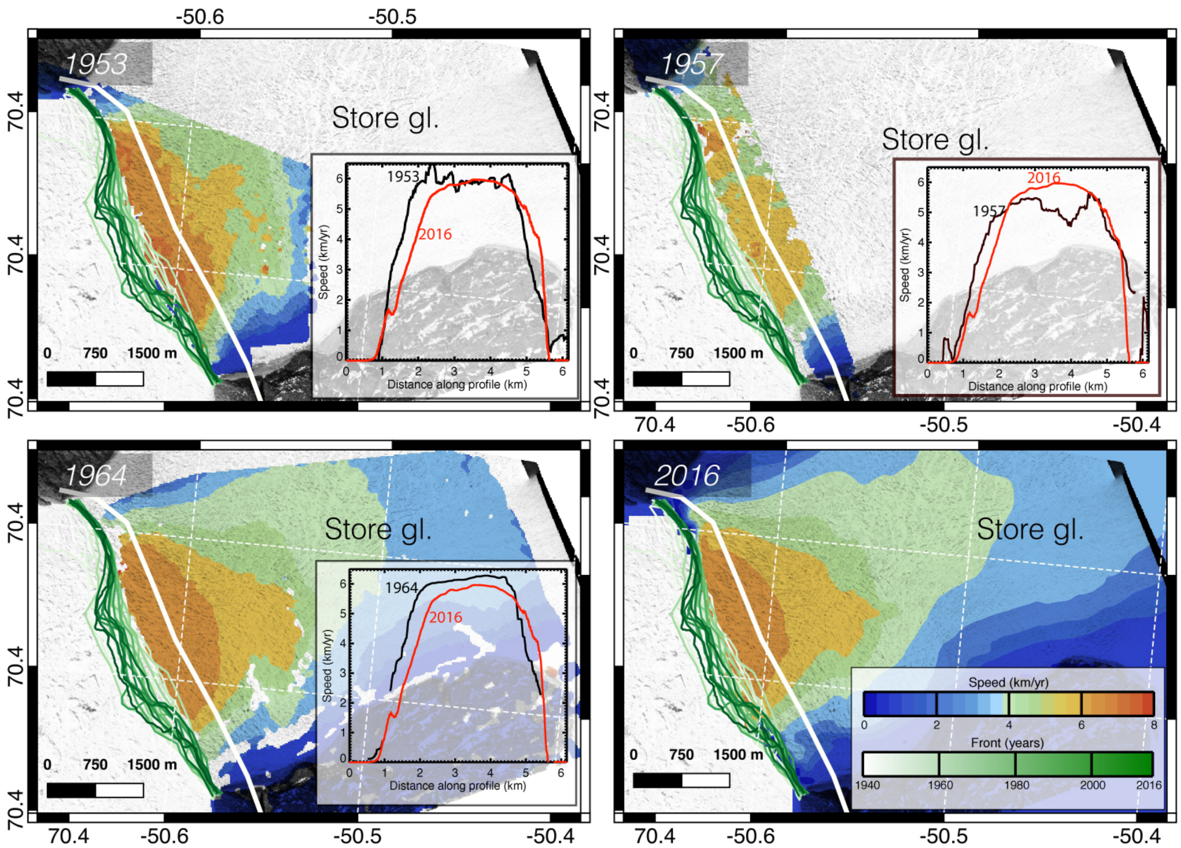

Figure 6.2: *Ice velocity from our study in 1953, 1957, 1964 (our study) and 2016 [Mouginot et al., 2017] overlaid on an orthoimage from 1964 on a linear color scale going from 0 km/yr (blue) to 8 km/yr (red). Ice front positions are shown on a green color scale color coded from 1940 to 2016.*

Over the frontal cross section, our new velocity maps capture the same trend close to the shear margin (Figure 6.2), with a steeper gradient than [*Mouginot et al.*, 2017] for the three different periods (~1-km/yr larger), which is expected considering the large differences in resolutions (150-m vs 2-m). Comparing with the latest 2016 ice velocity map from [*Mouginot et al.*, 2017], we find that the ice velocity in 1953 and 1964 was slightly larger than 2016, with a median over a frontal cross section of 118 m/yr and 335 m/yr respectively (Figure 6.1). In the centerline region, the highest velocity peak was in 1964, where it reaches 6.2 km/yr at the ice front (Figure 6.1). Slower flow rates are found in the centerline for the pair in July 1957, where we find that the ice-velocity was on average 530 m/yr, 1 km/yr lower than the one measured in 1953/2016 and 1964 respectively. On the southernmost margin of the glacier, the pattern of ice flow is however consistent with the speed in 1953 and 1964 and capture the same sharp gradient.

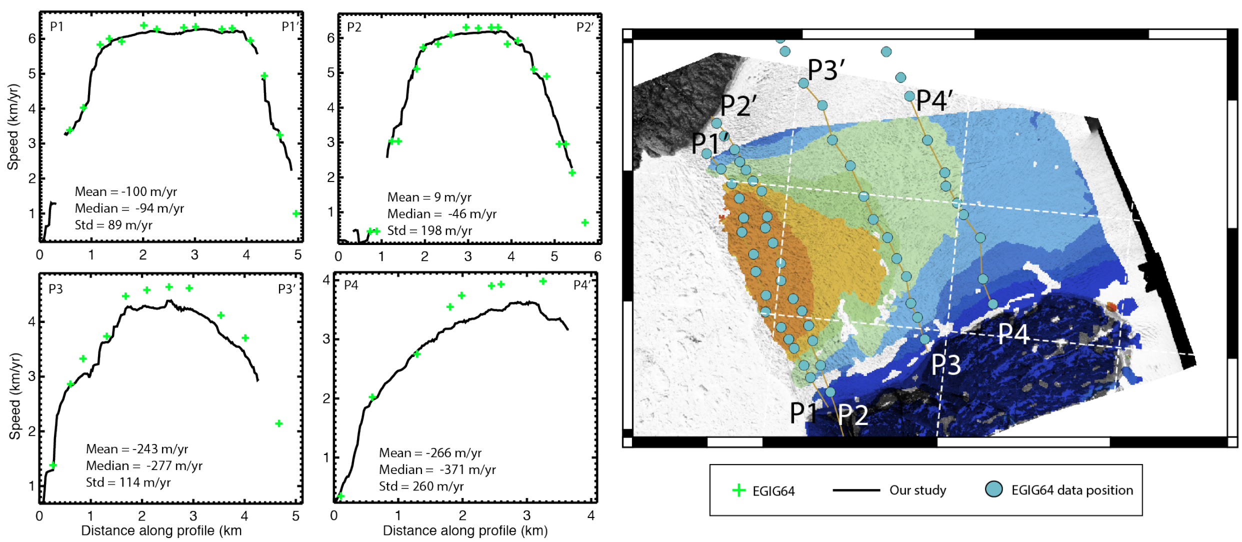

Figure 6.3: *Profile along EGIG64 gates measurements from our study (solid black line) and from EGIG64 (yellow star). The position of points (blue dot) and profiles (yellow solid line) measured during the EGIG campaign in 64 is shown on the left panels.*

We compare our ice velocity maps with the measurements from the EGIG campaign along 4 profiles shown in Figure 6.3. For the two profiles close to the front, our studies are within -94±89 m/yr (profile 1) and -46±198 m/yr (profile 2) (Figure 6.3). Further upstream (profile 3 and 4), we find larger differences with an overestimation of ice flow of 277 m/yr (profile 3) and 260 m/yr (profile 4) (Figure 6.3). For all profiles, larger difference are found in the center part region, where the glacier flows at the highest rates. We also compare our study with measurements from [*Drygalski*, 1897]. We find that our velocity are on average 460 m/yr lower (Figure 6.4) than what was found in [*Drygalski*, 1897] meaning the glaciers was flowing at higher rates at that time.

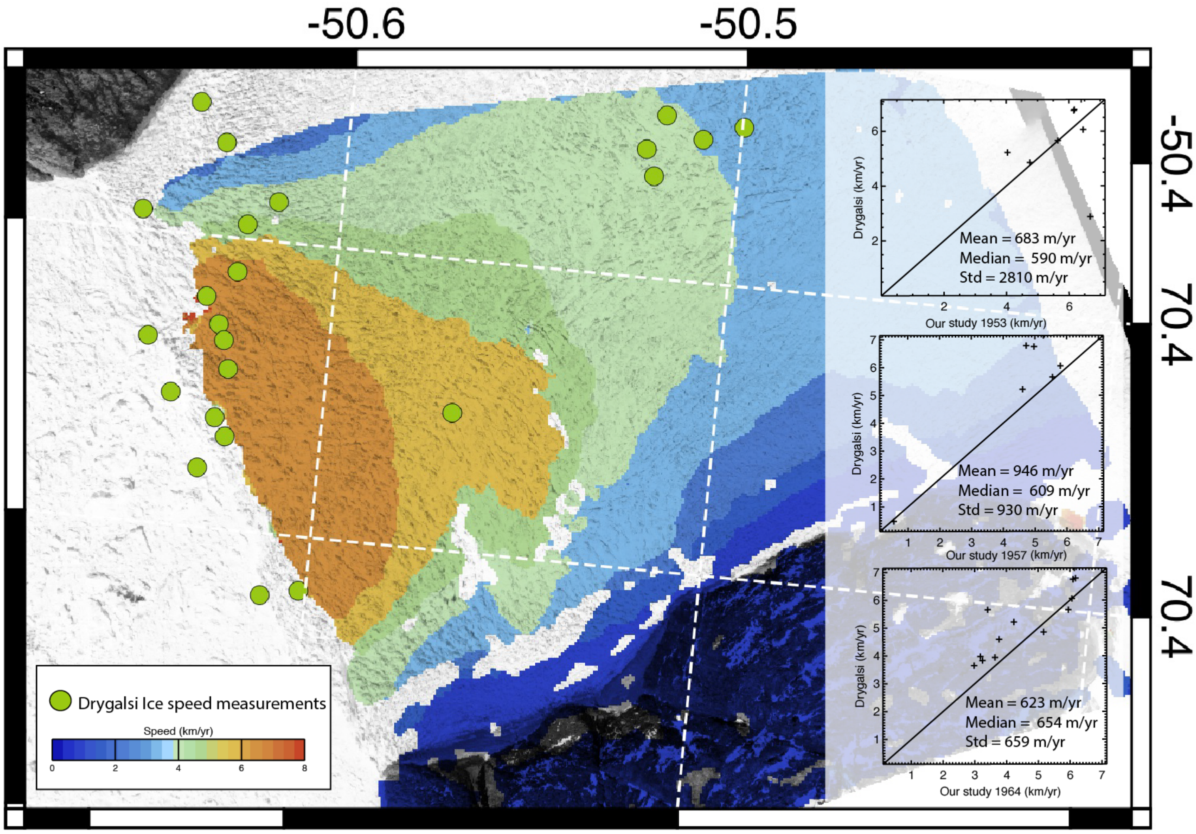

Figure 6.4: *Map showing the position of Drygalski's 1897 measurements (green dots) overlaid on our 1964 ice velocity maps. Ref:* **??**

In recent years, we observe that the temporal coverage gets denser as we get closer to present time due to the launch of numerous satellite missions (Figure 6.5). We observe a stable ice front velocity during the period 1990-present with an average of 5.7 km/yr, which is consistent with the 5.4 km/yr and 5.9 km/yr measured in 1953 and 1964 respectively. We note that this mean surface ice flow for the modern satellite period is also larger than the 4.7 km/yr ice velocity measured in 1957. For the period 2013-present, the constant acquisition of data every 6-days by Sentinel and every 14 days by Landsat-8 allow us to track infra-seasonal fluctuations in surface-ice flow. Between 2014 and 2017 we observe two distinct periods of dramatic decrease in flow rate. The first one started in late June 2014 and the ice flow decreased from 6 km/yr to 4.6 km/yr (Figure 6.5). The start of the second slow-down began in May 2016 (even though the signal is less clear), and we measure speed as low as 3 km/yr in July 2016, or a decrease by more than 50%. Such changes in surface ice flow behaviors, might be the same as the lower ice velocity observed in 1957. We note that similar pattern are likely driven by hydrology events and have been observed in seasonal surface mass change using GRACE data [*Schlegel et al.*, 2016].

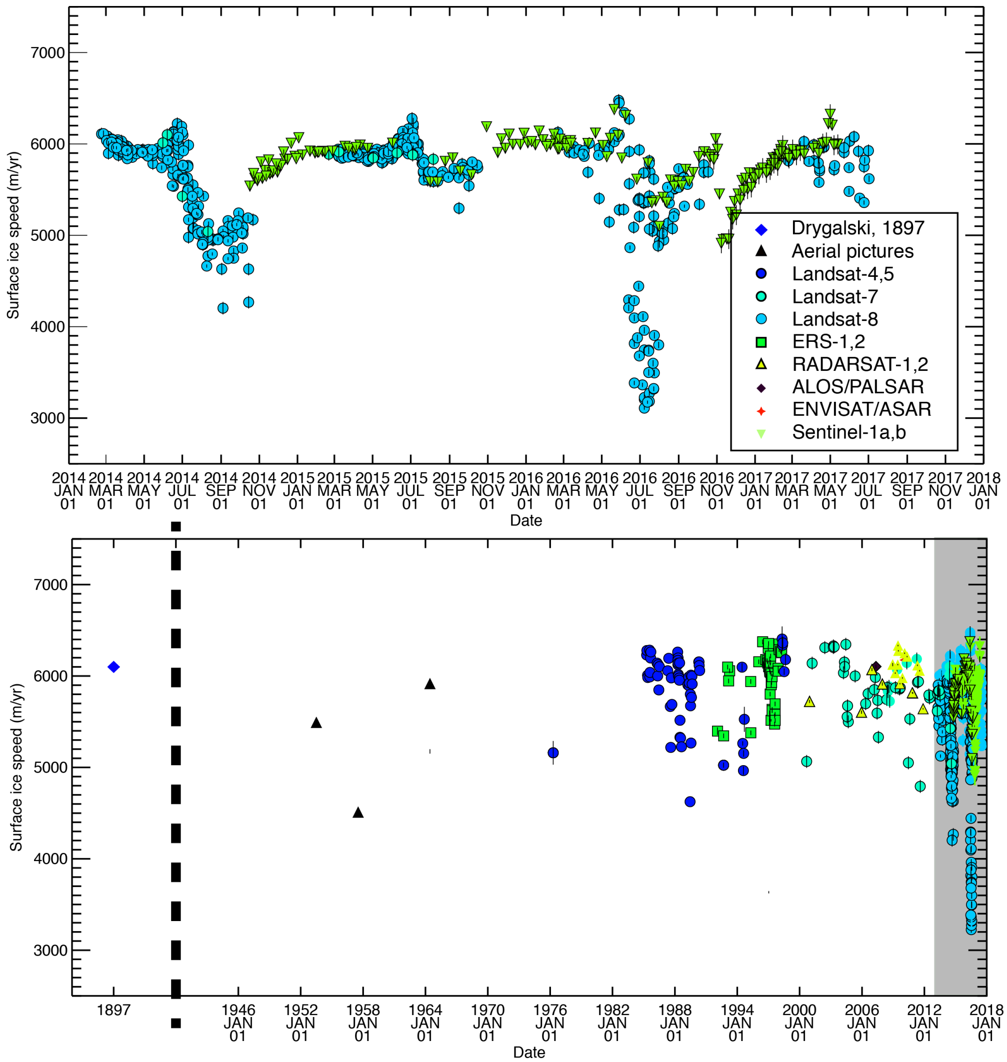

Figure 6.5: *Time series of ice velocities averaged over a sub-region of the ice front between 1953 and present. The upper panel is a zoom on the gray-shaded area.*

6.2 Mapping sub-ice shelf bathymetry of the Getz Ice shelf, West Antarctica

Using the expertise developed for the Amundsen Sea Embayment in Chapter 3, we started to expand our gravity inversion scheme to other regions of West Antarctica. We used free-air gravity anomalies from NASA's Operation Icebridge Campaign acquired between 2009 and 2016 above the main ice shelves along the Bakutis and Hobbs coast (Figure 6.7A). We divided the entire domain into three sub-regions with (1) Getz East (referred as Getz E.), (2) the main Getz Ice shelf, that down to the Wrigley Gulf (referred as Getz C.) and (3) Getz West along Hobbs coast (referred as Getz W.). The free-air gravity anomalies were upward continued to an elevation of 1,700 m above sea-level which is the maximum bed elevation of the grid.

The 3D model is the same as the one used in Chapter 3 for the Amundsen Sea Embayment. The initial bed combines the MC solution inland and IBCSO offshore. We merge the modeled and observed gravity by matching their mean value over overlapping regions between multibeam and gravity measurements. We allow for a 5-km wide transition boundary between the observed and modeled gravity. The inversion domain extends from the edges of the multibeam survey to the grounding line delineated from radar interferometry (Figure 6.7A). Because of the strong density gradient, we invert separately the small ice tongue flowing into Russell Bay and merge the result to the rest of the ice shelf. The inversion along the Hobbs Coast section is more challenging than the rest of the ice shelf because the DC-shift is not homogeneous everywhere. The changes in DC shift are likely due to changes in geology. Similarly as it was done for Pine Island glacier (Chapter 3), we use a minimum curvature interpolation scheme to map the variations in DC shift under the cavity and correct the gravity field for the variation in geology below the shelf.

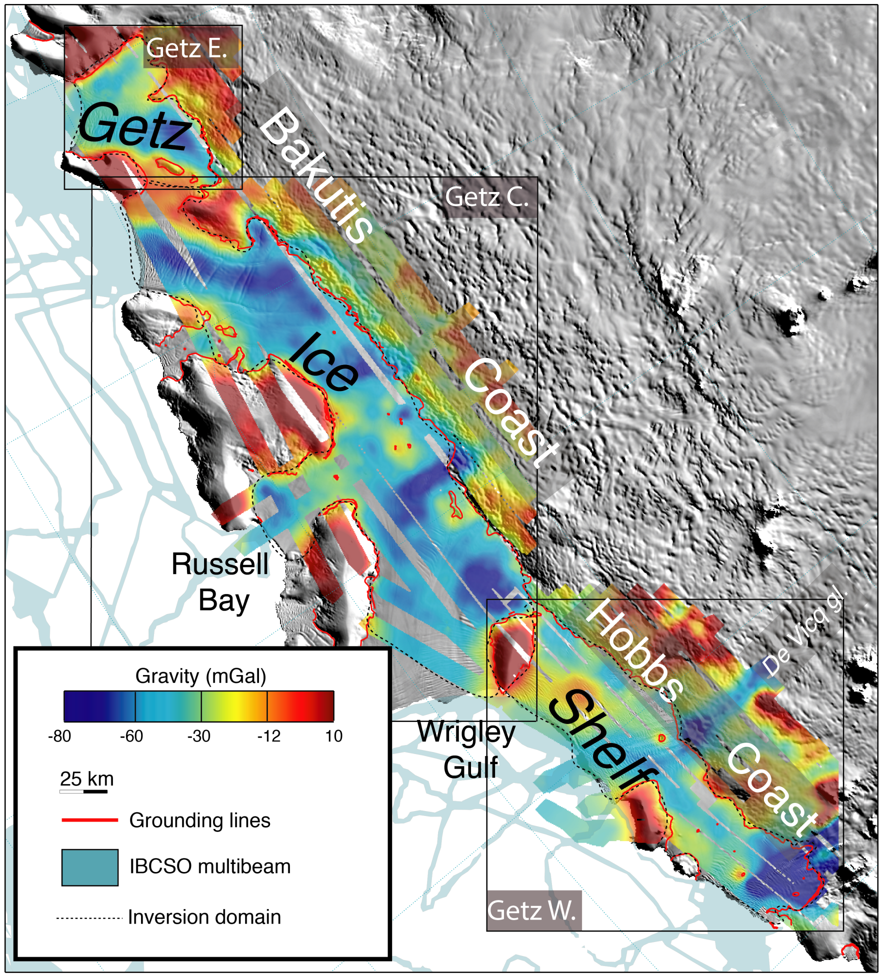

Figure 6.6: *Free-air gravity anomalies above the Getz Ice Shelf in West Antarctica overlaid on a MODIS mosaic of Antarctica from year 2004 on a grey scale. Areas mapped with multi beam echo sounding (MBES) are light grey. Glacier grounding lines from year 1996 are red. The limits of the gravity inversions are thin black dash lines within each black box.*

We present here preliminary results of the inversion along the coast of Bakutis. We find a steep transition between the ice shelf and the grounded ice all along the grounding line, with a bed shallowing from -800 m in some areas to -400 m inland. We note that this gradient is strongly present in the free-air gravity anomalies (Figure 6.6A), with a gravity varying from <-70 mGal to ∼-20mGal, hence this steep transition is not an artifact. Below Getz E., the deepest part of the sub-ice shelf cavity is located in front of the western part of the grounding line (Figure 6.7), a feature that is also observed in the gravity anomalies (Figure 6.6A). A sharp gradient at the eastern grounding line transition is however not observed in the gravity observations. This is likely due to the bedrock topography inland, where the mass-conservation reconstruction stops more than 20-km from the grounding line. Same observations can be made for the eastern part of Getz C. where the last 10-15 km between MC and the grounding line is from a kriging interpolation. In the central section of Getz C., half of the width is crossed by a ridge that is on average 800 below sea level.

Along the Hobbs Coast, our calculation reveals a cavity deeper than 800-m below sea level, east of De Vicq glacier. The channel is connected to the western part of the ice shelf by a 600 m deep trough that deepen to 800-m deep out of the cavity. Getz C. and Getz W are separated by a shallow 400 m deep ridge, hence blocking warm water to circulate in between the two cavities (Figure 6.7).

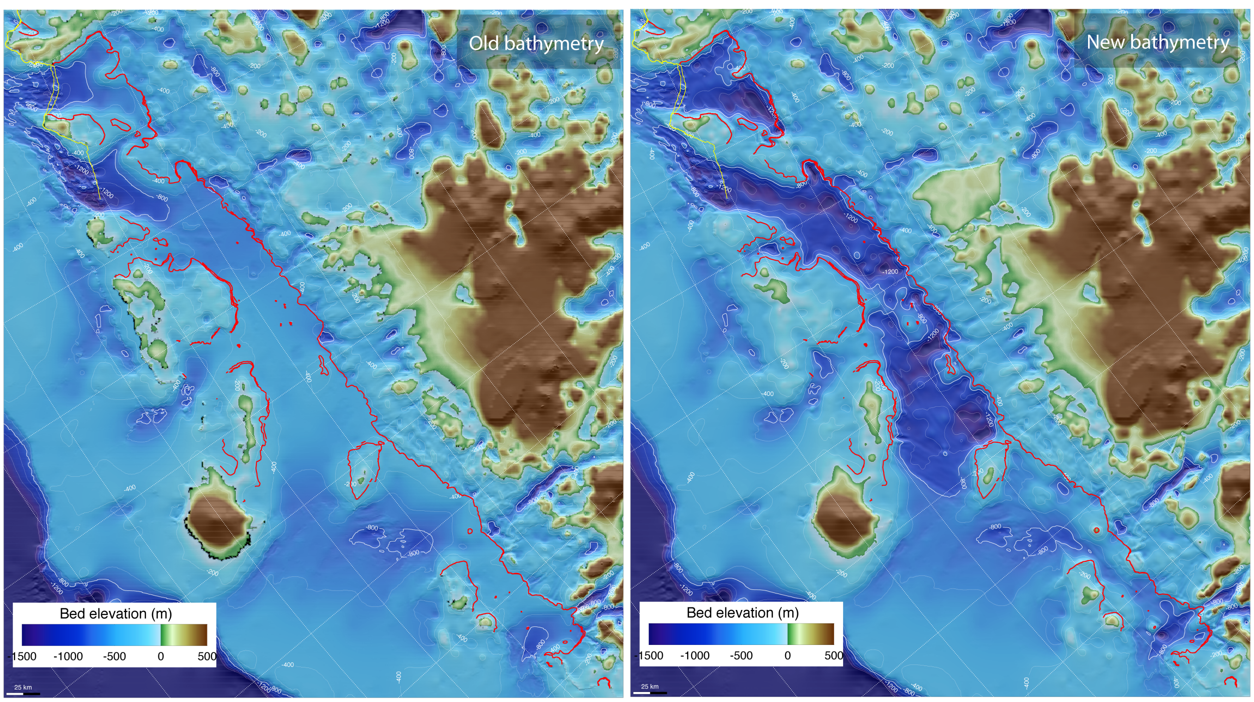

Figure 6.7: *(a) Old (RTOPO-2) and (b) New bathymetry (OIB gravity inversion) of the Getz Ice Shelf of West Antarctica. Bed elevation is color coded from brown/yellow and green (above sea level) to light blue and dark blue (-1,500 m), with contour lines every 200 m.*

6.3 Ice thickness of the central part of the South and North Patagonian Icefields, South America, from high-resolution airborne gravity and radar data.

6.3.1 Data and Methods

Gravity data In May and November 2012, we deployed the AIRGrav system in Patagonia, Chile for periods of 6 weeks on Eurocopter AS-350 B2 and B3 helicopters. In July 2016, we again used the AIRGrav on a fixed-wing aircraft for a period of 3 weeks. The survey area was divided between high-resolution (400-m) blocks over Glaciars San Rafael, Steffen, Colonia for NPI, and Jorge Montt and Occidental for SPI (Figure 6.8). The rest of the icefields was surveyed with a resolution of 1-km. NPI terrain varies from sea-level to 4,000 m, and terrain of SPI varies between sea-level and 3,600m (for the survey area). Adverse weather conditions prevented the survey of San Quíntin (NPI) and Greve (SPI). The traverse line spacing was 400 m, with a control line spacing of 2,000 m with a target speed of 50 knots on the glaciers and 60 knots on the plateaus. All 21 flights were flown with a ground clearance of 80 m.

The gravity data survey and the gravity anomaly processing were made by SGL (Sander Geophysics Limited). AIRGrav is an inertially referenced gravimeter that uses a Schuler tuned inertial platform that supports three orthogonal accelerometers. Accelerometer data are recorded at 128 Hz and later decimated to 2 Hz in processing. AIRGrav delivers gravity data with a noise level better than 0.5 mGal with a half sine wave ground resolution of 2 km [*Studinger et al.*, 2004]. The comparative navigation data supplied during all production flights allows for post-processed differential GPS corrections for every survey flight. The helicopter carried a Riegl LD90-31K-HiP Laser Rangefinder, with a range of 1500 m, an accuracy of 5 cm and a data rate of 3.3 Hz. The gravity data were processed into free-air gravity anomaly after Eotvos, normal gravity, free air, static, and level corrections. Statistical noise was reduced using a 20-sec filter on the glacier data and 28 sec on the plateaus. An analysis of cross-over lines indicated a noise level of 0.8 to 1.4 mGal, which is the expected nominal precision of AIRGrav. The glacier data lines acquired were filtered with a 20s half-wavelength low-pass time filter, gridded and low-pass filtered using a1,250-m half-wavelength.

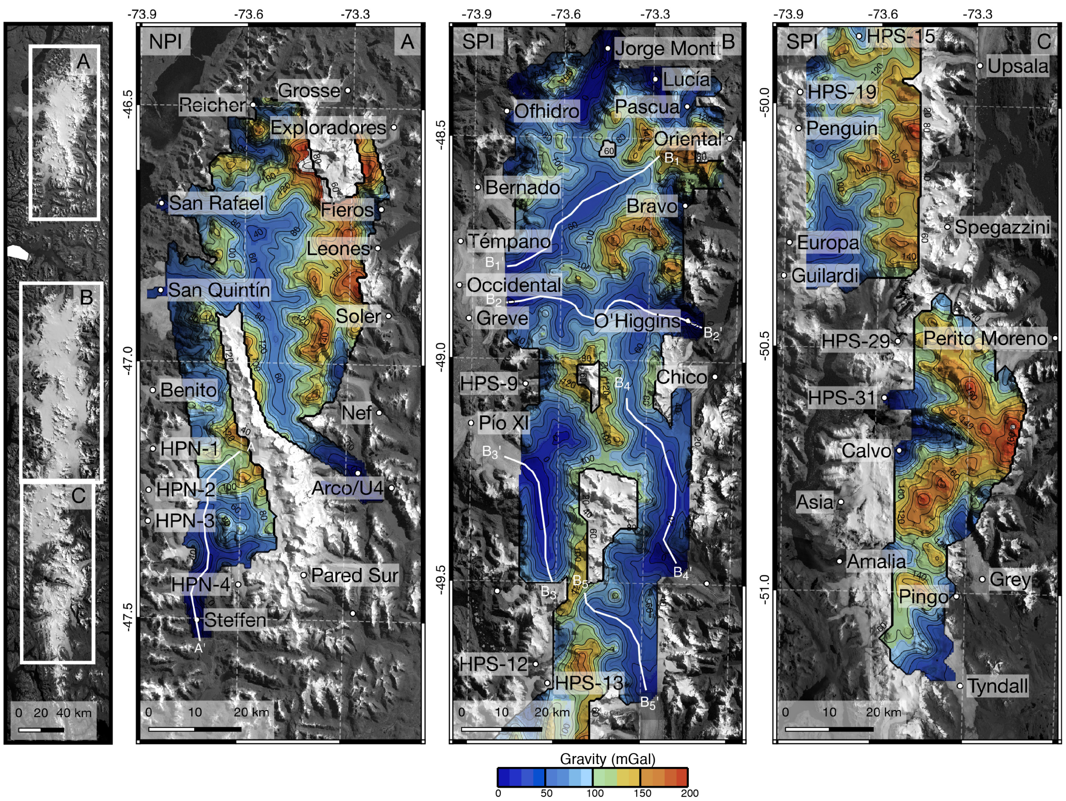

Figure 6.8: *Free-air gravity anomalies for the Northern Patagonian ice field (A) and Southern Patagonian icefield (B, C).*

Radar depth sounder The WISE instrument sounds the surface of the icefield by emitting a monochromatic pulse of one microsecond, which is called *tone* mode. We extract the surface location under the aircraft, using the aircraft location and a Digital Elevation model from SRTM V4. With those information, we convert the propagation time into distance using the speed of propagation of the radar signal through air and ice. We then compute a simulation of the echogram as if there was only reflection from the ice field surface and mountains on the sides. This simulated echogram is compared with the measured echogram to identify reliable echoes coming from the bedrock (and not from the sides). The bedrock elevation are digitized manually and classified with a quality flag for each echograms that varies depending on the uncertainty in the identification of the bed (Q0= ±100m, Q1= ±50m and Q2= ±25) (see Figure 6.9).

Bathymetry We used bathymetry data from [*Rivera et al.*, 2012] that were collected using a FURUNO sonar system, along with a Datasonic Bubble Pulser sub-bottom profiler. In front of Lake O'Higgins, we used data from [*Casassa et al.*, 1997], that were measured using a parametrical echo sounder (Innomar) in 2004 and 2005. Finally, we integrate bathymetry data from [*Koppes et al.*, 2010] in Laguna San Rafael from a zodiac using a Datasonics Bubble Pulser combined with a Lowrance 18-C depth sounder. These bathymetry data will be compared to the bedrock from radar and gravity inversion result.

Gravity inversion We form a three-dimensional model of NPI and SPI using the Geosoft GMSYS-3D software package which implements Parker's (1973) method. The 3D model include three layers with the following densities: 0.917 g/cm^3 for ice, 1.028 g/cm^3 for water, and a rock density from 2.5 to 3.0 g/cm^3. The surface of the ice field is determined using the laser altimeter which was onboard the 2012 campaign with a sub-meter precision. In areas where we have data gaps in the observations (ice, ground, water), we used a combination of a TanDEM-X DEM from 2015 (10 m resolution, over ice areas) and SRTM from 2000 at 30m horizontal resolution. All gravity data were upward continued to 3,500 m on NPI and 3,240 m on SPI, i.e. the highest flight elevation of the surveyed area. The first guess bedrock elevation was obtained using a linear correlation between radar data from WISE and gravity anomaly. During the inversion process, the modeled gravity from the first guess modeled is compared to observed gravity. The first guess layer is modified iteratively until we have an average difference of less than 0.1 mGal with the observation.

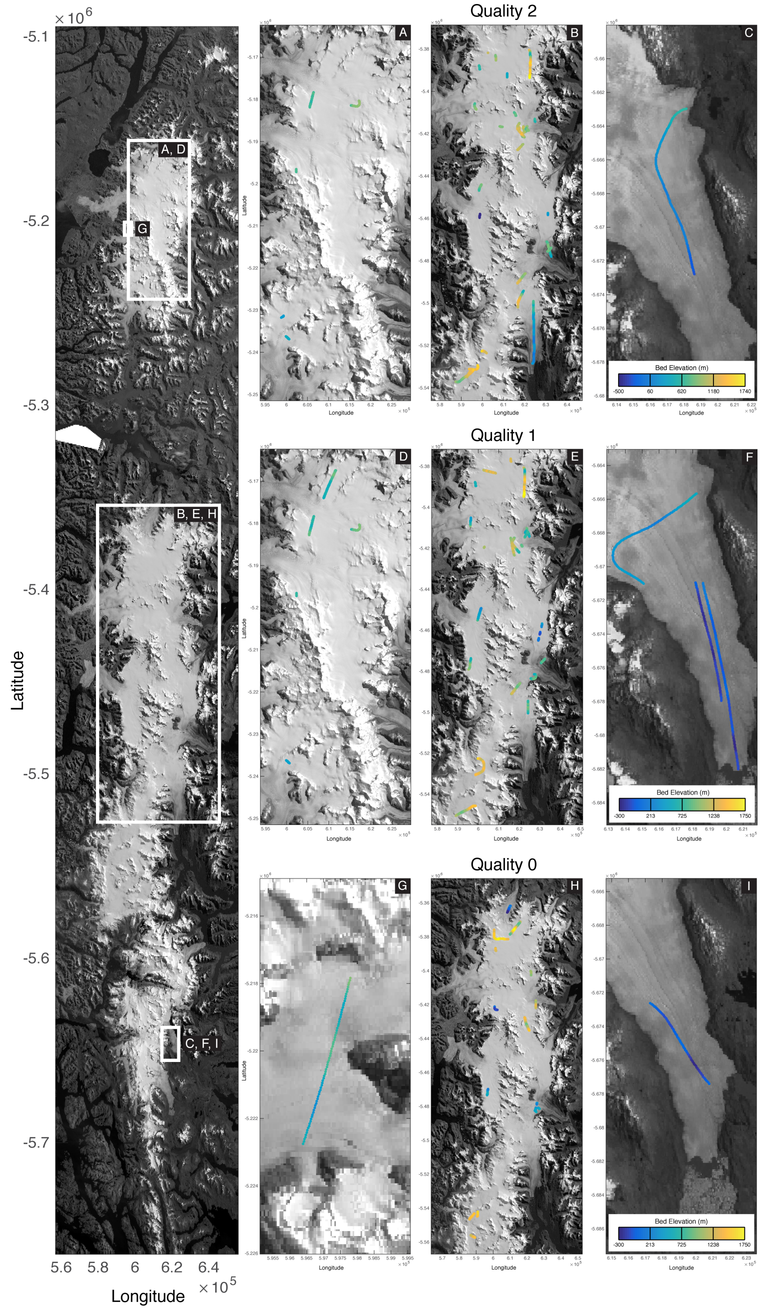

Figure 6.9: *Radar depth sounder profiles for the different quality over the Northern and Southern Patagonian Icefields.*

In order to adjust our first guess model to the observed gravity anomaly grid, we calculated the mean difference between the two grids (DC-shift) on ice free areas. Unlike previous studies, we found the DC Shift associated to each point where there is no ice and where there is gravity anomaly measurements. For a selected bedrock density, we do a set of inversions with a large number of DC-shift values (covering 130 mGal interval). For each inversions, we calculate the difference between the surface and the bedrock and choose the inversion that minimizes the difference on ice free areas. The DC-shift grid is then interpolated over the ice field using a weighting average method (radius of 10-km) and low-pass filtered to remove artifacts. We used a 40-km low pass filter for SPI and 25-km for NPI (size of the filter is a function of the average size of data gaps in both SPI and NPI).

6.3.2 Results

The bed elevation and ice thickness of NPI and SPI are shown in Fig. 2 with an intrinsic resolution of 750-m for the glacier troughs and 1 km for the plateau. The average misfit was reduced from -15.4 mGal (before the inversion) to 1.9 mGal (after the inversion). This translates into an uncertainty of ∼30m, using a translation factor of 5.8 mGal per 100 meters.

We complete the mapping of bedrock topography in NPI, by filling data gaps in the South Western part of the ice field from previous mapping from [*Gourlet et al.*, 2016]. In this region, the ice thickness exceeds 1000-m on the plateau. In the southwest part of the NPI, the inversion reveals two troughs running north-south and east-west that merge to form the main trunk of Steffen glacier (Fig. 6.10D). Ice velocities from [*Mouginot and Rignot*, 2014], 2014 indicates that the ice flows from the interior and reaches 500-m/yr at the front of Steffen glacier where ice is estimated to reach a thickness of 400-m.

In SPI, our study extends from Jorge Montt in the north to the southern tip of the ice field, with Tyndall glacier (Fig 6.10). This significantly extends previous mapping from [*Gourlet et al.*, 2016] that was limited to latitudes between -49^{o}S and -48.5^{o}S. The results highlights five notable troughs in the northern section of the SPI ice field denoted by the profiles B1-B5 (Fig. 6.10B). The largest glacial valleys are observed between Témplane and Oriental glacier and between Occidental and O'Higgings, where ice thickness can be greater 1600 m (Fig. 6.10E). Along B1-B1', ice is the thickest in the center of the profile where the thickness is greater than 1600 m. Between Occidental and O'Higgings, we note two ice streams that flows toward the east (O'Higgins) and west Occidental) part of the icefield. In the west, the ice thickness reaches 1200-m and is greater than 1000-m in the east (Fig

The ice surface between B3-B3' is relatively flat and the inversion reveals a deep bed with elevations varying between -50 m and 25 m on average, with ice thickness greater than 1200-m in the deepest parts. Another really deep trough is found between Chico and Viedma glaciers, with ice thickness that reaches more than 1300-m thick. Finally, the last deep trough is found in along the HPS-13 glacial valley, with a trough on average 800-m thick. The southern part of the SPI is constituted in majority of smaller mountain glaciers. The ice thickness in this area rarely exceeds 500-m except for Tyndall glacier, the last largest glacier at the southern tip of the SPI.

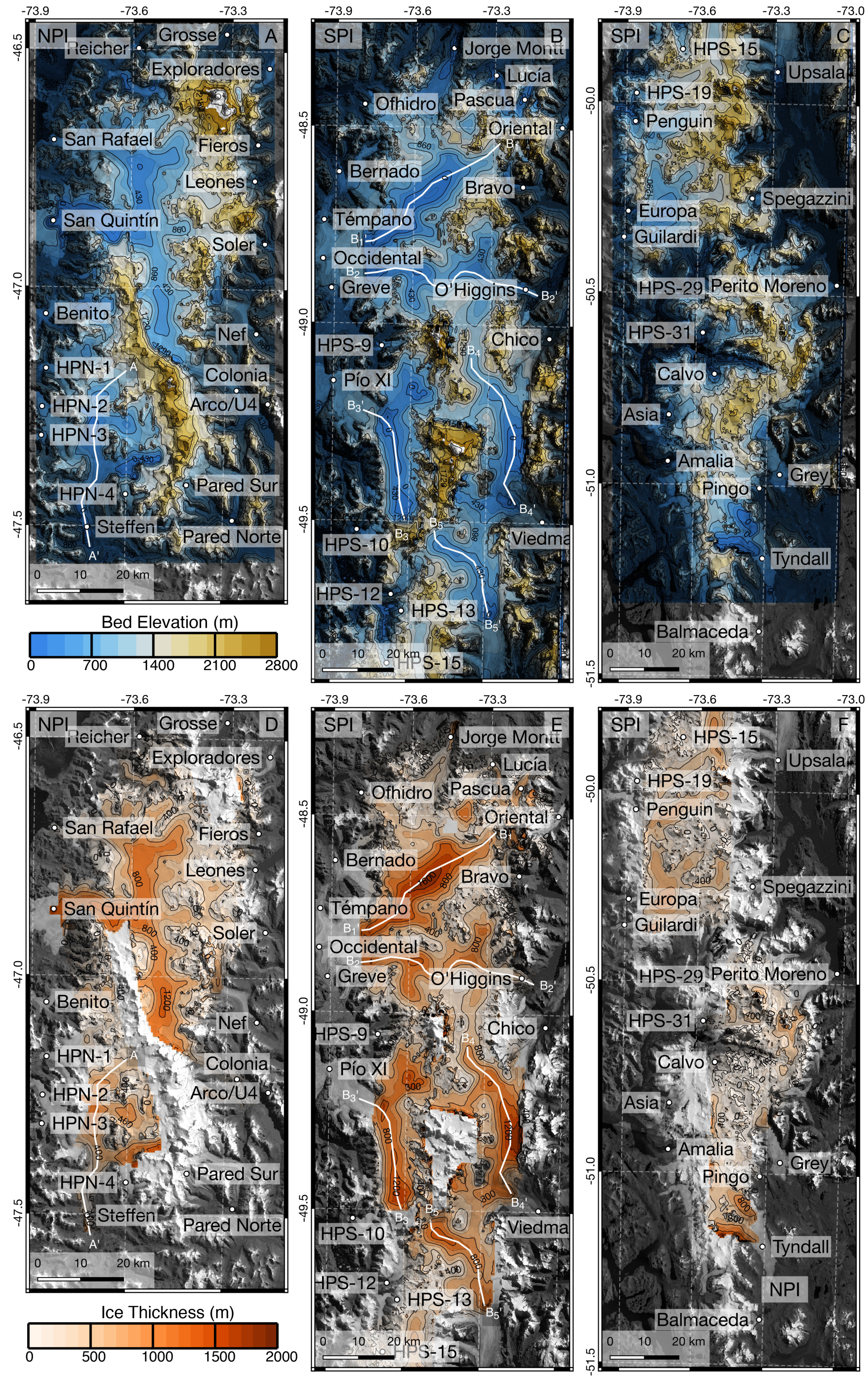

Figure 6.10: *Bed elevation in meters above sea-level and ice-thickness in meters for the Northern Patagonian Icefield (A, D), Southern Patagonian Icefield (B, C, E, F).*

Bibliography

Abdalati, W., et al., Outlet glacier and margin elevation changes: Near coastal thinning of the Greenland ice Sheet, *Journal of Geophysical Research*, *106*, 33, 729–33,741, 2001.

An, L., E. Rignot, S. Elieff, M. Morlighem, R. Millan, J. Mouginot, D. M. Holland, D. Holland, and J. Paden, Bed elevation of Jakobshavn Isbrae, West Greenland, from high-resolution airborne gravity and other data, *Geophysical Research Letters*, *44*, 3728–3736, 2017.

Andersen, M., et al., Basin-scale partitioning of Greenland ice sheet mass balance components (20072011), *Earth and Planetary Science Letters*, *409*, 89–95, 2015.

Arndt, J. E., et al., The International Bathymetric Chart of the Southern Ocean (IBCSO) Version 1.0-A new bathymetric compilation covering circum-Antarctic waters, *Geophysical Research Letters*, *40*, 3111–3117, 2013.

Bartholomaus, T. C., C. F. Larsen, and S. ONeel, Does calving matter? Evidence for significant submarine melt, *Earth and Planetary Science Letters*, *380*, 21–30, 2013.

Baudry, N., M. Diament, and Y. Albouy, Precise location of unsurveyed seamounts in the Austral archipelago area using SEASAT data, *Geophysical Journal International*, *89*, 869–888, 1987.

Bauer, A., Missions aeriennes de reconnaissance au Groenland 1957-1958, *Medd. Gronl.*, *173*, 1968.

Bjørk, A. A., K. H. Kjaer, N. J. Korsgaard, S. A. Khan, K. K. Kjeldsen, C. S. Andresen, J. E. Box, N. K. Larsen, and S. Funder, An aerial view of 80 years of climate-related glacier fluctuations in southeast Greenland, *Nature Geoscience*, *5*, 427–432, 2012.

Boghosian, A., K. Tinto, J. R. Cochran, D. Porter, S. Elieff, B. L. Burton, and R. E. Bell, Resolving bathymetry from airborne gravity along Greenland fjords, *Journal of Geophysical Research: Solid Earth*, *120*, 8516–8533, 2015.

Buch, E., and Meteorologisk Institut, *Present oceanographic conditions in Greenland waters*, Danish Meteorological Institute, Copenhagen, 2002, oCLC: 464824664.

Burgess, E. W., R. R. Forster, and C. F. Larsen, Flow velocities of Alaskan glaciers, *Nature Communications*, *4*, 2013.

Campbell, J. B., and R. H. Wynne, *Introduction to remote sensing*, 5th ed ed., Guilford Press, New York, 2011.

Carbonnell, M., and A. Bauer, Exploitation des couvertures photographiques aeriennes répetées du front des glaciers vêlant dans Disko Bugt et Umanak Fjord, juin-juillet, 1964, *Medd. Gronl.*, *173*, 1968.

Casassa, G., H. Brecher, A. Rivera, and M. Aniya, A century-long recession record of glaciar ohiggins, chilean patagonia, *Annals of Glaciology*, *24*, 106110, 1997.

Christoffersen, P., R. I. Mugford, K. J. Heywood, I. Joughin, J. A. Dowdeswell, J. P. M. Syvitski, A. Luckman, and T. J. Benham, Warming of waters in an East Greenland fjord prior to glacier retreat: mechanisms and connection to large-scale atmospheric conditions, *The Cryosphere*, *5*, 701–714, 2011.

Church, J. A., et al., Revisiting the Earth's sea-level and energy budgets from 1961 to 2008, *Geophysical Research Letters*, *38*, n/a–n/a, 2011.

Cochran, J. R., and R. E. Bell, Icebridge sander airgrav l1b geolocated free air gravity anomalies, nasa distributed active archive, *Natl. Snow and Ice Data Cent., Boulder, Col, [Digital Media], updated 2014*, 2010.

Cochran, J. R., and R. E. Bell, Inversion of IceBridge gravity data for continental shelf bathymetry beneath the Larsen Ice Shelf, Antarctica, *Journal of Glaciology*, *58*, 540–552, 2012.

Cochran, J. R., and M. Talwani, Free-air gravity anomalies in the world's oceans and their relationship to residual elevation, *Geophysical Journal International*, *50*, 495–552, 1977.

Colgan, W., W. Abdalati, M. Citterio, B. Csatho, X. Fettweis, S. Luthcke, G. Moholdt, S. B. Simonsen, and M. Stober, Hybrid glacier Inventory, Gravimetry and Altimetry (HIGA) mass balance product for Greenland and the Canadian Arctic, *Remote Sensing of Environment*, *168*, 24–39, 2015.

Copland, L., M. J. Sharp, and J. A. Dowdeswell, The distribution and flow characteristics of surge-type glaciers in the Canadian High Arctic, *Ann. Glaciol*, *36*, 73–81, 2003.

Cuffey, K., *The physics of glaciers*, 4th ed ed., Butterworth-Heinemann/Elsevier, Burlington, MA, 2010.

Damiani, T. M., T. A. Jordan, F. Ferraccioli, D. A. Young, and D. D. Blankenship, Variable crustal thickness beneath Thwaites Glacier revealed from airborne gravimetry, possible implications for geothermal heat flux in West Antarctica, *Earth and Planetary Science Letters*, *407*, 109–122, 2014.

Dehecq, A., N. Gourmelen, and E. Trouve, Deriving large-scale glacier velocities from a complete satellite archive: Application to the Pamir-Karakoram-Himalaya, *Remote Sensing of Environment*, *162*, 55–66, 2015.

Drygalski, E. V., *Dr Von Drygalski's Greenland Expedition 1891-1893*, Berlin, Berlin, 1897.

Dutrieux, P., et al., Strong Sensitivity of Pine Island Ice-Shelf Melting to Climatic Variability, *Science*, *343*, 174–178, 2014.

Enderlin, E. M., I. M. Howat, S. Jeong, M.-J. Noh, J. H. van Angelen, and M. R. van den Broeke, An improved mass budget for the Greenland ice sheet, *Geophysical Research Letters*, *41*, 866–872, 2014.

Ettema, J., M. R. van den Broeke, E. van Meijgaard, W. J. van de Berg, J. L. Bamber, J. E. Box, and R. C. Bales, Higher surface mass balance of the Greenland ice sheet revealed by high-resolution climate modeling, *Geophysical Research Letters*, *36*, 2009.

Favier, L., G. Durand, S. L. Cornford, G. H. Gudmundsson, O. Gagliardini, F. Gillet-Chaulet, T. Zwinger, A. J. Payne, and A. M. Le Brocq, Retreat of Pine Island Glacier controlled by marine ice-sheet instability, *Nature Climate Change*, *4*, 117–121, 2014.

Fretwell, P., et al., Bedmap2: improved ice bed, surface and thickness datasets for Antarctica, *The Cryosphere*, *7*, 375–393, 2013.

Gardner, A. S., G. Moholdt, B. Wouters, G. J. Wolken, D. O. Burgess, M. J. Sharp, J. G. Cogley, C. Braun, and C. Labine, Sharply increased mass loss from glaciers and ice caps in the Canadian Arctic Archipelago, *Nature*, *473*, 357–360, 2011.

Goldstein, R., Satellite Radar Interferometry for Monitoring Ice Sheet Motion: Application to an Antarctic Ice Stream, *Science*, *262*, 1525–1530, 1993.

Gourlet, P., E. Rignot, A. Rivera, and G. Casassa, Ice thickness of the northern half of the Patagonia Icefields of South America from high-resolution airborne gravity surveys, *Geophysical Research Letters*, *43*, 241–249, 2016.

Gray, L., and K. Mattar, Influence of Ionospheric Electron Density Fluctuations on Satellite Radar Interferometry, *Geophys. Res. Lett.*, *27*, 1451–1454, 2000.

Gray, L., K. Mattar, and N. Short, Speckle Tracking for 2-Dimensional Ice Motion Studies in Polar Regions: Influence of the Ionosphere., *Fringes 99'*, 1999.

Henriksen, N., *Greenland from Archaean to Quaternary: descriptive text to the Geological map of Greenland 1: 2 500 000*, vol. 185, Geological Survey of Denmark, 2009.

Holt, J. W., D. D. Blankenship, D. L. Morse, D. A. Young, M. E. Peters, S. D. Kempf, T. G. Richter, D. G. Vaughan, and H. F. J. Corr, New boundary conditions for the West Antarctic Ice Sheet: Subglacial topography of the Thwaites and Smith glacier catchments, *Geophysical Research Letters*, *33*, 2006.

Howat, I. M., I. Joughin, M. Fahnestock, B. E. Smith, and T. A. Scambos, Synchronous retreat and acceleration of southeast Greenland outlet glaciers 200006: Ice dynamics and coupling to climate, *Journal of Glaciology*, *54*, 646–660, 2008.

Howat, I. M., A. Negrete, and B. E. Smith, The Greenland Ice Mapping Project (GIMP) land classification and surface elevation data sets, *The Cryosphere*, *8*, 1509–1518, 2014.

Hughes, T. J., The weak underbelly of the West Antarctic ice-sheet, *Journal of Glaciology*, 1981.

Hutter, K., Dynamics of glaciers and large ice masses, *Annual Review of Fluid Mechanics*, *14*, 87–130, 1982.

Jacobs, S., A. Jenkins, H. Hellmer, C. Giulivi, F. Nitsche, B. Huber, and R. Guerrero, The Amundsen Sea and the Antarctic Ice Sheet, *Oceanography*, *25*, 154–163, 2012.

Jacobs, S., C. Giulivi, P. Dutrieux, E. Rignot, F. Nitsche, and J. Mouginot, Getz Ice Shelf melting response to changes in ocean forcing, *Journal of Geophysical Research: Oceans*, *118*, 4152–4168, 2013.

Jacobs, S. S., A. Jenkins, C. F. Giulivi, and P. Dutrieux, Stronger ocean circulation and increased melting under Pine Island Glacier ice shelf, *Nature Geoscience*, *4*, 519–523, 2011.

Jenkins, A., P. Dutrieux, S. S. Jacobs, S. D. McPhail, J. R. Perrett, A. T. Webb, and D. White, Observations beneath Pine Island Glacier in West Antarctica and implications for its retreat, *Nature Geoscience*, *3*, 468–472, 2010.

Jiskoot, H., D. Juhlin, H. St Pierre, and M. Citterio, Tidewater glacier fluctuations in central East Greenland coastal and fjord regions (1980s2005), *Annals of Glaciology*, *53*, 35–44, 2012.

Joughin, I., M. Fahnestock, S. Ekholm, and R. Kwok, Balance velocities of the Greenland ice sheet, *Geophysical Research Letters*, *24*, 3045–3048, 1997.

Joughin, I., W. Abdalati, and M. Fahnestock, Large fluctuations in speed on Greenland's Jakobshavn Isbr glacier, *Nature*, *432*, 608–610, 2004.

Joughin, I., B. E. Smith, and W. Abdalati, Glaciological advances made with interferometric synthetic aperture radar, *Journal of Glaciology*, *56*, 1026–1042, 2010.

Joughin, I., D. E. Shean, B. E. Smith, and P. Dutrieux, Grounding line variability and subglacial lake drainage on Pine Island Glacier, Antarctica, *Geophysical Research Letters*, *43*, 9093–9102, 2016.

Khan, S. A., et al., Sustained mass loss of the northeast Greenland ice sheet triggered by regional warming, *Nature Climate Change*, *4*, 292–299, 2014.

Koppes, M., R. Sylwester, A. Rivera, and B. Hallet, Variations in Sediment yield Over the Advance and Retreat of a Calving Glacier, Laguna San Rafael, North Patagonian Icefield, *Quaternary Research*, *73*, 84–95, 2010.

Korsgaard, N. J., C. Nuth, S. A. Khan, K. K. Kjeldsen, A. A. Bjørk, A. Schomacker, and K. H. Kjaer, Digital elevation model and orthophotographs of Greenland based on aerial photographs from 19781987, *Scientific Data*, *3*, 160,032, 2016.

Krabill, W., E. Arnold, S. Manizade, C. Martin, J. Sonntag, R. Swift, R. Thomas, W. Wright, and J. Yungel, Rapid Thinning of Parts of the Southern Greenland Ice Sheet, *Science*, *283*, 1522–1524, 1999.

Larsen, C. F., E. Burgess, A. A. Arendt, S. O'Neel, A. J. Johnson, and C. Kienholz, Surface melt dominates Alaska glacier mass balance: Alaska Glacier Mass Balance, *Geophysical Research Letters*, *42*, 5902–5908, 2015.

Lenaerts, J. T. M., J. H. van Angelen, M. R. van den Broeke, A. S. Gardner, B. Wouters, and E. van Meijgaard, Irreversible mass loss of Canadian Arctic Archipelago glaciers, *Geophysical Research Letters*, *40*, 870–874, 2013.

Leuschen, C., G. P., R. F., P. J., and A. C., Icebridge mcords l2 ice thickness, 2010.

Lowe, A., and J. Anderson, Evidence for abundant subglacial meltwater beneath the paleo-ice sheet in Pine Island Bay, Antarctica, *J. Glac.*, *49*, 125–138, 2003.

Lubin, D., and R. Massom, *Polar remote sensing*, 1st ed ed., Springer, Berlin : New York, 2005.

Mayol, L., Identification of unstable glaciers intermediate between normal and surging glaciers, *Mater. Glyatsiol. Issled*, *133*, 133–135, 1978.

Michel, R., and E. Rignot, Flow of Glaciar Moreno, Argentina, frotn repeat-pass ShuttleImaging Radar images: comparison of the phase correlationmethod with radar interferometry, *International Glaciological Society*, *45*, 93–100, 1999.

Millan, R., E. Rignot, V. Bernier, M. Morlighem, and P. Dutrieux, Bathymetry of the Amundsen Sea Embayment sector of West Antarctica from Operation IceBridge gravity and other data, *Geophysical Research Letters*, *44*, 1360–1368, 2017.

Mige, C., et al., Spatial extent and temporal variability of Greenland firn aquifers detected by ground and airborne radars: Greenland Firn Aquifers, *Journal of Geophysical Research: Earth Surface*, *121*, 2381–2398, 2016.

Moon, T., I. Joughin, B. Smith, M. R. van den Broeke, W. J. van de Berg, B. Nol, and M. Usher, Distinct patterns of seasonal Greenland glacier velocity: Seasonal velocity, *Geophysical Research Letters*, *41*, 7209–7216, 2014.

Morlighem, M., E. Rignot, H. Seroussi, E. Larour, H. Ben Dhia, and D. Aubry, A mass conservation approach for mapping glacier ice thickness, *Geophysical Research Letters*, *38*, n/a–n/a, 2011.

Morlighem, M., E. Rignot, J. Mouginot, H. Seroussi, and E. Larour, Deeply incised submarine glacial valleys beneath the Greenland ice sheet, *Nature Geoscience*, *7*, 418–422, 2014.

Morlighem, M., et al., BedMachine v3: Complete Bed Topography and Ocean Bathymetry Mapping of Greenland From Multibeam Echo Sounding Combined With Mass Conservation, *Geophysical Research Letters*, *44*, 11,051–11,061, 2017.

Motyka, R. J., L. Hunter, K. A. Echelmeyer, and C. Connor, Submarine melting at the terminus of a temperate tidewater glacier, LeConte Glacier, Alaska, USA, *Annals of Glaciology*, *36*, 57–65, 2003.

Mouginot, J., and E. Rignot, Ice motion of the patagonian icefields of south america: 19842014, *Geophysical Research Letters*, *42*, 1441–1449, 2014.

Mouginot, J., and E. Rignot, Ice motion of the Patagonian Icefields of South America: 1984-2014, *Geophysical Research Letters*, *42*, 1441–1449, 2015.

Mouginot, J., B. Scheuchl, and E. Rignot, Mapping of Ice Motion in Antarctica Using Synthetic-Aperture Radar Data, *Remote Sens.*, *4*, 2753–2767, 2012.

Mouginot, J., E. Rignot, B. Scheuchl, and R. Millan, Comprehensive Annual Ice Sheet Velocity Mapping Using Landsat-8, Sentinel-1, and RADARSAT-2 Data, *Remote Sensing*, *9*, 364, 2017.

Murray, T., et al., Ocean regulation hypothesis for glacier dynamics in southeast Greenland and implications for ice sheet mass changes, *Journal of Geophysical Research*, *115*, 2010.

Muto, A., S. Anandakrishnan, and R. B. Alley, Subglacial bathymetry and sediment layer distribution beneath the Pine Island Glacier ice shelf, West Antarctica, modeled using aerogravity and autonomous underwater vehicle data, *Annals of Glaciology*, *54*, 27–32, 2013.

Muto, A., L. E. Peters, K. Gohl, I. Sasgen, R. B. Alley, S. Anandakrishnan, and K. L. Riverman, Subglacial bathymetry and sediment distribution beneath Pine Island Glacier ice shelf modeled using aerogravity and in situ geophysical data: New results, *Earth and Planetary Science Letters*, *433*, 63–75, 2016.

Mnchow, A., K. Falkner, H. Melling, B. Rabe, and H. Johnson, Ocean Warming of Nares Strait Bottom Waters o Northwest Greenland, 20032009, *Oceanography*, *24*, 114–123, 2011.

Nilsson, J., L. Sandberg Srensen, V. R. Barletta, and R. Forsberg, Mass changes in Arctic ice caps and glaciers: implications of regionalizing elevation changes, *The Cryosphere*, *9*, 139–150, 2015.

Nitsche, F. O., S. S. Jacobs, R. D. Larter, and K. Gohl, Bathymetry of the Amundsen Sea continental shelf: Implications for geology, oceanography, and glaciology, *Geochemistry, Geophysics, Geosystems*, *8*, n/a–n/a, 2007.

Noel, B., W. J. van de Berg, H. Machguth, S. Lhermitte, I. Howat, X. Fettweis, and M. R. van den Broeke, A daily, 1 km resolution data set of downscaled Greenland ice sheet surface mass balance (19582015), *The Cryosphere*, *10*, 2361–2377, 2016.

O'Leary, M., and P. Christoffersen, Calving on tidewater glaciers amplified by submarine frontal melting, *The Cryosphere*, *7*, 119–128, 2013.

Overeem, I., B. D. Hudson, J. P. M. Syvitski, A. B. Mikkelsen, B. Hasholt, M. R. van den Broeke, B. P. Y. Nol, and M. Morlighem, Substantial export of suspended sediment to the global oceans from glacial erosion in Greenland, *Nature Geoscience*, *10*, 859–863, 2017.

P. Gogineni, CReSIS Radar Depth Sounder data, Lawrence, Kansas (USA: Digital Media), *Natl. Snow and Ice Data Cent.*, 2012.

Parizek, B. R., et al., Dynamic (in)stability of Thwaites Glacier, West Antarctica, *Journal of Geophysical Research: Earth Surface*, *118*, 638–655, 2013.

Parker, R. L., The rapid calculation of potential anomalies, *Geophysical Journal International*, *31*, 447–455, 1973.

Pechnig, R., H. Delius, and A. Bartetzko, Effect of compositional variations on log responses of igneous and metamorphic rocks. II: acid and intermediate rocks, *Geological Society, London, Special Publications*, *240*, 279–300, 2005.

Pfeffer, W. T., et al., The Randolph Glacier Inventory: a globally complete inventory of glaciers, *Journal of Glaciology*, *60*, 537–552, 2014.

Raymond, C., How do glaciers surge?, *J. Geophys. Res.*, *92*, 9121–9134, 1987.

Riaz, S., A. Ali, and M. N. Baig, Increasing risk of glacial lake outburst floods as a consequence of climate change in the Himalayan region, *Jmb: Journal of Disaster Risk Studies*, *6*, 1–7, 2014.

Rignot, E., Changes in ice dynamics and mass balance of the Antarctic ice sheet, *Philosophical Transactions of the Royal Society A: Mathematical, Physical and Engineering Sciences*, *364*, 1637–1655, 2006.

Rignot, E., Changes in West Antarctic ice stream dynamics observed with ALOS PALSAR data, *Geophysical Research Letters*, *35*, n/a–n/a, 2008.

Rignot, E., and J. Mouginot, Ice flow in Greenland for the International Polar Year 2008-2009, *Geophysical Research Letters*, *39*, n/a–n/a, 2012.

Rignot, E., D. Braaten, S. P. Gogineni, W. B. Krabill, and J. R. McConnell, Rapid ice discharge from southeast Greenland glaciers, *Geophysical Research Letters*, *31*, n/a–n/a, 2004.

Rignot, E., J. E. Box, E. Burgess, and E. Hanna, Mass balance of the Greenland ice sheet from 1958 to 2007, *Geophysical Research Letters*, *35*, 2008.

Rignot, E., J. Mouginot, and B. Scheuchl, Antarctic grounding line mapping from differential satellite radar interferometry: grounding line of Antarctica, *Geophysical Research Letters*, *38*, n/a–n/a, 2011.

Rignot, E., S. Jacobs, J. Mouginot, and B. Scheuchl, Ice-Shelf Melting Around Antarctica, *Science*, *341*, 2013.

Rignot, E., J. Mouginot, M. Morlighem, H. Seroussi, and B. Scheuchl, Widespread, rapid grounding line retreat of Pine Island, Thwaites, Smith, and Kohler glaciers, West Antarctica, from 1992 to 2011, *Geophysical Research Letters*, *41*, 3502–3509, 2014.

Rignot, E., et al., Modeling of ocean-induced ice melt rates of five west Greenland glaciers over the past two decades, *Geophysical Research Letters*, *43*, 6374–6382, 2016.

Rivera, A., M. Koppes, C. Bravo, and J. C. Aravena, Little Ice Age advance and retreat of Glaciar Jorge Montt, Chilean Patagonia, *Climate of the Past*, *8*, 403–414, 2012.

Sandwell, D. T., D. Mller, W. Smith, E. Garcia, and R. Francis, New global marine gravity model from CryoSat-2 and Jason-1 reveals buried tectonic structure, *Marine Geophysics*, *346*, 65–67, 2014.

Scambos, T. A., M. J. Dutkiewicz, J. C. Wilson, and R. A. Bindschadler, Application of image cross-correlation to the measurement of glacier velocity using satellite image data, *Remote sensing of environment*, *42*, 177–186, 1992.

Schlegel, N.-J., D. N. Wiese, E. Y. Larour, M. M. Watkins, J. E. Box, X. Fettweis, and M. R. van den Broeke, Application of GRACE to the assessment of model-based estimates of monthly Greenland Ice Sheet mass balance (2003-2012), *The Cryosphere*, *10*, 1965–1989, 2016.

Short, N. H., and A. L. Gray, Glacier dynamics in the Canadian High Arctic from RADARSAT-1 speckle tracking, *Can. J. Remote Sensing*, *31*, 225–239, 2005.

Smith, W. H., and D. T. Sandwell, Conventional bathymetry, bathymetry from space, and geodetic altimetry, *Oceanography*, *17*, 8–23, 2004.

Studinger, M., R. E. Bell, and A. A. Tikku, Estimating the depth and shape of subglacial Lake Vostok's water cavity from aerogravity data, *Geophysical Research Letters*, *31*, n/a–n/a, 2004.

Studinger, M., L. Koenig, S. Martin, and J. Sonntag, Operation Icebridge : using instrumented aircraft to bridge the observational gap between ICESat and ICESat-2, in *IEEE Geoscience and Remote Sensing Letters*, pp. 1918–1919, 2010.

Tedesco, M., et al., Arctic Report Card Greenland Ice Sheet, *Tech. rep.*, Lamont Doherty Earth Observatory, 2015.

Thomas, R., Accelerated Sea-Level Rise from West Antarctica, *Science*, *306*, 255–258, 2004.

Tinto, K. J., and R. E. Bell, Progressive unpinning of Thwaites Glacier from newly identified offshore ridge: Constraints from aerogravity, *Geophysical Research Letters*, *38*, n/a–n/a, 2011.

Turrin, J. B., R. R. Forster, J. M. Sauber, D. K. Hall, and R. L. Bruhn, Effects of bedrock lithology and subglacial till on the motion of Ruth Glacier, Alaska, deduced from five pulses from 1973 to 2012, *Journal of Glaciology*, *60*, 771–781, 2014.

Van Wychen, W., L. Copland, L. Gray, D. Burgess, B. Danielson, and M. Sharp, Spatial and temporal variation of ice motion and ice flux from Devon Ice Cap, Nunavut, Canada, *J. Glaciol*, *58*, 657–664, 2012.

Van Wychen, W., D. O. Burgess, L. Gray, L. Copland, M. Sharp, J. A. Dowdeswell, and T. J. Benham, Glacier velocities and dynamic ice discharge from the Queen Elizabeth Islands, Nunavut, Canada, *Geophys. Res. Lett.*, *41*, 484–490, 2014.

Van Wychen, W., J. Davis, D. O. Burgess, L. Copland, L. Gray, M. Sharp, and C. Mortimer, Characterizing interannual variability of glacier dynamics and dynamic discharge (1999-2015) for the ice masses of Ellesmere and Axel Heiberg Islands, Nunavut, Canada, *J. Geophys. Res.*, *121*, 39–63, 2016.

Vaughan, D. G., I. Allison, P. Mote, E. Rignot, T. Zhang, A. A. Arendt, and J. Bamber, 4 Observations: Cryosphere, in *IPCC*, p. 66, 2013.

Vaughan, D. G., et al., New boundary conditions for the West Antarctic ice sheet: Subglacial topography beneath Pine Island Glacier, *Geophysical Research Letters*, *33*, 2006.

Weidick, A., Observations on some Holocene glacier fluctuations in West Greenland, *Bull. Gronl. Geol. Unders.*, *73*, 1968.

William, S., On determining the depth of the sea without the use of the sounding-line, and on an attraction-meter, *Proceedings of the Royal Society of London*, *24*, 317–321, 1876.

Willis, M. J., A. K. Melkonian, M. E. Pritchard, and A. Rivera, Ice loss from the Southern Patagonian Ice Field, South America, between 2000 and 2012, *Geophysical Research Letters*, *39*, n/a–n/a, 2012.

Appendix A

Supplementary Information for Chapter 2

We include 3 figures that describe the frontal position of near-stagnant and stagnant glaciers, yearly velocity mosaic, and satellite tracks positions.

- Figure A.1 displays the position of the satellite tracks processed in this study.

- Figure A.2 are 100-m-resolution mosaics of velocity derived from ERS-1, RADARSAT-1, ALOS/PALSAR, LANDSAT-7, LANDSAT-8 and Sentinel-1a.

- Figure A.3 represents the frontal position of near-stagnant and stagnant glaciers.

- Table A.1 summarizes the ice discharge of each glacier for each ice cap. In the first three columns, we list the ice cap names, glacier names and ice discharge methods. We list marine-terminating and land-terminating glacier area in km2 for each ice cap per the Randolph Glacier Inventory. Other columns includes the ice discharge and related errors from 1991 to 2015. Black values are measured. Grey values are linearly interpolated. Green values are extrapolated by taking the closest non-surging discharge value (associated to a conservative 100% error). For each ice cap, we list the total surveyed discharge and the total discharge after scaling of the remaining marine-terminating glaciers.

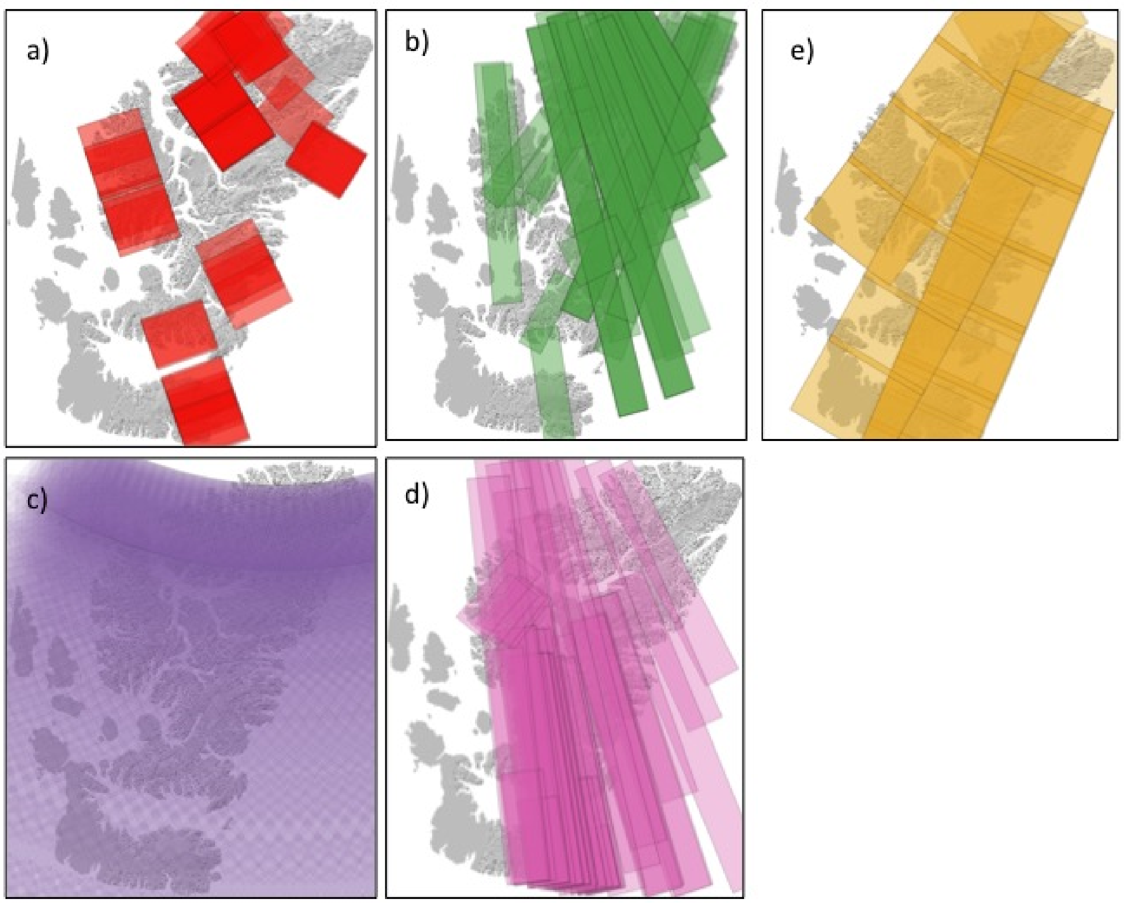

Figure A.1: *Satellite tracks employed in this study: a) ERS-1, b) RADARSAT-1, c) LANDSAT, d) ALOS/PALSAR, e) Sentinel-1a.*

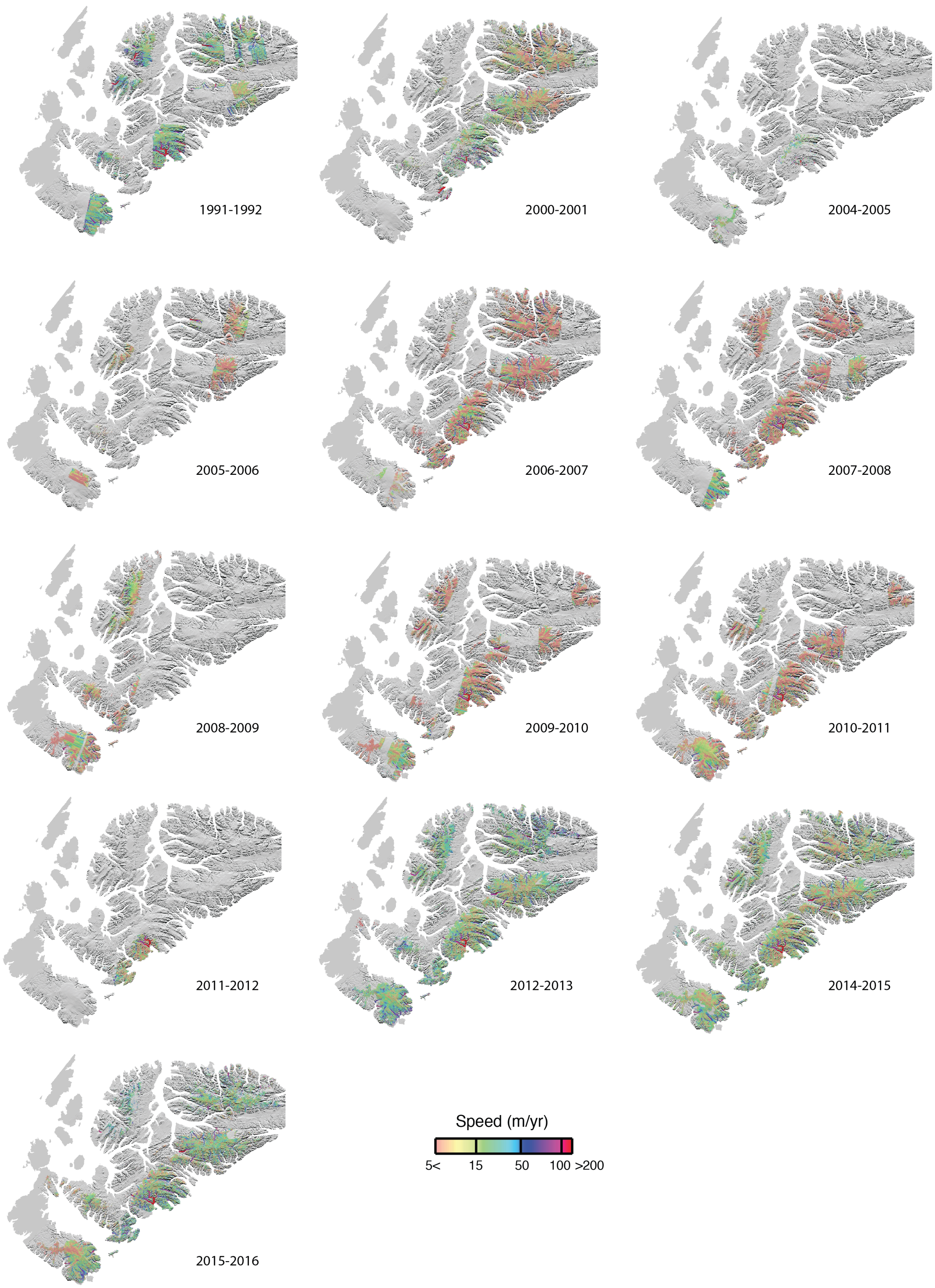

Figure A.2: *Ice velocity mosaic of the QEI, Canada, between 1991 and 2016 computed from ERS-1, RADARSAT-1, ALOS/PALSAR, LANDSAT-7/8 and Sentinel-1a data*

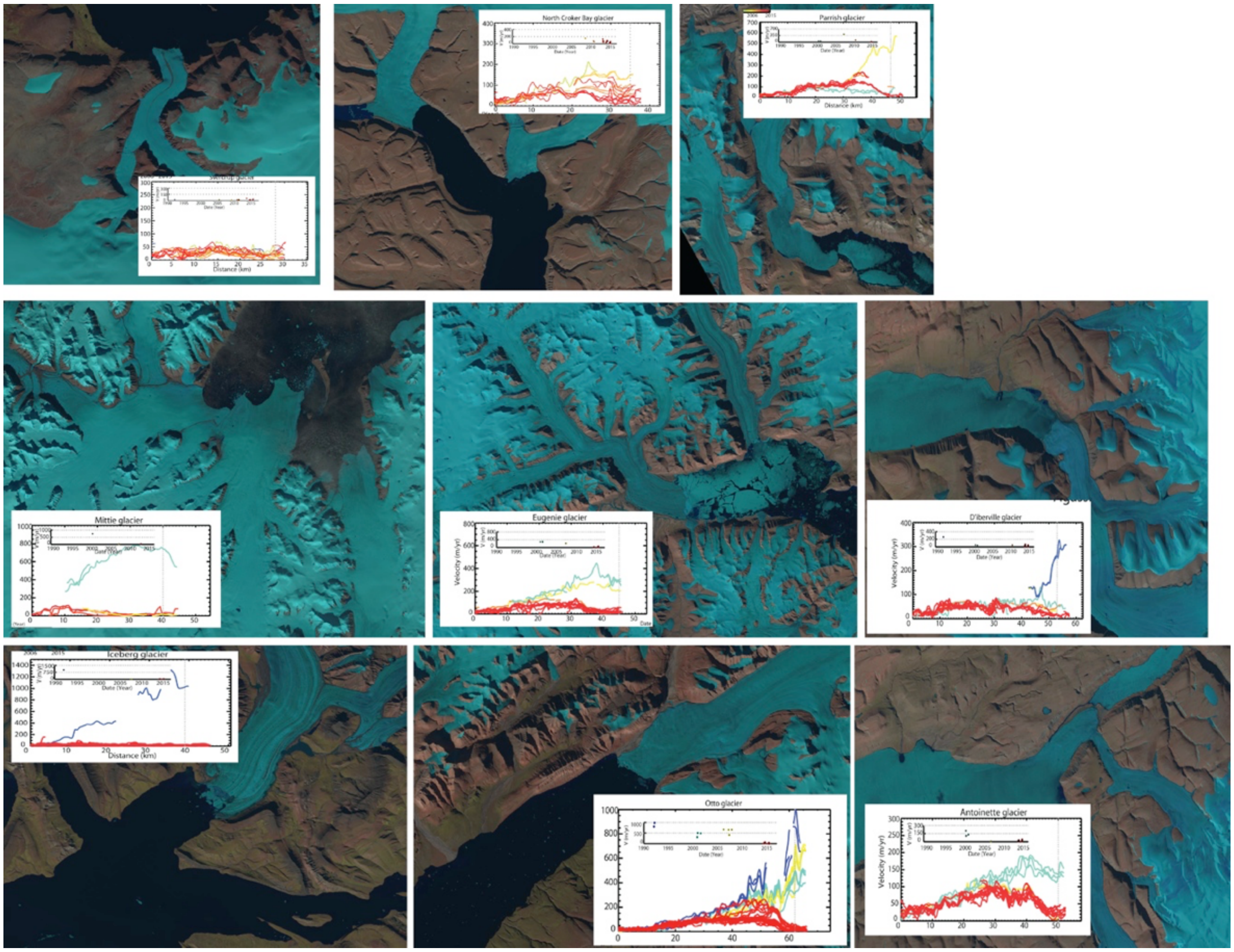

Figure A.3: *Calving front of glaciers derived from Landsat-8 images acquired between June and September from year 2014 and 2015, with near-stagnant or stagnant ice front.*

Table A.1: *Ice discharge for each glacier. Column 1-2: ice cap names, glacier names and ice discharge calculation method, Column 3: Glacier area, marine-terminating glacier area, land-terminating glacier area, Column 4 to 21 : ice discharge and error for the years 1991 to 2015. Calculation of non-surveyed glacier ice discharge is also shown for each ice cap.*

Ice cap	Glacier Name	Area (km2)	Ice Discharge (10-2 Gt/yr) 1991	1996	2000	2001	2002	2003	2004	2005	2006	2007	2008	2009	2010	2011	2012	2013	2014	2015
Agassiz	Canon*	941	4.7 ± 2.2	4.7 ± 2.2	4.7 ± 1.1	4.6 ± 2.0	4.5 ± 2.0	4.4 ± 2.0	4.2 ± 2.0	4.1 ± 2.0	4.0 ± 2.0	3.8 ± 0.9	4.6 ± 2.2	5.4 ± 1.3	5.5 ± 1.3	5.1 ± 2.4	4.7 ± 2.4	4.4 ± 1.1	6.4 ± 1.5	6.7 ± 1.6
	Diberville*	1594	7.8 ± 2.4	4.8 ± 3.1	2.3 ± 0.7	2.2 ± 1.2	2.0 ± 1.2	1.9 ± 1.2	1.8 ± 1.2	1.6 ± 1.2	1.5 ± 0.5	1.5 ± 1.0	1.6 ± 1.0	1.6 ± 1.0	1.6 ± 0.5	1.4 ± 0.8	1.2 ± 0.8	1.0 ± 0.3	1.1 ± 0.3	0.5 ± 0.3
	Glacier 4)*	1092	0.2 ± 0.1	0.3 ± 0.3	0.4 ± 0.2	0.4 ± 0.4	0.5 ± 0.4	0.5 ± 0.4	0.5 ± 0.4	0.6 ± 0.2	0.7 ± 0.3	0.3 ± 0.1	0.3 ± 0.3	0.3 ± 0.1	0.3 ± 0.3	0.3 ± 0.3	0.3 ± 0.3	0.3 ± 0.1	0.4 ± 0.1	0.5 ± 0.2
	Glacier 3)*	227	0.8 ± 0.3	0.7 ± 0.5	0.6 ± 0.2	0.6 ± 0.4	0.6 ± 0.4	0.6 ± 0.4	0.6 ± 0.4	0.5 ± 0.4	0.5 ± 0.4	0.5 ± 0.2	0.5 ± 0.4	0.6 ± 0.2	0.6 ± 0.5	0.7 ± 0.5	0.7 ± 0.3	0.8 ± 0.3	0.5 ± 0.2	0.1 ± 0.2
	Dobbin*	690	2.1 ± 1.5	2.1 ± 1.5	2.1 ± 0.7	2.1 ± 6.8	2.1 ± 6.8	2.1 ± 6.8	17.3 ± 6.1	21.1 ± 7.4	12.9 ± 4.4	9.7 ± 4.5	6.5 ± 4.5	3.2 ± 4.5	0.0 ± 0.1	0.1 ± 0.1	0.1 ± 0.1	0.2 ± 0.1	0.1 ± 0.1	0.0 ± 0.2
	Eugenie*	1087	5.3 ± 3.0	5.3 ± 3.0	5.3 ± 1.5	5.9 ± 3.8	6.5 ± 3.8	7.1 ± 3.8	7.7 ± 3.8	8.3 ± 3.8	8.9 ± 2.2	6.7 ± 2.3	4.5 ± 2.3	2.3 ± 2.3	0.1 ± 0.1	0.1 ± 0.4	0.1 ± 0.4	0.1 ± 0.3	0.1 ± 0.1	0.1 ± 0.1
	John Richardson*	669	1.3 ± 0.5	2.2 ± 1.4	2.9 ± 0.9	3.1 ± 2.0	3.3 ± 2.0	3.4 ± 2.0	3.6 ± 2.0	3.8 ± 1.1	2.9 ± 0.9	3.1 ± 1.0	3.1 ± 1.9	3.2 ± 1.9	3.2 ± 1.9	3.2 ± 1.9	3.2 ± 0.9	3.2 ± 0.9	3.2 ± 0.9	2.2 ± 0.8
	Parrish	770	0.2 ± 0.1	0.2 ± 0.1	0.2 ± 0.0	0.2 ± 0.5	0.2 ± 0.5	0.2 ± 0.5	0.2 ± 0.5	0.2 ± 0.5	20.1 ± 0.5	19.1 ± 0.4	13.1 ± 0.6	7.0 ± 0.2	5.0 ± 0.1	3.5 ± 0.2	2.0 ± 0.2	0.5 ± 0.1	1.0 ± 0.1	0.4 ± 0.1
	Tuborg*	490	2.5 ± 0.9	4.1 ± 2.9	5.3 ± 2.0	4.3 ± 2.2	3.3 ± 2.2	2.3 ± 2.2	1.3 ± 2.2	0.3 ± 0.2	2.2 ± 1.0	2.5 ± 2.6	2.8 ± 2.6	3.2 ± 2.6	3.5 ± 1.6	4.1 ± 3.5	4.8 ± 3.5	5.4 ± 2.0	5.1 ± 2.0	3.4 ± 1.7
	Antoinette*	1000	3.4 ± 2.1	3.4 ± 2.1	3.3 ± 1.0	2.9 ± 1.2	2.4 ± 1.2	1.9 ± 1.2	1.4 ± 1.2	0.9 ± 1.2	0.4 ± 0.2	0.3 ± 0.2	0.2 ± 0.2	0.1 ± 0.2	0.0 ± 0.0	0.1 ± 0.1	0.1 ± 0.1	0.2 ± 0.1	0.2 ± 0.1	0.1 ± 0.2
	Surveyed	**8561**	**28.4** ± 5.3	27.7 ± 6.4	**27.2** ± 3.2	26.2 ± 8.8	25.3 ± 8.8	24.3 ± 8.8	38.6 ± 8.2	**41.4** ± 8.8	**54.1** ± 5.6	**47.6** ± 5.9	37.2 ± 6.5	**26.9** ± 6.2	**19.8** ± 2.9	18.5 ± 4.7	17.2 ± 4.4	**16.0** ± 2.5	**18.0** ± 2.7	**14.1** ± 2.5
	All land term.	12272			Discharge non surv. : 0.9 ± 0.9															
	All tidewaters	**8844**	**29.3** ± 5.3	28.6 ± 6.5	**28.1** ± 3.4	27.1 ± 8.8	26.1 ± 8.8	25.1 ± 8.8	39.9 ± 8.3	**42.8** ± 8.9	**55.9** ± 5.6	**49.2** ± 6.0	38.5 ± 6.5	**27.8** ± 6.2	**20.5** ± 3.0	19.1 ± 4.8	17.8 ± 4.5	**16.5** ± 2.6	**18.6** ± 2.8	**14.6** ± 2.7
Devon	Belcher	1134.4	9.2 ± 0.2	9.0 ± 0.4	8.9 ± 0.4	8.9 ± 0.4	8.9 ± 0.4	8.8 ± 0.4	8.8 ± 0.4	8.8 ± 0.4	8.8 ± 0.4	8.7 ± 0.2	10.7 ± 0.2	12.1 ± 0.3	9.9 ± 0.2	10.7 ± 0.5	11.5 ± 0.5	12.3 ± 0.3	15.6 ± 0.3	21.7 ± 0.4
	East7	471.1	4.4 ± 0.1	4.1 ± 0.3	3.8 ± 0.3	3.7 ± 0.3	3.6 ± 0.3	3.5 ± 0.3	3.5 ± 0.3	3.4 ± 0.3	3.3 ± 0.3	3.2 ± 0.1	3.6 ± 0.1	3.7 ± 0.1	2.7 ± 0.1	2.6 ± 0.2	2.6 ± 0.2	2.5 ± 0.1	1.5 ± 0.1	0.8 ± 0.1
	Eastern	663.9	2.4 ± 0.1	2.1 ± 0.2	1.8 ± 0.2	1.7 ± 0.2	1.7 ± 0.2	1.6 ± 0.2	1.5 ± 0.2	1.5 ± 0.2	1.4 ± 0.2	1.3 ± 0.1	2.2 ± 0.1	2.7 ± 0.1	1.8 ± 0.1	2.3 ± 0.2	2.7 ± 0.2	3.1 ± 0.1	2.6 ± 0.1	1.8 ± 0.1
	Fitzroy	572	4.6 ± 0.1	4.6 ± 0.3	4.8 ± 0.3	4.9 ± 0.3	5.0 ± 0.3	5.0 ± 0.3	5.1 ± 0.3	5.1 ± 0.3	5.2 ± 0.3	5.6 ± 0.2	6.6 ± 0.2	7.8 ± 0.2	5.6 ± 0.2	5.9 ± 0.3	6.3 ± 0.3	6.6 ± 0.2	6.4 ± 0.2	5.0 ± 0.2
	NCB	2170.6	4.6 ± 0.7	4.6 ± 0.4	5.5 ± 0.5	5.7 ± 0.5	6.0 ± 0.5	6.2 ± 0.5	6.4 ± 0.5	6.7 ± 0.5	6.9 ± 0.5	7.2 ± 0.5	7.4 ± 0.2	4.8 ± 0.3	2.2 ± 0.1	2.5 ± 0.2	2.7 ± 0.2	2.9 ± 0.1	1.5 ± 0.1	0.7 ± 0.1
	SCB		5.8 ± 0.7	5.8 ± 0.4	5.3 ± 0.5	5.1 ± 0.5	5.0 ± 0.5	4.9 ± 0.5	4.7 ± 0.1	4.8 ± 0.3	4.9 ± 0.3	4.9 ± 0.3	5.0 ± 0.2	4.9 ± 0.3	4.7 ± 0.1	5.5 ± 0.3	6.4 ± 0.3	7.2 ± 0.2	6.9 ± 0.2	7.3 ± 0.2
	Southeast	2622.8	6.0 ± 0.2	5.5 ± 0.4	5.1 ± 0.4	5.0 ± 0.4	4.9 ± 0.4	4.8 ± 0.4	4.7 ± 0.4	4.6 ± 0.4	4.5 ± 0.4	4.4 ± 0.2	5.0 ± 0.2	5.5 ± 0.2	4.8 ± 0.2	6.2 ± 0.4	7.5 ± 0.4	8.9 ± 0.2	8.6 ± 0.2	5.6 ± 0.2
	Sverdrup	765.4	0.6 ± 0.1	0.6 ± 0.1	0.6 ± 0.1	0.6 ± 0.1	0.6 ± 0.1	0.6 ± 0.1	0.6 ± 0.1	0.5 ± 0.1	0.5 ± 0.1	0.5 ± 0.1	0.5 ± 0.1	0.4 ± 0.1	0.5 ± 0.1	0.4 ± 0.2	0.3 ± 0.2	0.1 ± 0.1	0.0 ± 0.1	0.6 ± 0.1
	Surveyed	8400.2	**37.5** ± 1.1	**36.2** ± 0.9	35.8 ± 1.0	35.7 ± 1.0	35.6 ± 1.0	35.5 ± 1.0	**35.4** ± 0.9	35.5 ± 0.9	35.5 ± 0.9	**36.0** ± 0.7	**41.0** ± 0.5	**41.8** ± 0.6	**32.3** ± 0.4	36.1 ± 0.9	39.9 ± 0.9	**43.7** ± 0.5	**43.0** ± 0.5	**43.5** ± 1.2
	All land term.	4722			Discharge non surv. : 8.0 ± 8.0															
	All tidewaters	**10275**	**45.6** ± 8.1	**44.2** ± 8.1	43.8 ± 8.1	43.6 ± 8.1	43.5 ± 8.1	43.4 ± 8.1	**43.3** ± 8.1	43.4 ± 8.1	43.5 ± 8.1	**44.0** ± 8.0	**50.2** ± 8.0	**51.1** ± 8.0	**39.5** ± 8.0	44.2 ± 8.1	48.8 ± 8.1	**53.5** ± 8.0	**52.6** ± 8.0	**53.2** ± 8.1
NEI	Disraeli*	1384.5	0.9 ± 0.6	0.9 ± 0.6	0.9 ± 0.3	1.0 ± 0.8	1.0 ± 0.8	1.1 ± 0.8	1.1 ± 0.8	1.1 ± 0.8	1.2 ± 0.8	1.2 ± 0.8	1.2 ± 0.8	1.3 ± 0.4	1.3 ± 0.4	1.4 ± 1.1	1.6 ± 1.1	1.7 ± 1.1	1.9 ± 0.7	1.6 ± 0.6
	Milne*	1078.3	5.1 ± 1.2	4.8 ± 2.3	4.6 ± 1.1	4.5 ± 2.1	4.4 ± 2.1	4.3 ± 2.1	4.2 ± 2.1	4.1 ± 2.1	4.0 ± 1.0	4.0 ± 1.9	3.9 ± 1.9	3.8 ± 1.9	3.8 ± 1.9	3.7 ± 1.9	3.6 ± 1.9	3.6 ± 0.9	3.0 ± 0.7	4.1 ± 1.0
	De Vries*	875.3	0.5 ± 0.2	0.3 ± 0.3	0.2 ± 0.2	0.2 ± 0.3	0.2 ± 0.3	0.3 ± 0.3	0.3 ± 0.3	0.3 ± 0.3	0.3 ± 0.2	0.6 ± 0.2	0.6 ± 0.5	0.5 ± 0.5	0.4 ± 0.5	0.3 ± 0.5	0.2 ± 0.5	0.1 ± 0.2	0.2 ± 0.2	0.5 ± 0.6
	M'Clintock*	1734.5	1.7 ± 0.7	1.5 ± 1.2	1.4 ± 0.6	1.4 ± 1.2	1.4 ± 1.2	1.5 ± 1.2	1.5 ± 1.2	1.5 ± 0.6	1.4 ± 0.6	1.5 ± 1.3	1.5 ± 1.3	1.6 ± 1.3	1.6 ± 1.3	1.7 ± 1.3	1.7 ± 1.3	1.8 ± 1.3	1.9 ± 0.7	1.7 ± 0.8
	Otto*	1214.8	24.7 ± 6.8	15.2 ± 9.2	7.7 ± 2.3	9.9 ± 7.5	12.1 ± 7.5	14.3 ± 7.5	16.6 ± 7.5	18.8 ± 5.1	18.9 ± 5.2	19.1 ± 5.2	15.9 ± 6.9	12.7 ± 6.9	9.6 ± 6.9	6.4 ± 1.8	3.3 ± 1.0	0.1 ± 0.1	0.3 ± 0.1	0.3 ± 0.3
	Glacier 1)*	660.6	0.2 ± 0.2	0.4 ± 0.4	0.5 ± 0.2	0.6 ± 0.4	0.6 ± 0.4	0.6 ± 0.4	0.6 ± 0.4	0.6 ± 0.4	0.6 ± 0.2	0.5 ± 0.4	0.4 ± 0.4	0.4 ± 0.4	0.3 ± 0.4	0.2 ± 0.4	0.1 ± 0.4	0.0 ± 0.2	0.4 ± 0.2	0.1 ± 0.2
	Glacier 2)*	205.1	2.2 ± 0.7	2.8 ± 1.6	3.2 ± 0.9	3.3 ± 2.0	3.5 ± 2.0	3.6 ± 2.0	3.8 ± 2.0	3.9 ± 2.0	4.0 ± 1.1	3.2 ± 0.9	3.1 ± 1.6	3.0 ± 1.6	2.9 ± 1.6	2.8 ± 1.6	2.7 ± 1.6	2.6 ± 0.7	3.0 ± 0.8	2.0 ± 0.6
	Yelverton*	774.6	11.4 ± 5.8	11.4 ± 5.8	11.4 ± 2.9	11.5 ± 5.8	11.6 ± 5.8	11.7 ± 5.8	11.7 ± 5.8	11.8 ± 5.8	11.9 ± 3.0	11.0 ± 2.8	10.9 ± 5.6	10.9 ± 5.6	10.8 ± 5.6	10.7 ± 5.6	10.6 ± 5.6	10.5 ± 2.7	11.7 ± 2.9	10.6 ± 2.8
	Surveyed	**7927.7**	**46.7** ± 9.1	37.4 ± 11.3	**29.9** ± 4.0	32.4 ± 10.0	34.8 ± 10.0	37.3 ± 10.0	39.8 ± 10.0	**42.2** ± 8.4	**42.5** ± 6.3	**41.1** ± 6.4	37.6 ± 9.4	**34.1** ± 9.4	**30.5** ± 9.4	27.2 ± 6.6	23.8 ± 6.4	**20.5** ± 3.4	**22.3** ± 3.2	**20.9** ± 3.2
	All land term.	16871			Discharge non surv. : 10.1 ± 10.1															
	All tidewaters	**10343**	**56.9** ± 13.6	47.5 ± 15.2	**40.1** ± 10.9	42.5 ± 14.2	45.0 ± 14.2	47.4 ± 14.2	49.9 ± 14.2	**52.3** ± 13.1	**52.6** ± 11.9	**51.3** ± 12.0	47.8 ± 13.8	**44.3** ± 13.8	**40.7** ± 13.8	37.3 ± 12.1	33.9 ± 12.0	**30.6** ± 10.7	**32.5** ± 10.6	**31.0** ± 10.6
AHI	GoodFriday	731	21.2 ± 5.1	18.4 ± 7.5	16.0 ± 7.5	15.5 ± 7.5	14.9 ± 7.5	14.3 ± 7.5	13.7 ± 7.5	13.2 ± 7.5	12.6 ± 7.5	12.0 ± 7.5	11.4 ± 7.5	10.9 ± 2.4	10.4 ± 2.3	9.9 ± 4.3	9.4 ± 4.3	8.9 ± 1.9	7.8 ± 1.8	7.8 ± 1.8
	Iceberg*	1056.2	64.9 ± 14.1	0.1 ± 1.0	0.1 ± 0.2	0.1 ± 0.2	0.1 ± 0.7	0.1 ± 0.7	0.1 ± 0.7	0.1 ± 0.5	0.1 ± 0.5	0.1 ± 0.1	0.2 ± 0.1	0.1 ± 0.1	0.2 ± 0.3	0.3 ± 0.3	0.4 ± 0.3	0.5 ± 0.2	0.8 ± 0.2	1.6 ± 0.4
	Surveyed	1787.2	**86.2** ± 15.0	18.4 ± 7.6	16.1 ± 7.6	15.5 ± 7.6	15.0 ± 7.6	14.4 ± 7.6	13.8 ± 7.6	13.2 ± 7.6	12.7 ± 7.6	**12.1** ± 7.5	**11.6** ± 7.6	**10.9** ± 2.4	**10.5** ± 2.4	10.1 ± 4.3	9.8 ± 4.3	**9.4** ± 2.0	**8.5** ± 1.8	**9.4** ± 1.8
	All land term.	10116			Discharge non surv. : 0.0 ± 0.0															
	All tidewaters	**1791**	**86.2** ± 15.0	18.5 ± 7.6	16.1 ± 7.6	15.6 ± 7.6	15.0 ± 7.6	14.4 ± 7.6	13.8 ± 7.6	13.3 ± 7.6	12.7 ± 7.6	**12.1** ± 7.5	**11.6** ± 7.6	**11.0** ± 2.4	**10.6** ± 2.4	10.2 ± 4.3	9.8 ± 4.3	**9.4** ± 2.0	**8.6** ± 1.8	**9.4** ± 1.8
Sydkap/Mittie	Mittie	1741.3	3.9 ± 0.3	3.9 ± 0.3	89.3 ± 1.0	46.1 ± 1.1	24.6 ± 1.1	3.0 ± 1.1	3.0 ± 1.1	3.0 ± 1.1	3.9 ± 0.1	0.2 ± 0.1	0.3 ± 0.1	0.3 ± 0.1	0.4 ± 0.1	0.4 ± 0.1	0.4 ± 0.1	4.8 ± 0.1	4.8 ± 0.1	1.0 ± 0.1
	Glacier 11)	498.2	0.9 ± 0.5	0.9 ± 0.5	0.9 ± 0.5	0.9 ± 0.5	0.9 ± 0.5	0.9 ± 0.5	0.9 ± 0.5	0.9 ± 0.5	0.9 ± 0.3	3.9 ± 1.0	1.7 ± 0.4	0.4 ± 0.2	1.6 ± 0.4	1.5 ± 0.7	1.3 ± 0.7	1.1 ± 0.4	1.5 ± 0.4	0.7 ± 0.7
	Sydkap	490.8	4.3 ± 0.1	3.7 ± 0.2	3.3 ± 0.1	3.3 ± 0.2	3.3 ± 0.2	3.2 ± 0.2	3.2 ± 0.2	3.2 ± 0.2	3.2 ± 0.2	3.2 ± 0.2	3.1 ± 0.1	2.8 ± 0.2	2.5 ± 0.1	2.4 ± 0.2	2.4 ± 0.2	2.3 ± 0.1	4.1 ± 0.1	4.7 ± 0.2
	Surveyed	2730.3	**9.1** ± 0.6	8.6 ± 0.6	**93.5** ± 1.1	50.3 ± 1.3	28.7 ± 1.3	7.1 ± 1.3	7.1 ± 1.3	7.1 ± 1.3	**8.0** ± 0.4	**7.3** ± 1.0	**5.1** ± 0.4	**3.6** ± 0.3	**4.5** ± 0.4	4.3 ± 0.7	**4.1** ± 0.7	**8.2** ± 0.4	**10.3** ± 0.4	**6.5** ± 0.7
	All land term.	4977			Discharge non surv. : 6.2 ± 6.2															
	All tidewaters	**5075**	**15.3** ± 6.2	14.8 ± 6.2	**99.7** ± 6.3	56.5 ± 6.3	34.9 ± 6.3	13.3 ± 6.3	13.3 ± 6.3	13.3 ± 6.3	**14.2** ± 6.2	**13.5** ± 6.3	**11.3** ± 6.2	**9.8** ± 6.2	**10.7** ± 6.2	10.5 ± 6.2	**10.3** ± 6.2	**14.4** ± 6.2	**16.5** ± 6.2	**12.7** ± 6.2
PoW	Glacier 10)	180	0.1 ± 0.2	0.1 ± 0.4	0.1 ± 0.1	0.1 ± 0.2	0.2 ± 0.2	0.2 ± 0.2	0.2 ± 0.2	0.2 ± 0.2	0.2 ± 0.1	0.2 ± 0.1	0.2 ± 0.2	0.2 ± 0.2	0.2 ± 0.1	0.2 ± 0.3	0.1 ± 0.2	0.0 ± 0.0	0.1 ± 0.0	0.3 ± 0.1
	Glacier 9)	324	18.0 ± 6.4	8.4 ± 6.9	0.8 ± 0.4	3.7 ± 7.0	6.6 ± 7.0	9.5 ± 7.0	12.4 ± 7.0	15.3 ± 7.0	18.2 ± 6.5	6.0 ± 2.3	5.3 ± 2.9	4.6 ± 2.9	3.8 ± 2.9	3.1 ± 2.9	2.3 ± 2.9	1.6 ± 0.6	2.4 ± 0.9	4.9 ± 1.8
	Ekbaw	1530.3	16.2 ± 9.3	16.2 ± 9.3	16.2 ± 4.6	16.0 ± 9.0	15.7 ± 9.0	15.4 ± 9.0	15.1 ± 9.0	14.9 ± 9.0	14.6 ± 9.0	14.3 ± 4.4	14.2 ± 6.7	14.0 ± 4.3	13.9 ± 4.1	12.2 ± 6.7	10.4 ± 6.7	8.6 ± 2.6	9.9 ± 2.9	5.7 ± 2.0
	Leffert	583.4	0.8 ± 0.6	0.8 ± 0.6	0.8 ± 0.3	0.8 ± 0.7	0.9 ± 0.7	1.0 ± 0.7	1.0 ± 0.7	1.1 ± 0.7	1.1 ± 0.7	1.2 ± 0.4	1.2 ± 0.8	1.1 ± 0.4	1.3 ± 0.4	1.2 ± 0.8	1.2 ± 0.8	1.2 ± 0.4	0.8 ± 0.3	0.1 ± 0.1
	Glacier 8)	1892	19.8 ± 0.3	13.6 ± 0.5	8.7 ± 0.5	7.5 ± 0.5	6.3 ± 0.5	5.1 ± 0.5	3.8 ± 0.5	2.6 ± 0.5	1.4 ± 0.5	0.2 ± 0.2	0.8 ± 0.3	1.5 ± 0.2	2.0 ± 0.2	2.2 ± 0.4	2.3 ± 0.2	1.2 ± 0.2	1.2 ± 0.2	0.2 ± 0.2
	Stygge	363.6	0.2 ± 0.1	0.3 ± 0.3	0.4 ± 0.2	0.4 ± 0.4	0.5 ± 0.4	0.5 ± 0.4	0.5 ± 0.2	0.5 ± 0.4	0.5 ± 0.2	0.5 ± 0.2	0.5 ± 0.4	0.5 ± 0.2	0.5 ± 0.2	0.4 ± 0.4	0.3 ± 0.4	0.3 ± 0.2	0.5 ± 0.2	0.6 ± 0.2
	Trinity	3085.1	66.4 ± 0.8	39.8 ± 1.3	18.6 ± 0.5	20.7 ± 1.1	22.7 ± 1.1	24.8 ± 1.1	26.9 ± 0.6	58.3 ± 1.6	89.6 ± 1.0	49.9 ± 0.6	78.0 ± 1.8	106.1 ± 1.2	105.1 ± 1.2	104.8 ± 2.3	104.5 ± 1.2	121.1 ± 1.3	127.6 ± 1.3	130.1 ± 1.4
	Wykeham		27.5 ± 0.4	21.5 ± 0.6	16.6 ± 0.3	19.0 ± 0.7	21.5 ± 0.7	23.9 ± 0.7	26.3 ± 0.7	28.7 ± 0.7	31.2 ± 0.4	12.1 ± 0.2	19.8 ± 0.6	27.4 ± 0.4	29.7 ± 0.4	37.0 ± 1.0	44.2 ± 0.6	49.4 ± 0.6	50.3 ± 0.6	52.5 ± 0.6
	Glacier 5)	212	2.4 ± 0.2	2.4 ± 0.2	2.4 ± 0.1	2.4 ± 0.2	2.4 ± 0.2	2.3 ± 0.2	2.3 ± 0.2	2.2 ± 0.2	2.2 ± 0.2	2.1 ± 0.1	2.7 ± 0.2	3.2 ± 0.1	2.1 ± 0.1	2.6 ± 0.2	3.0 ± 0.2	3.5 ± 0.1	3.3 ± 0.1	0.7 ± 0.1
	Glacier 7)	181.3	3.5 ± 0.1	3.0 ± 0.3	2.7 ± 0.1	2.8 ± 0.3	2.9 ± 0.3	3.1 ± 0.3	3.2 ± 0.3	3.3 ± 0.3	3.4 ± 0.1	1.8 ± 0.1	2.2 ± 0.2	2.5 ± 0.1	1.7 ± 0.1	1.2 ± 0.2	0.6 ± 0.1	1.1 ± 0.1	1.3 ± 0.1	0.5 ± 0.0
	Glacier 6)	176	3.4 ± 0.1	3.1 ± 0.2	2.8 ± 0.1	2.3 ± 1.2	1.8 ± 1.2	1.3 ± 1.2	0.8 ± 1.1	0.9 ± 1.1	1.1 ± 0.1	0.9 ± 0.1	0.8 ± 0.1	0.6 ± 0.1	0.2 ± 0.0	0.2 ± 0.1	0.1 ± 0.0	0.1 ± 0.0	0.2 ± 0.0	0.3 ± 0.0
	Cadogan	738.3	16.7 ± 0.3	11.7 ± 0.5	7.6 ± 0.2	8.1 ± 0.4	8.6 ± 0.4	9.2 ± 0.4	9.7 ± 0.2	9.1 ± 0.4	8.5 ± 0.2	7.9 ± 0.2	7.8 ± 0.4	7.7 ± 0.2	6.7 ± 0.2	6.4 ± 0.4	6.1 ± 0.4	5.8 ± 0.2	5.8 ± 0.2	4.4 ± 0.2
	Surveyed	9266	175.0 ± 11.4	121.0 ± 11.7	77.7 ± 4.7	83.9 ± 11.6	90.1 ± 11.6	96.2 ± 11.6	102.4 ± 11.5	137.2 ± 11.6	172.0 ± 11.2	97.1 ± 5.0	133.4 ± 5.4	169.6 ± 5.4	167.2 ± 5.2	171.2 ± 7.8	175.2 ± 7.5	193.9 ± 3.1	203.3 ± 3.4	200.2 ± 3.1
	All land term.	7102			Discharge non surv. : 45.4 ± 45.4															
	All tidewaters	**12032**	**220.5** ± 46.8	166.4 ± 46.9	**123.1** ± 45.7	129.3 ± 46.9	135.5 ± 46.9	141.6 ± 46.9	**147.8** ± 46.9	182.6 ± 46.9	**217.4** ± 46.8	**142.6** ± 45.7	178.8 ± 46.4	**215.1** ± 45.7	**212.6** ± 45.7	216.6 ± 46.1	**220.6** ± 46.0	**239.3** ± 45.5	**248.7** ± 45.5	**245.6** ± 45.5
	Others land term	435.42																		
	Surveyed	38672	383.0																	
	All tidewaters	48359	80 %																	
	Total	104854	**453.6** ± 52.3	320.0 ± 51.3	**350.9** ± 48.8	314.7 ± 51.4	300.0 ± 51	285.3 ± 51.4	**307.9** ± 51.3	**347.6** ± 51.1	**396.3** ± 50.2	**312.6** ± 49.3	**338.1** ± 50.4	**358.9** ± 49.3	**334.6** ± 49	337.9 ± 49	**341.3** ± 49.1	**363.6** ± 48	**377.5** ± 48	**366.5** ± 48

Legend

Black	Surveyed
Grey	Interpolated
Green	Extrapolated (closest non surging value). Corresponding error is multiplied by 2.
Areas	From the Randolph Glacier Inventory
Icecaps abbreviations	
DIC	Devon Ice Cap
NEI	Northern Ellsmere Icefield
AHI	Axel heiberg Island
PoW	Prince of Wales Icefield
Ice discharge Method	
*	Centerline
	Flux-gate

Note: All discharge are given in Gigaton per year (Gt/yr) or 10^12 kg/yr.

Appendix B

Supplementary Information for Chapter 3

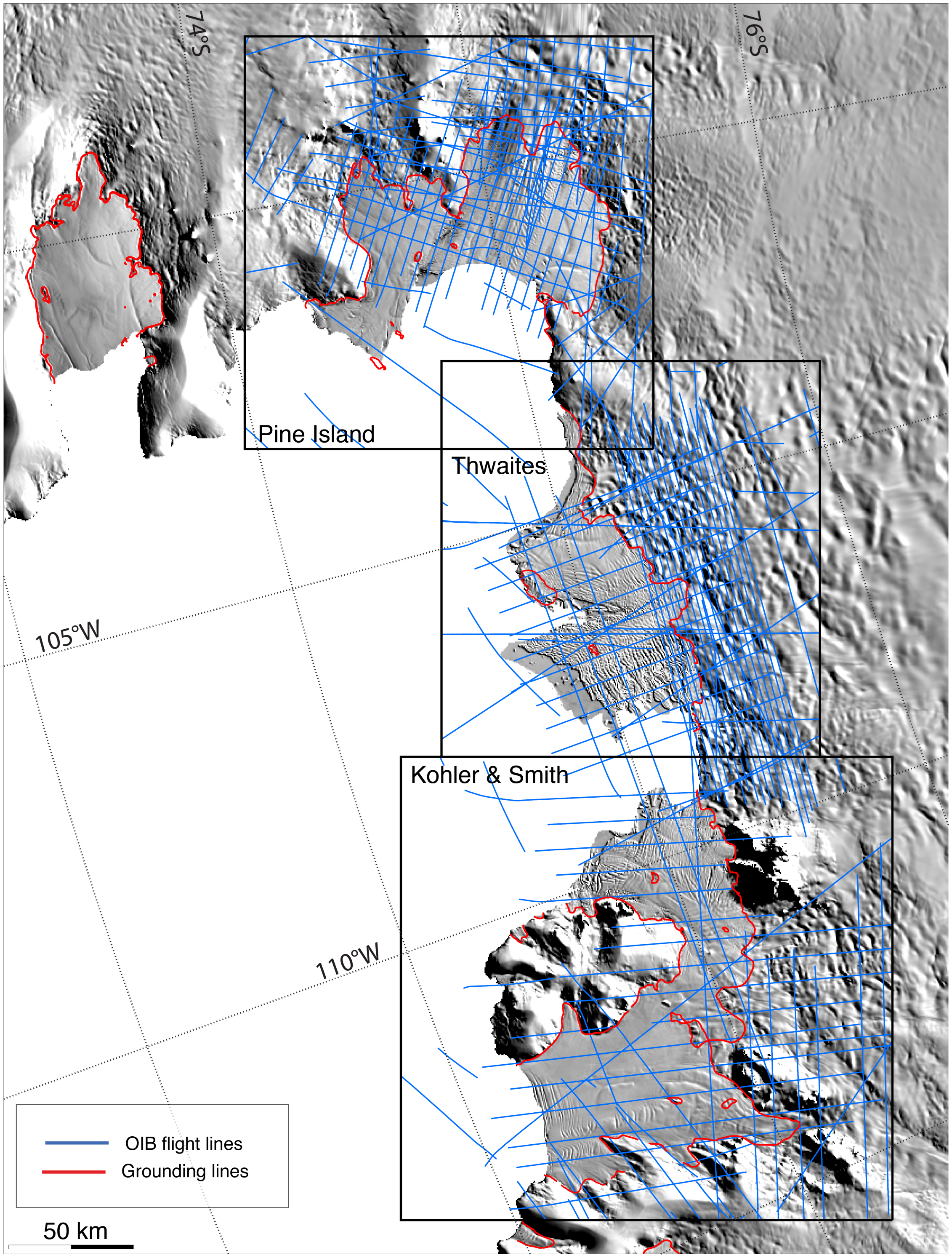

Figure B.1: *Select 32 OIB flight lines (blue thin line) acquired between 2009 and 2014 over the Amundsen Sea Embayment sector, West Antarctica with the 3 inversion domains: 1) Pine Island, 2) Thwaites, and 3) Kohler/Smith glaciers delineated with black solid rectangles. Grounding line positions in year 1996 are thin red lines. Ocean is white. Background is a MODIS mosaic of Antarctica from year 2004.*

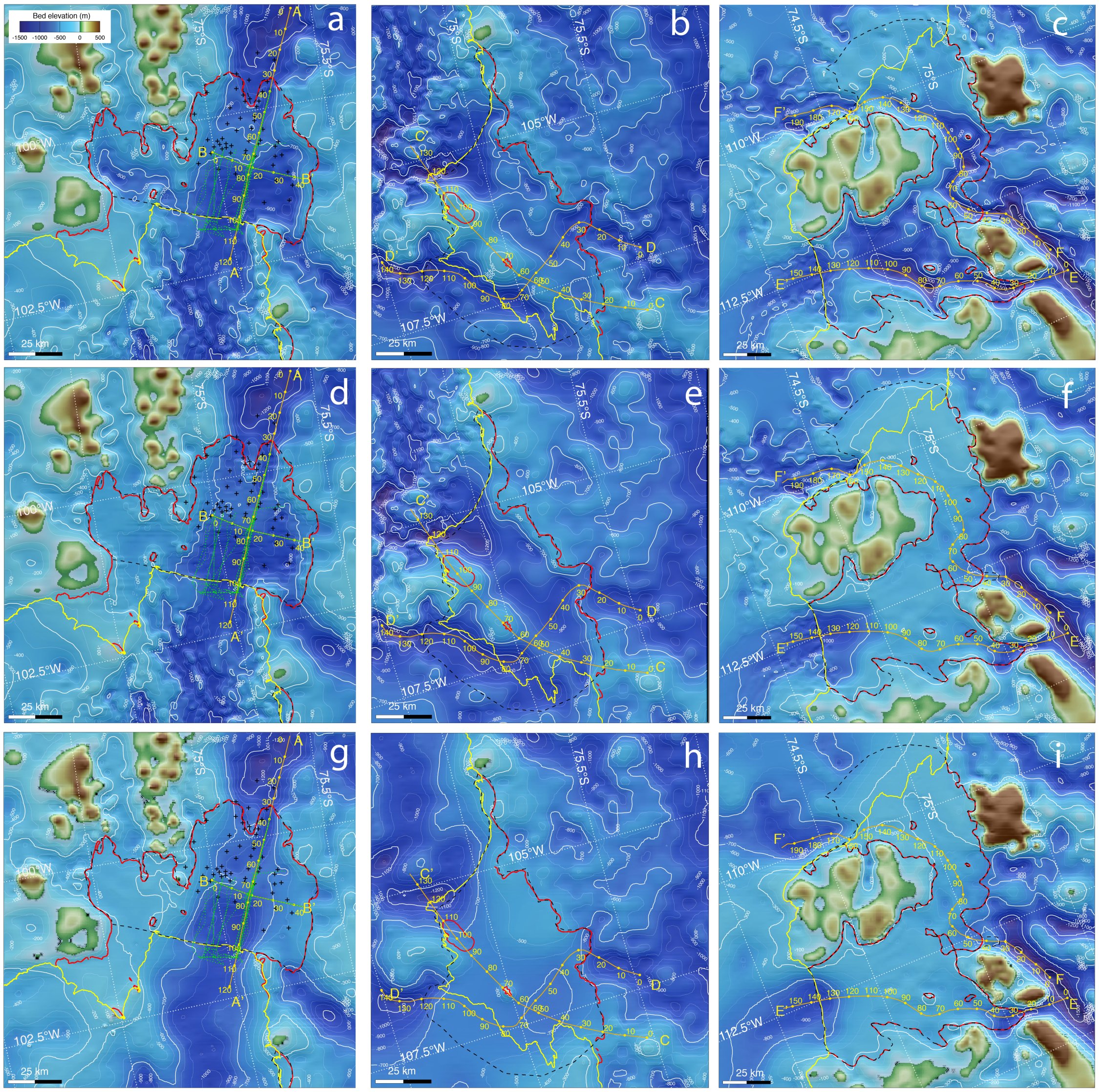

Figure B.2: *Bed elevation of (a, d, g) Pine Island, (b, e, h) Thwaites, and (c, f, i) Kohler and Smith glaciers, in West Antarctica combining Mass Conservation inland, IBCSO off shore, and OIB gravity data beneath the ice shelves (black dot domain) with additional constraint from AUV and seismic data for (a). Bed elevation from (d) [Muto et al., 2016], (e,f) IBCSO, and (g, h, i) BEDMAP-2 [Fretwell et al., 2013]. All other notations similar to Figure 2.*

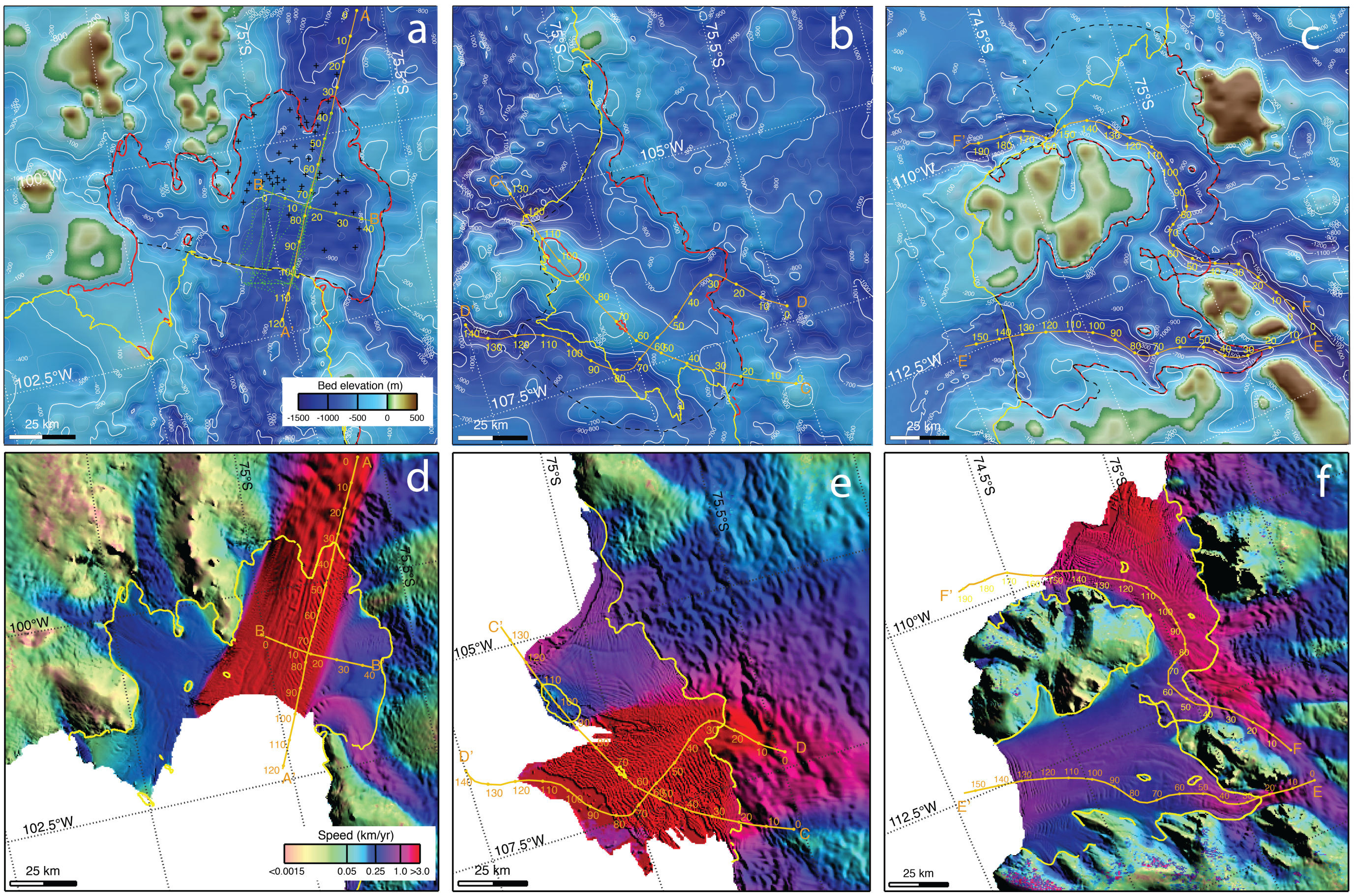

Figure B.3: *Bed elevation of the Amundsen Sea Embayment sector of West Antarctica (top, a-c) inferred from OIB gravity data versus ice speed on a logarithmic scale (bottom d-f) from [Rignot et al., 2011]. In (a-c), ice front position is yellow, 1996 grounding line is red. In (d-f), 1996 grounding line is yellow. Profiles A-A' through F-F' are orange, with dots every 10 km. Bed elevation contours are every 200 m, with a thicker contour for 800 m depth.*

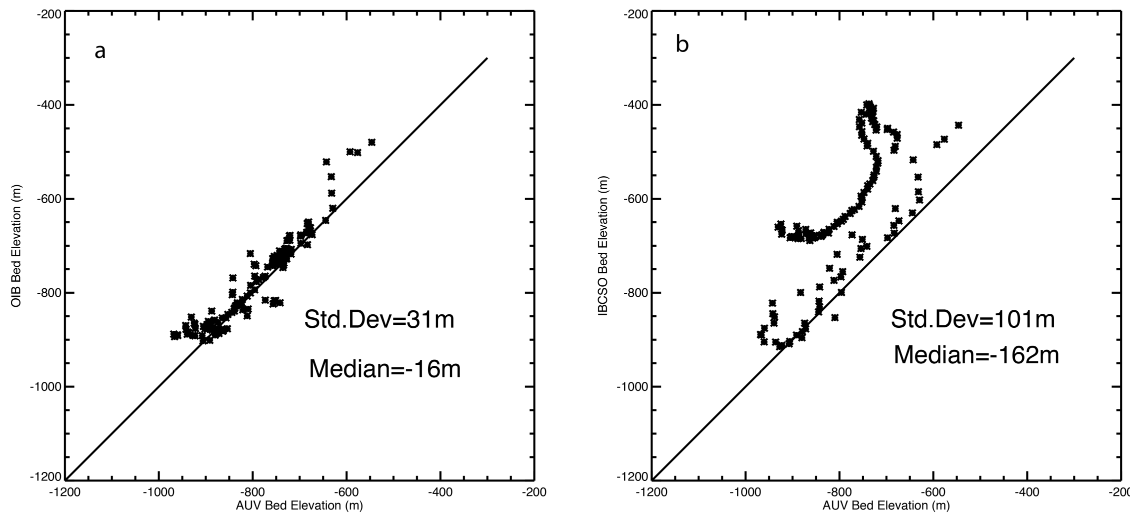

Figure B.4: *Bed elevation in meters above sea level from the Autosub Vehicle (AUV) data along profile B-B' (see Fig. 1-2) in Pine Island Bay, West Antarctica versus bed elevation from (a) OIB and (b) IBCSO. Insets indicate the median and standard deviation of the difference between (AUV-OIB) and (AUV-IBCSO).*

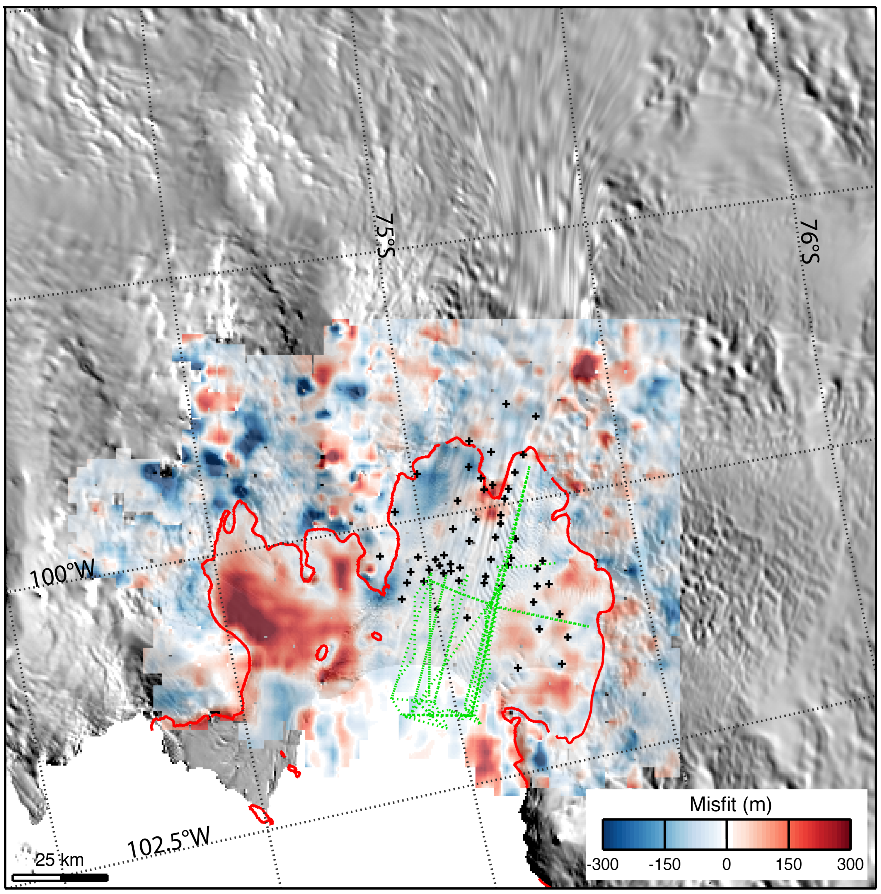

Figure B.5: *Bed elevation misfit in meters between [Muto et al.,2016] and this study (difference [Muto et al.,, 2016]-This study). Red color represents areas where our inversion is deeper than [Muto et al., 2016] and blue color represents areas where our inversion is shallower than [Muto et al., 2016]. Black dots represent the location of seismic observations. Green dashed lines represent the AUV measurements. The 1996 grounding line is red line.*

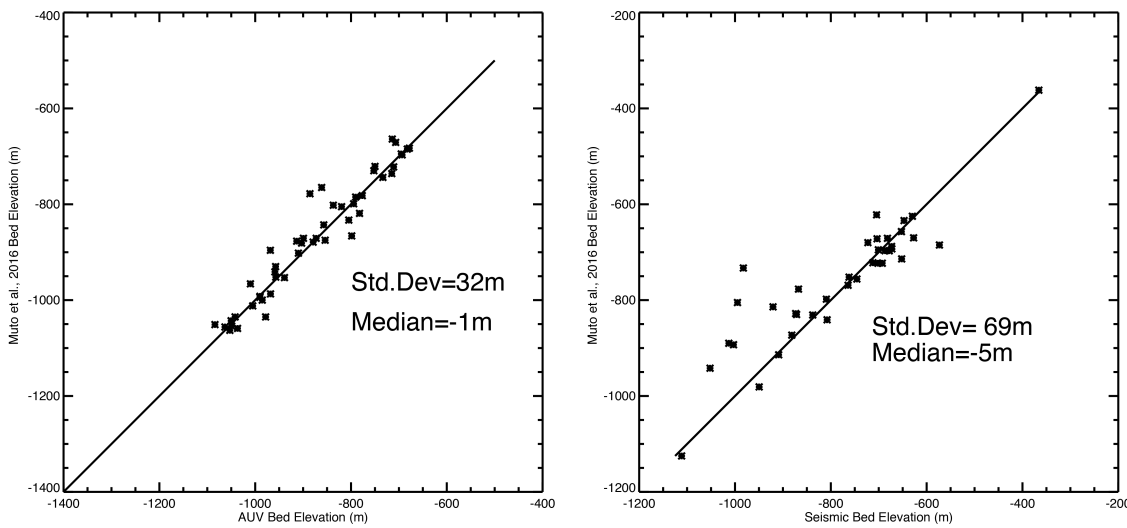

Figure B.6: *Comparison of the bed elevation from [Muto et al., 2016] with (a) AUV and (b) seismic data employed in [Muto et al., 2016]. Insets indicate the median and standard deviation of the difference between the bed elevation and the AUV data in (a) and seismic data in (b).*

Appendix C

Supplementary Information for Chapter 4

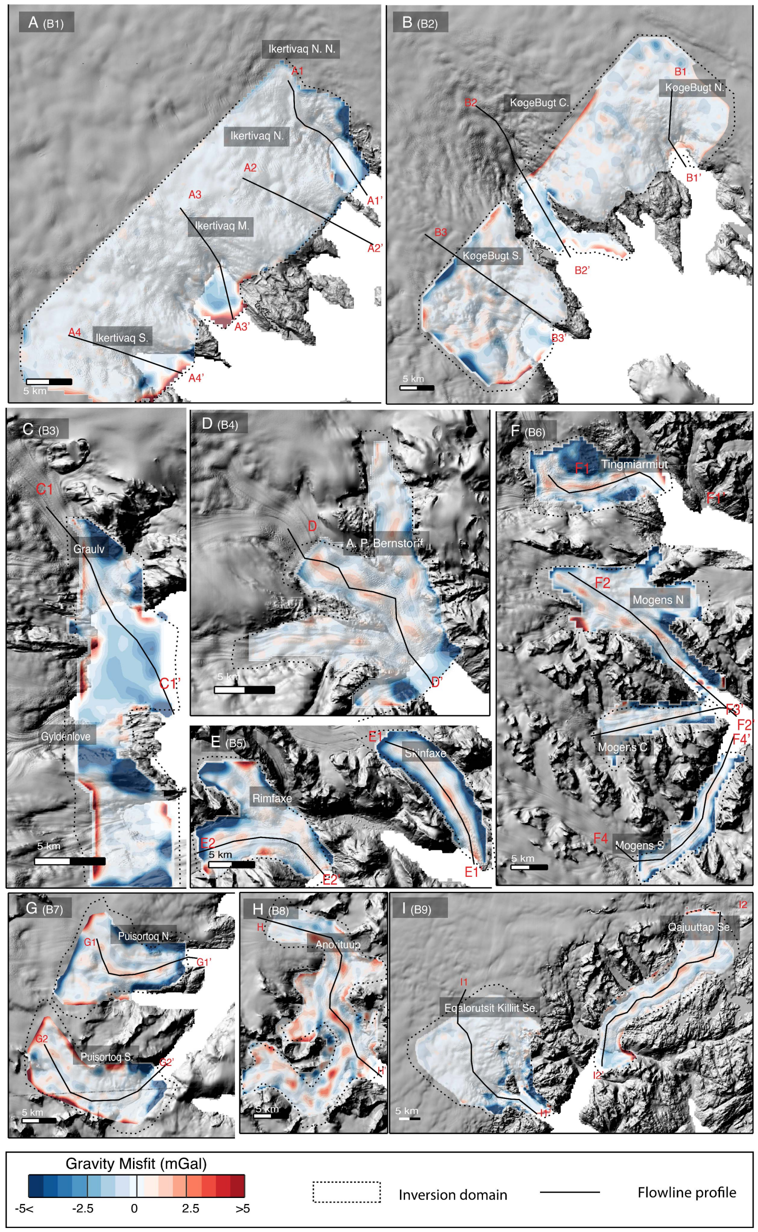

Figure C.1: *Modeled minus observed gravity in milligal (mGal) after the gravity inversion overlayed on a shaded relief version of GIMP3 over (A) Ikertivaq (Block 1), (B) Køgebugt (Block 2), (C) Gyldenløve (Block 3), (D) A. P. Bernstorff (Block 4), (E) Rimfaxe and Skinfaxe (Block 5), (F) Tingmiarmiut and Mogens (Block 6), (G) Puisortoq (Block 7) , (H) Anorituup (Block 8), (I) Qajuuttap Se. and Eqalorutsit Killiit Se. (Block 9). The statistics of the misfit including the mean difference and its standard deviation can be found for each blocks in Table 1.*

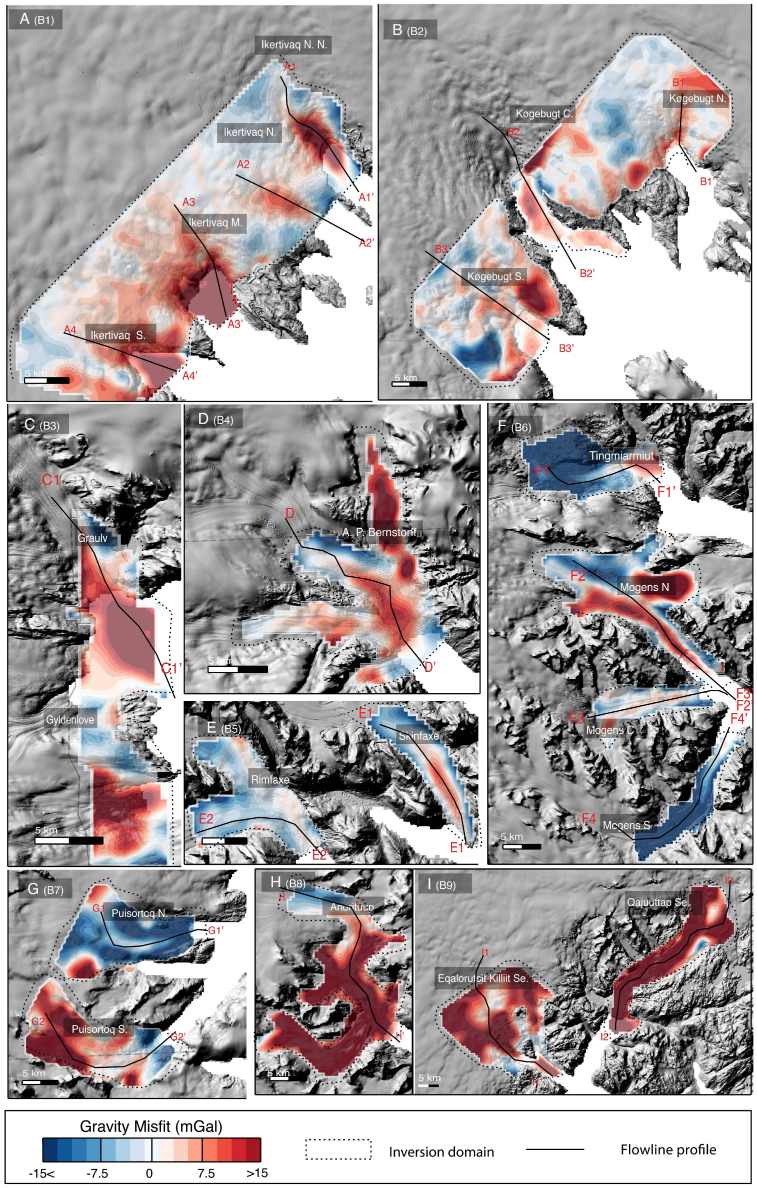

Figure C.2: *Modeled minus observed gravity in milligal (mGal) before the gravity inversion overlayed on a shaded relief version of GIMP3 over (A) Ikertivaq (Block 1), (B) Køgebugt (Block 2), (C) Gyldenløve (Block 3), (D) A. P. Bernstorff (Block 4), (E) Rimfaxe and Skinfaxe (Block 5), (F) Tingmiarmiut and Mogens (Block 6), (G) Puisortoq (Block 7) , (H) Anorituup(Block 8), (I) Qajuuttap Se. and Eqalorutsit Killiit Se. (Block 9). The statistics of the misfit including the mean difference and its standard deviation can be found for each blocks in Table 1.*

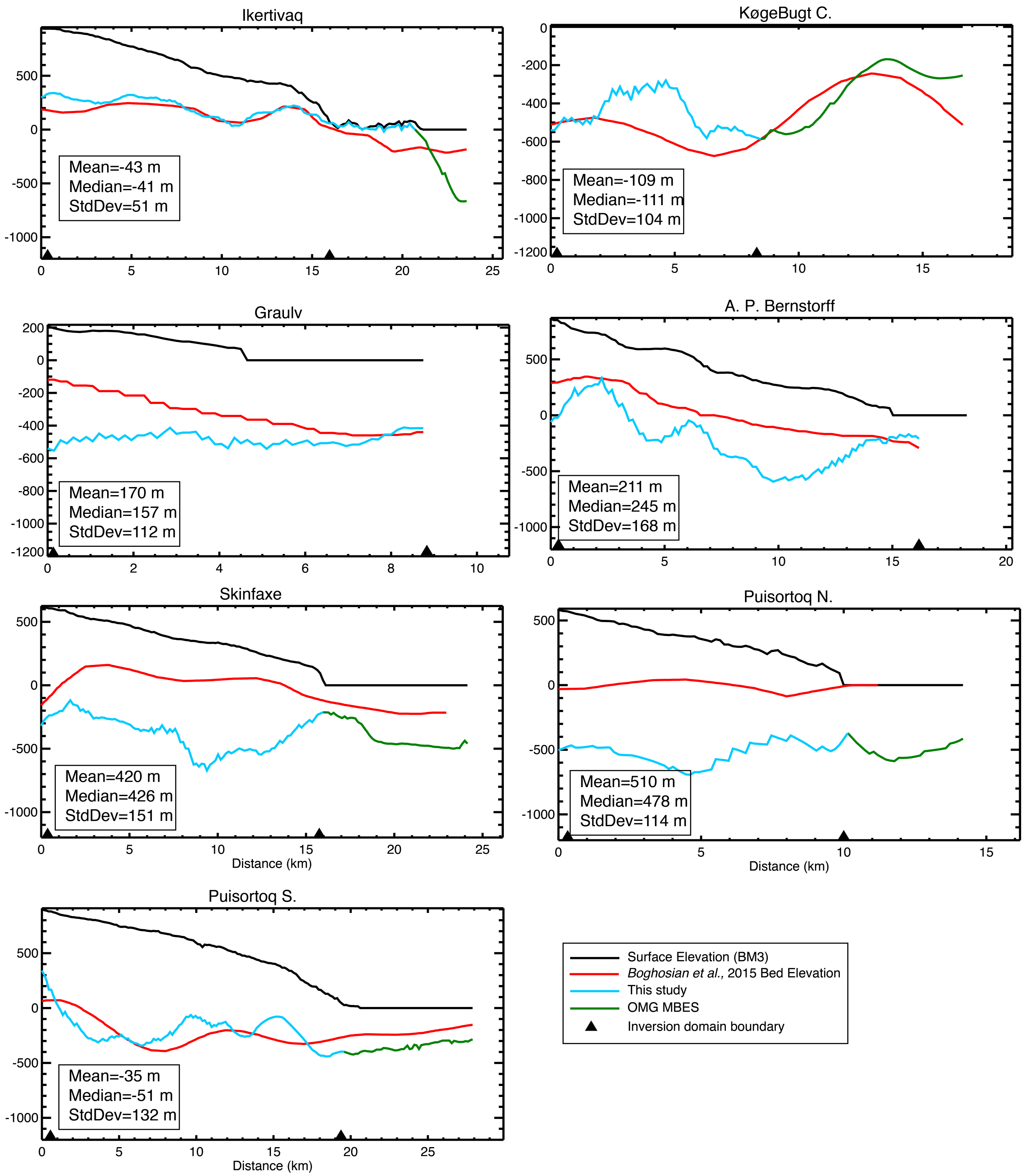

Figure C.3: *Comparison of bed elevation from Boghosian et al., 2015 with OIB bed elevations. The inserts show the statistic of the difference between Boghosian et al., 2015 and bed elevations from this study in the inversion domain boundary.*

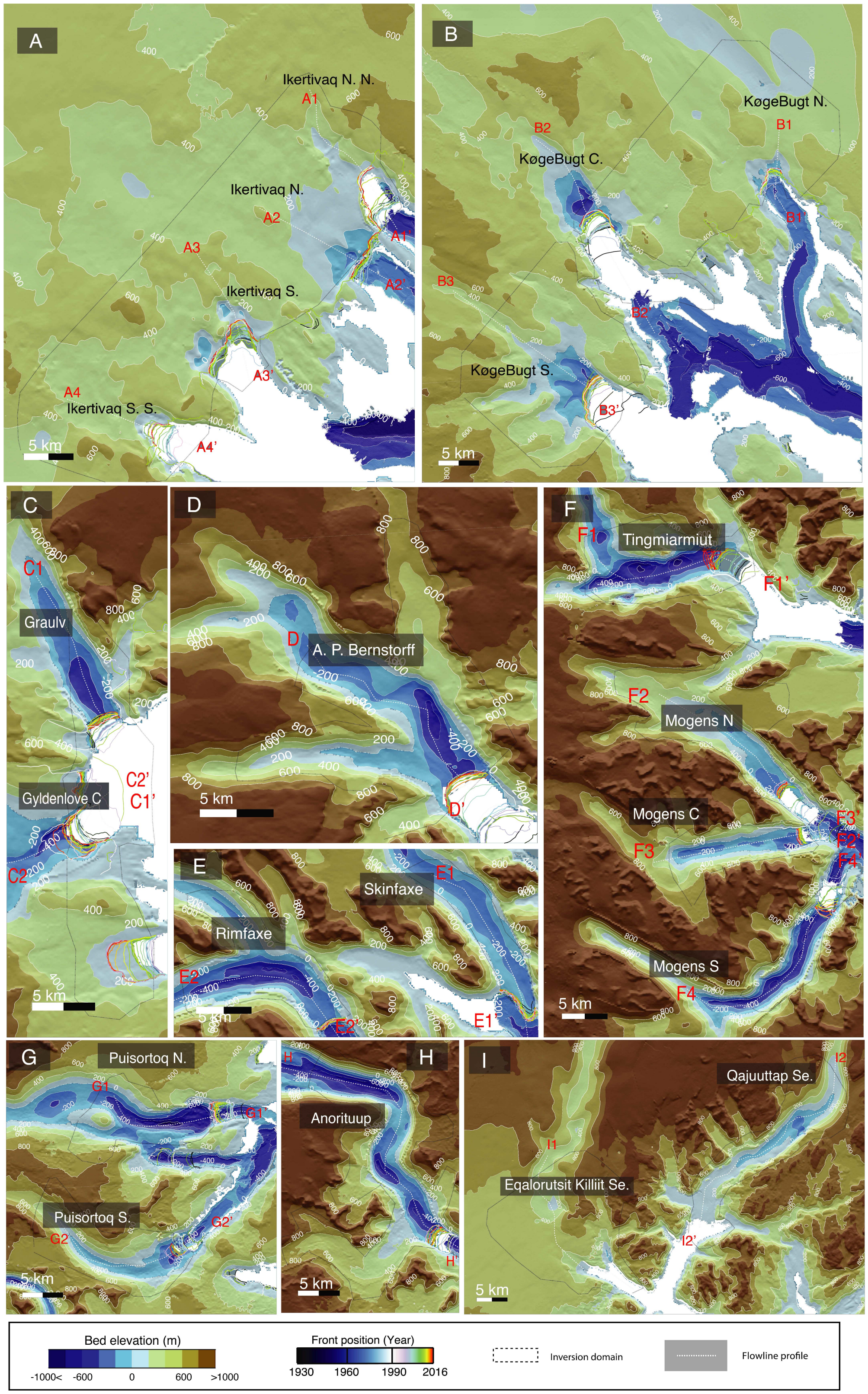

Figure C.4: *Bed elevation from BedMachine v3 data over A) Ikertivaq (B1), B) Køgebugt (B2), C) Gyldenløve and Graulv (B3), D) A. P. Bernstorff (B4), (E) Rimfaxe and Skinfaxe (B5), (F) Tingmiarmiut and Mogens (B6), (G) Puisortoq (B7), Anorituup (B8), Qajuuttap Se. and Eqalorutsit Killiit Se. (B9). Contour lines are shown at a 200-m interval. White is no data.*

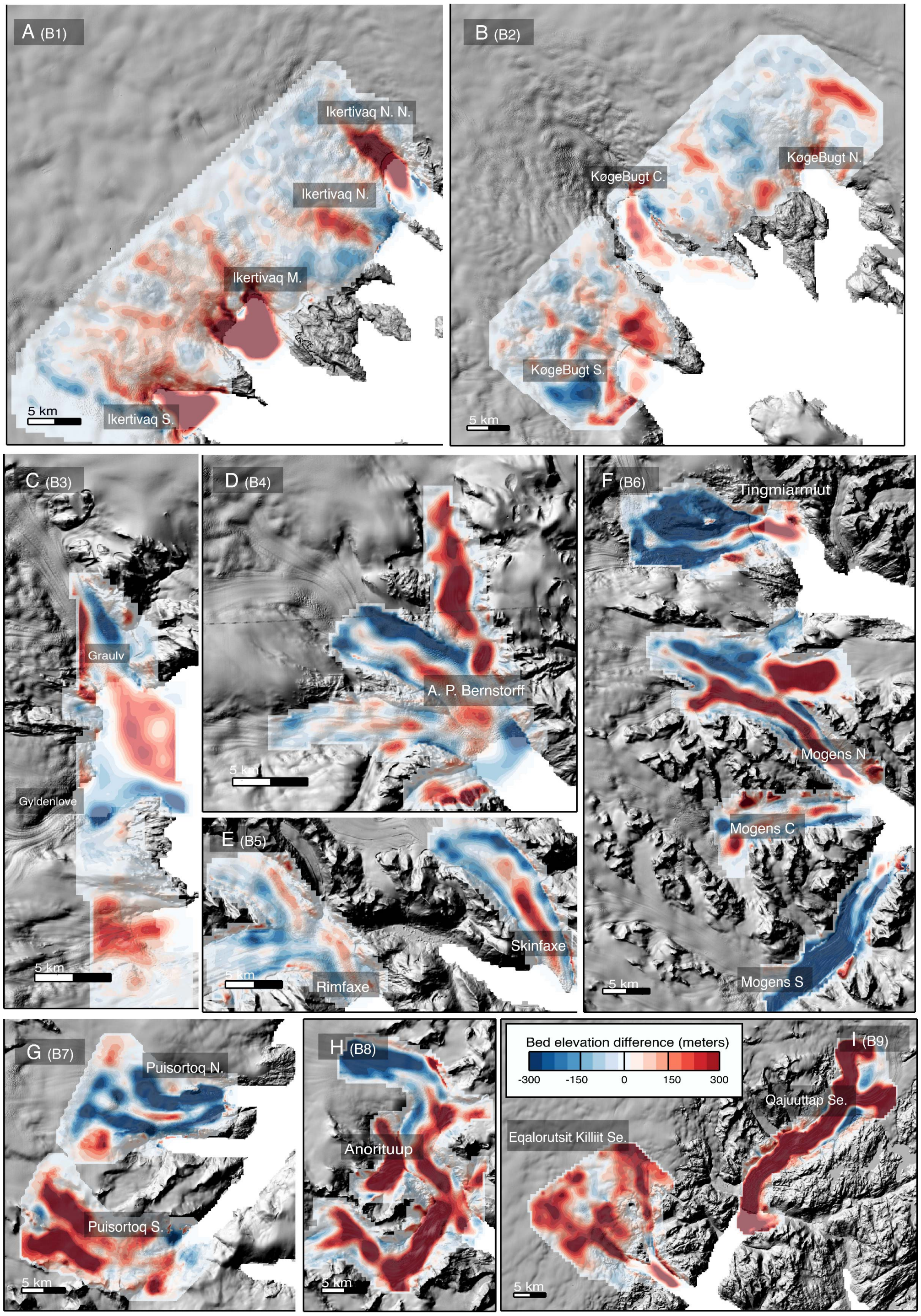

Figure C.5: *Comparison of BM3 bed elevation and our study (meters) overlayed on a shaded relief version of GIMP3 over A) Ikertivaq (Block 1), B) Køgebugt (Block 2), C) Gyldenløve (Block 3), D) A. P. Bernstorff (Block 4), (E) Rimfaxe and Skinfaxe (Block 5), (F) Tingmiarmiut and Mogens (Block 6), (G) Puisortoq (Block 7) , Anorituup(Block 8), Qajuuttap Se. and Eqalorutsit Killiit Se. (Block 9).*

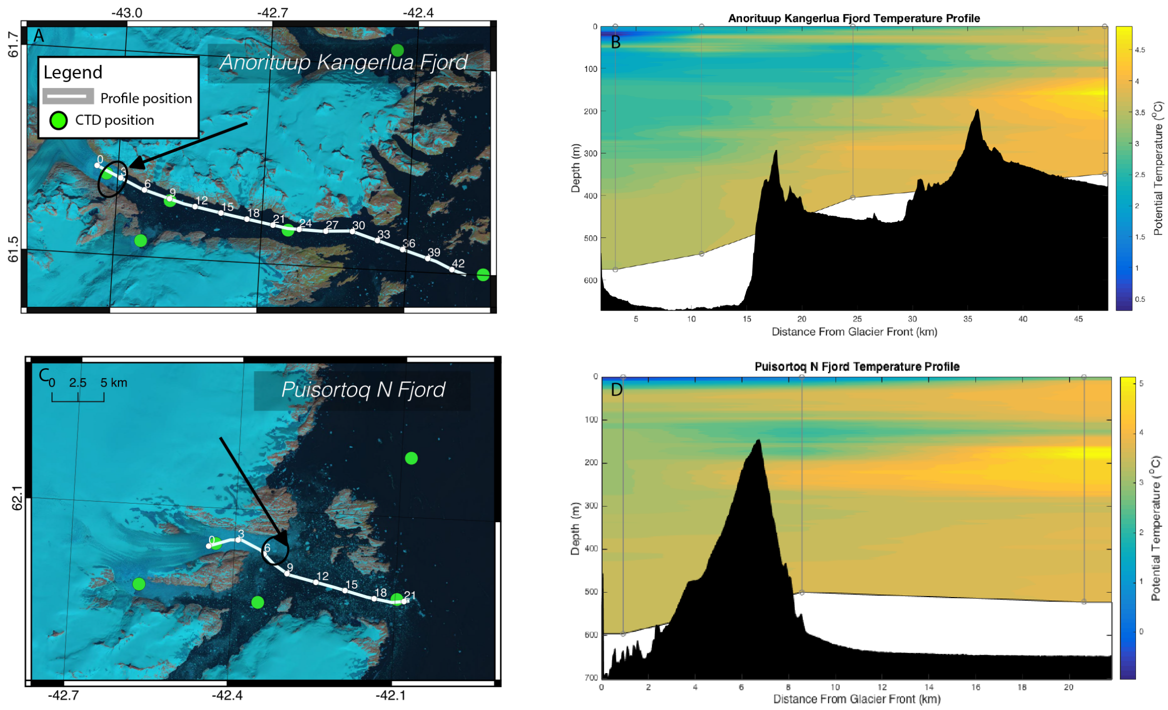

Figure C.6: *a) and c) shows area where stranded icebergs over Puisortoq N and Anorituup fjords (black arrow) were observed between 2013 and 2017. The landsat images shown here are from september 2014 (a) and 2017 (c). b) and d) shows Temperature profile and OMG bathymetry along the fjords of Anorituup and Puisortoq N. CTD and profile location are shown in a) and c).*

Table C.1: *Column 1: Glacier name, Column 2: Box number as in Figure 4.1, Column 3: Sea level rise equivalent of each glacier basins (meters), Column 4: misfit before the inversion (mGal), Column 5: misfit after the inversion (mGal), Column 6: Uncertainty in bed elevation before the inversion (m), Column 7: Uncertainty in bed elevation after the inversion, Column 8: Ice velocity averaged on a subregion close to the front (km/yr), Column 8: Area of drainage basin (km^2), Column 9: Ice discharge in the 1990s using OIB gravity inversion (Gt/yr), Column 10: Ice discharge in the 1990s using BM3 (Gt/yr), Column 11: Balance SMB from RACMO SMB for the period 1960-1989 (Gt/yr), Column 12: Error on the balance SMB (Gt/yr), Column 13: Error on the ice discharge calculation (Gt/yr)*

Glacier Name	Box Number	SLE (meters)	Misfit Before (mGal)	Misfit After (mGal)	Bed Error Before (m)	Bed Error After (m)	Front Speed 2016 (km/yr)	Basin area (square km)	Fluxes OIB in 1990s (Gt/yr)	Fluxes BM3 in 1990s (Gt/yr)	Balance SMB (60-89) (Gt/yr)	Error on SMB (60-89) (Gt/yr)	Error on fluxes (Gt/yr)
Ikertivaq N N	1	0.07	6.7	1.1	115.5	19.0	6	4849	5.2	1.93	4.8	0.5	0.7
Ikertivaq N							3.3	1702	1.8	1.7	1.8	0.2	0.2
Ikertivaq M							1.8	3897	5.2	1.898	4.3	0.4	0.5
Ikertivaq S							2.1	5162	5.3	3.9	5.4	0.5	0.6
KøgeBugt N	2	0.09	5.3	0.9	108.6	15.5	1.9	3479	3.2	1.7	3.4	0.3	0.3
Køgebugt C							7	17171	/	/	/	/	/
Køgebugt S							4	3282	5.9	5	5.3	0.5	0.6
Graulv	3	0.02	8.3	3.2	143.1	55.2	3.4	5359	4.3	3.7	4.8	0.5	0.6
A. P. Bernstorff	4	0.02	7.3	1.2	125.9	20.7	3.4	5036	4.4	4.2	4.9	0.5	0.6
Skinfaxe	5	0.01	7.1	2.8	122.4	48.3	2.4	3552	1.8	1.5	1.8	0.2	0.4
Rimfaxe			3.6	1.6	62.1	27.6	2.5	2773	1.9	1.8	1.8	0.2	0.3
Tingmiarmiut	6	0.02	13	2.4	224.1	41.4	4.8	4348	4.4	4.8	4.5	0.5	0.5
Mogens N							3	1918	1.9	1.1	1.7	0.2	0.2
Mogens C							1.8	771	0.5	0.5	0.6	0.1	0.1
Mogens S							3.4	2178	2.5	2.8	2.7	0.3	0.4
Puisortoq N	7	0.006	7.2	1.6	124.1	27.6	2.9	2356	3.2	4.6	2.5	0.3	0.4
Puisortoq S							1.7	454	0.5	0.5	0.3	0	0.1
Anorituup	8	0.006	12.3	1.2	212.1	20.7	3.7	3375	5.5	4.9	3.8	0.4	0.5
Eqalorutsit Killiit Se.	9	0.02	10.1	1.2	174.1	20.7	0.83	4135	2.6	0.7	3.1	0.4	0.6
Qajuuttaap Se							3.6	5312	4.6	0	4.2	0.5	0.6

Total area: 81109 km^2	**Total Flux from Gravi: 64.7 Gt/yr**	**Total Flux from MC: 47.2 Gt/yr**	**Total Flux from SMB: 61.7 Gt/yr**

Legend

Box number Box number from Figure 1

SLE Sea Level Equivalent (meters)

Bed Error After Given as the standard deviation between modelled and observed gravity. Does not include transition zone to BedMachine v3

Bed Error Before Given as the standard deviation between first guess and observed gravity. Does not include transition zone to BedMachine v3

Front speed Given as the average front speed at a subregion of the ice front from the speed map from [*Mouginot et al.,* 2017]

Basin Area Area of the basin plotted in Figure 1

Fluxes Ice discharge is calculated using a flux gate close to the front of the glacier along with ice velocities derived from speckle and feature tracking. The ice thickness is calculated using the inverted bedrock and BedMachinev3 (BM3). A "/" is indicated in the case of Køgebugt Central because the gravity data does not cover the landed part of this glacier.

Mean SMB The mean SMB is calculated at the basin scale using RACMO v2.3 dowscaled at a resolution of 1-km. The SMB is then averaged between 1960 and 1989 over the basins plotted in Figure 1.